



**Politecnico
di Torino**

Characterization of the tensile anisotropy of LPBF Inconel 718 by fracture mechanism behavior analysis

Master Degree Thesis
of Straton Donald Tarimo

In partial fulfilment of the requirements for the
Master of science in Mechanical Engineering

Supervisor: Prof. Raffaella Sesana
Prof. Cristiana Delprete
Co-supervisor: Dr. Matteo Crachi

Torino-Italy, November 2022

Dedication

To You, Holy Ghost / Holy Spirit /
To You, Jesus Christ / Blood of Jesus Christ /
To You, Almighty God of Ancient times

To You, my brothers and sisters Angels of the Living God

STRATON DONALD

Abstract

In recent studies, characterization of tensile anisotropic behavior of metallic materials used the following instruments such as Scanning Electron Microscopy (SEM), Transmission Electron Microscopy (TEM) and Optical Microscopy (OM) to be able to observe the microstructure of the metals. SEM includes Electron Backscatter Diffraction (EBSD) and Energy Dispersive Spectroscopy (EDS). Additive Manufacturing (AM) involves processes that implement three-dimensional (3D) printing of complex geometries, layer by layer. Powder Bed Fusion (PBF) is an AM which uses thermal energy density to selectively melt and fuse powder particles in a powder bed. Laser powder bed fusion (LPBF) is one of the PBF process where the source of thermal energy is a laser power responsible to melt powder particles. LPBF introduces defects such as porosities, elongated columnar dendrites, melt pool on the microstructure of the metals. Researchers have investigated anisotropy caused by LPBF and quantified by tensile properties anisotropies (including elastic modulus E , yield strength σ_y , ultimate tensile strength UTS , elongation at failure $A\%$). It resulted a correlation between printing direction and mechanical properties.

Topic of the present research is In718, a material widely used for aerospace applications and often processed by means of AM, this material shows brittle tensile fracture (i.e., cleavages, transgranular and intergranular fractures) and ductile fracture (i.e., micro voids coalescence) when processed with AM.

The aim of this thesis is to investigate the fracture behaviour of In718 specimens by means of fracture surface analysis. The *in-situ* scanning electron microscopy (SEM) and optical microscopy (OM) are used to characterize the microstructure of In718 specimens fracture surfaces from tensile tests and surfaces of cubic samples obtained by LPBF in AM. The tensile test operated at room temperature is performed on cylindrical specimens obtained with axis parallel and perpendicular to deposition plane. The results confirmed that the measured mechanical properties and fracture surface aspect are affected by deposition direction. The sources of anisotropies such as elongated grain, porosities, lack of fusion and melt pools within the In718 fracture surfaces were observed. OM enabled to observe the microstructure of In718 cubic samples in both deposition orientations for the grain morphology (i.e., elongated columnar dendrites, equiaxed dendrites) and its defects (such as, porosities, keyholes, lack of fusion, melt pools). Additionally, EDS by Energy Dispersive X-ray (EDX) analysis method is used to characterize the chemical composition of In718 superalloy cube samples and its powder particles. Ultimately, explicit dynamics finite element simulation is implemented to visualize the failure of cylindrical specimens of In718 in tensile test.

Keywords:

AM, L-PBF, Selective laser melting (SLM), In718 superalloy, microstructure anisotropy, tensile anisotropy property, scanning electron microscope (SEM), EDS/EDX, optical microscopy (OM), FEM

Acknowledgments

I would like to extend my gratitude to Politecnico di Torino, DIMEAS and Sophia High Tech s.r.l for allowing me to access and work freely with the expensive machines and specimens for my thesis.

I am forever grateful to Italian Embassy in Dar es Salaam and Italian Ministry of Foreign Affairs for the MAECI scholarship that enabled me to start my studies here at Politecnico di Torino. Also, Madam Valeria La Scala, I appreciate your time and consideration that you gave me at the embassy.

However, the encouragement and guidance from my supervisor Prof. Raffaella Sesana, has made this thesis to come into completion and with success.

I am grateful to my co-supervisor Dr. Matteo Crachi for guiding me in the technical aspects of this project. All the hard work we did together during the summer when it was hot has been accomplished now.

Next, I would like to thank Mr. Gianpaolo Serino (DIMEAS) for guiding us how to use SEM and everyone in one way or the other in this matter.

Likewise, I would like to thank Dr. Luca Lavagna and Prof. Pavese (DISAT), for allowing us to use optical micrography and other facilities in their Laboratory with short time notice.

My fellow students, thank you for working with me during my studies.

Last of all, my family and especially Ms. Maria Antonietta Nigro and her mother Carmela Calice Barbaro for their support during the hard times and now it is accomplished.

Table of Contents

Dedication	II
Abstract	III
Acknowledgments	IV
Figure directory	IV
Table directory	VII
Abbreviations	VIII
Symbols	X
1 Introduction	1
1.1 Main Topic	1
1.2 Aim.....	4
1.3 Organization of the thesis	5
1.4 Inconel 718	6
1.4.1 Chemical composition	6
1.4.2 Properties.....	6
1.4.3 Inconel 718 Powder.....	7
1.5 Additive Manufacturing	8
1.5.1 Selective laser Melting	10
1.5.2 LPBF Process parameters	11
1.5.3 Scan strategy	11
1.5.4 AM Sample orientations	14
1.6 Components post processing	15
1.6.1 Temperature gradient and solidification rate control in AM	17
1.7 Types of fracture in monotonic tensile test.....	19
1.8 In718 microstructure defects.....	21
2 State of the art	22
2.1 LPBF.....	22

2.2	Anisotropic Mechanical properties	24
2.2.1	Tensile property anisotropy:	24
2.2.2	AM of In718 tensile properties anisotropies from literature review	25
2.3	Anisotropic microstructures:.....	26
2.3.1	Electron backscattering deffraction (EBSD)	26
2.3.2	Transmission Electron Microscope (TEM).....	27
2.3.3	Scanning Electron Microscope (SEM).....	28
3	Problem and research objective	30
4	Materials and methods.....	31
4.1	Experimental plan	31
4.1.1	Powder morphologies and size distribution	31
4.1.2	Data acquisition to compute yield strength, UTS, elongation	31
4.1.3	Analyse the anisotropic microstructures of fractured surfaces and defects.....	32
4.1.4	In718 superalloy cubes: analysing the anisotropic microstructures and chemical composition	33
4.2	Specimens	34
4.2.1	Chemical compositions	34
4.2.2	Specimen orientations and geometry	35
4.2.3	Laser Process parameters	35
4.2.4	Heat treatment of In718 samples	36
4.3	Equipments.....	37
4.3.1	Tensile test machine	37
4.3.2	Polishing machine	38
4.3.3	Optical microscopy	39
4.3.4	SEM	39
4.4	Tensile test and characterization of In718 samples	40
4.4.1	Tensile test procedure.....	40
4.4.2	Acquired data	40

4.4.3	Tensile test parameters:.....	40
4.4.4	SEM: Fracture surface analysis.....	41
4.4.5	OM : metallography preparation.....	42
4.4.6	EDS maps : Chemical analysis on the microstructure and In718 powder	43
5	Results and discussions.....	44
5.1	Inconel 718 Powder analysis	44
5.1.1	In718 powder particle morphology	44
5.2	Tensile test results.....	47
5.2.1	Stress-strain curves of Inconel 718 superalloys:	47
5.2.2	Stress- strain trend for all samples of Inconel 718 superalloys.....	50
5.2.3	Summary of tensile anisotropies of Inconel 718 samples.....	50
5.3	Optical micrography for microstructure analysis	51
5.3.1	Sample A2.1: AS.....	51
5.3.2	Sample A2.2: HT	52
5.3.3	Sample B2.1: AS.....	53
5.3.4	Sample B2.2 HT.....	54
5.3.5	Microstructure anisotropies characterization	55
5.4	SEM Fracture surfaces analysis	56
5.4.1	Specimen 1: ZX orientation	56
5.4.2	Specimen 6: HT, XY orientation	64
5.4.3	External surface analysis	70
5.4.4	Tensile anisotropies characterization	74
5.5	Analyse chemical composition for cube specimens: EDS/EDX map	78
5.5.1	Sample A2.1: AS.....	78
5.6	Porosity analysis by using MATLAB code.....	81
5.6.1	Cube Sample A2.1: (ZX) AS.....	82
5.6.2	Cube Sample A2.2:(ZX) HT.....	83

5.6.3	Cube Sample B2.1: (XY) AS	84
5.6.4	Cube Sample B2.2 (XY) HT	85
5.6.5	Cylindrical Specimen 1: (ZX) AS	86
5.6.6	Cylindrical Specimen 6 (XY): HT	87
5.6.7	Summary of porosity values of In718 superalloys specimens	88
6	FEM analysis.....	90
7	Conclusion and future work	92
8	Reference	93
9	Appendix	99
9.1	Appendix A: In718 cylindrical specimen drawing	99
9.2	Appendix B: In718 cube specimen drawing	100
9.3	Appendix C: SEM Micrograph in Image J and PSD results by Origin Pro:.....	101
9.4	Appendix D: SEM Micrograph:.....	102
9.5	Appendix E: SEM: EDS/EDX for Spectrum results:	110

Figure directory

FIGURE 1-1:CF6-6 CUTAWAY - JET ENGINE [8]	2
FIGURE 1-2: SEM CHARACTERIZATION OF STATES OF IN718 POWDER PARTICLES.....	7
FIGURE 1-3: SLM PROCESS CHAIN [17].....	8
FIGURE 1-4: SCHEMATIC OF LPBF PROCESS [19]	9
FIGURE 1-5: WORKING PRINCIPLE OF LPBF PROCESSING CHAMBER WITH MAIN COMPONENTS [21].....	10
FIGURE 1-6: FIGURE: TYPES OF SCAN STRATEGIES (A) UNIDIRECTIONAL (B) BI-DIRECTIONAL (C) ISLAND SCANNING (D) SPOT MELTING (E)SPOT MELTING CONTOURS WITH SNAKING FILL (F) LINE MELTING CONTOURS WITH SNAKING FILL [26]	11
FIGURE 1-7: TWO TYPES OF SCAN PATHS IN LPBF [27].....	12
FIGURE 1-8:LASER POWER VERSUS SCAN SPEED WHERE PROCESSING WINDOW IS SHOWN IN RED LINES [27].....	12
FIGURE 1-9: ORIENTATION DESIGNATION FOR MECHANICAL TESTING OF AM MATERIALS.....	14
FIGURE 1-10: TRANSFORMATION TIME TEMPERATURE(TTT) DIAGRAM OF IN718 SUPERALLOYS [37].....	15
FIGURE 1-11: STAGES OF HEAT TREATMENT FOR IN718 SUPERALLOYS [39].....	16
FIGURE 1-12: (A) SCHEMATIC CURVE TO SHOW RELATIONSHIP BETWEEN HEAT INPUT, GRAIN GROWTH AND COOLING OF MELT POOL (B) GRAPH SHOWING SOLIDIFICATION RATE VERSUS TEMPERATURE GRADIENT [42]	18
FIGURE 1-13: (A) BRITTLE FRACTURE DUE TO TRANSGRANULAR FRACTURE, (B) BRITTLE FRACTURE DUE TO INTERGRANULAR FRACTURE, (C) TEMPERATURE VERSUS ENERGY ABSORBED DURING FRACTURE, (D) DUCTILE FRACTURE DUE TO MICRO VOIDS FORMATION (E) CLEAVAGE FRACTURE [45] [46]	20
FIGURE 1-14: CHARACTERIZATION BY BSE SEM SHOWING (A) CRACKS (B) POROSITIES [47]	21
FIGURE 2-1: (A) LASER POWDER BED FUSION(L-PBF), (B) CYLINDRICAL DOG BONES AT DIFFERENT BUILD ORIENTATIONS HORIZONTAL (XY) BUILD, AND VERTICAL ORIENTATION BUILD (ZX) AND AT AN ANGLE OF 45° [9].....	22
FIGURE 2-2: 3D CUBES OF 2 MM ³ SHOWING THE TOP VIEW (XY), RIGHT VIEW(YZ), FRONT VIEW(ZX) MICROSTRUCTURES PROCESSED POWER OF (A) 950 W AND (B) 250 W AT A MAGNIFICATION OF 500 μM [9].....	23
FIGURE 2-3: EBSD ORIENTATION MAPS IN LONGITUDINAL SECTION TO ZX ORIENTATION (A) ELONGATED COLUMNAR GRAINS (B) EQUIAXED GRAINS	26
FIGURE 2-4: IPF EBSD MAP SHOWING THE EFFECT OF THE SCAN PATTERN ON GRAIN ORIENTATION [32]	26
FIGURE 2-5: TEM MICROGRAPHS WITH SAED PATTERNS OF LAVES PHASES [63]	27
FIGURE 2-6: FRACTOGRAPHY SURFACES OF IN718 SUPERALLOYS SAMPLES (A) AS SAMPLE (B) HT SAMPLE [53].....	28
FIGURE 2-7: IN718 SUPERALLOYS SAMPLES AS PRODUCED BY SLM: A) LONGITUDINAL SECTION, B) TRANSVERSE SECTION [53]	29
FIGURE 2-8: IN718 SUPERALLOYS SAMPLES AFTER HOMOGENIZATION + AGING PRODUCED BY SLM:.....	29
FIGURE 4-1: TTT DIAGRAM FOR IN718 [49].....	36
FIGURE 4-2: TENSILE TEST MACHINE, TYPE ZWICK MOD 50KN (DIMEAS)	37
FIGURE 4-3: METALLOGRAPHIC PREPARATION MACHINES (A) SPECIMEN MOLD MACHINE (B) POLISHING MACHINE (DIMEAS) (C) POLISHING MACHINE (DISAT)	38
FIGURE 4-4: OPTICAL MICROSCOPY (DISAT).....	39
FIGURE 4-5: SCANNING ELECTRON MICROSCOPY (DIMEAS)	39
FIGURE 5-1: IN718 POWDER SEM IMAGES (A - C) VIRGIN (C) HIGH MAGNIFICATION SHOWING DENDRITIC FEATURES	44
FIGURE 5-2: (A & B) IMAGE J SAMPLE ANALYSIS (C)PSD	45

FIGURE 5-3: NORMALIZED LIFE AND STRENGTH VERSUS GRAIN SIZE [64]	46
FIGURE 5-4: XY AS N.1.....	47
FIGURE 5-5: SPECIMEN 6, XY HT N.1	48
FIGURE 5-6: SPECIMEN 1, ZX AS N.1	49
FIGURE 5-7: ENGINEERING STRESS - STRAIN ANISOTROPIES FOR ALL SAMPLES OF IN718 SUPERALLOYS	50
FIGURE 5-8: SAMPLE A2.1 AS SHOWING (A) MELT POOLS, POROSITIES AND KEYHOLE (B) ELONGATED COLUMNAR DENDRITES AND EQUIAXED DENDRITES GROWTH DIRECTION (C & D) MELT POOL SIZES AND POROSITIES ON ELONGATED COLUMNAR DENDRITES AND EQUIAXED DENDRITES	51
FIGURE 5-9: SAMPLE A2.2 HT (A) ELONGATED COLUMNAR DENDRITES GROWS RANDOMLY (B) POROSITIES IN RED ARROW	52
FIGURE 5-10: SAMPLE B2.1 SHOWING (A) ISLAND SCAN STRATEGY (B-D) DIRECTION OF CELLULAR DENDRITES	53
FIGURE 5-11: SAMPLE B2.2 (A & C) ISLAND SCAN STRATEGY AND POROSITIES (B) SAMPLE HOMOGENIZATION WITH POROSITIES.....	54
FIGURE 5-12: SPECIMEN 1 SHOWING (A) SHEAR SURFACES/FACETS (B) MAGNIFIED FACET SHOWING THE POROSITIES, DIMPLES, CLEAVAGES, ELONGATED COLUMNAR DENDRITES	56
FIGURE 5-13: (A) SHEAR SURFACE (B) MAGNIFIED SHEAR SURFACE.....	57
FIGURE 5-14: SHEAR SURFACE.....	58
FIGURE 5-15: DUCTILE FRACTURE.....	59
FIGURE 5-16: VERTICAL INTERGRANULAR FRACTURE MIXED WITH VERTICAL TRANSGRANULAR FRACTURE WITH CUP AND CONE.....	60
FIGURE 5-17: DUCTILE FRACTURE MIXED WITH BRITTLE FRACTURE	61
FIGURE 5-18: (A) LACK OF FUSION PORE SPLIT AND BRITTLE FRACTURE (B) LACK OF FUSION PORE SPLIT	62
FIGURE 5-19: FOUR ZONES INDICATING THE STAGES DURING CRACK INITIATION AND PROPAGATION	63
FIGURE 5-20: SPECIMEN 6 SHOWS (A) OVERALL VIEW SHOWING A SMOOTH FLAT SURFACE, (B) DUCTILE FRACTURE AND DIMPLES (C) HORIZONTAL INTERGRANULAR (D) HORIZONTAL TRANSGRANULAR.....	64
FIGURE 5-21: SPECIMEN 6 SHOWS (A) HORIZONTAL INTERGRANULAR FRACTURE (B) LACK OF FUSION PORE NEAR LATERAL SURFACE (C) HORIZONTAL INTERGRANULAR AND QUASI CLEAVAGE FRACTURE	65
FIGURE 5-22: (A) T SHAPE HORIZONTAL INTERGRANULAR FRACTURE (B) PARALLEL HORIZONTAL INTERGRANULAR FRACTURE(LAYER TO LAYER SPLIT) (C) FACETS, DIMPLES AND HORIZONTAL INTERGRANULAR FRACTURE	66
FIGURE 5-23:(A) PORE (DIAM 10) WITH HORIZONTAL TRANSGRANULAR FRACTURE AND MICRO VOIDS COALESCENCE (B) HORIZONTAL TRANSGRANULAR FRACTURE INSIDE LACK OF FUSION PORE, MICRO VOIDS COALESCENCE (C) INTEGRANULAR MIXED WITH CLEAVAGES FRACTURE.....	67
FIGURE 5-24: LACK OF FUSION PORE WITH BRITTLE INTERGRANULAR FRACTURE MIXED WITH DUCTILE FRACTURE (MICRO VOIDS COALESCENCE) ...	68
FIGURE 5-25: BRITTLE AND DUCTILE FRACTURE MIXED.....	69
FIGURE 5-26: SURFACE ENHANCEMENT OPERATIONS (A) FINISH MACHINING (B) DRAG FINISH (C) VIBRATORY SURFACE FINISH [65]	70
FIGURE 5-27: (A) PRIMARY AND SECONDARY CRACKS (B) MAGNIFIED PRIMARY CRACK MAGNIFICATION 692 X.....	71
FIGURE 5-28: (A) PRIMARY CRACK (B & C) MAGNIFIED VIEWS.....	72
FIGURE 5-29: SPECIMEN 6 DISPLAY LATERAL SURFACE CRACK IN XY ORIENTATION	73
FIGURE 5-30: SAMPLE A2.1 AS SHOWS (A) SEM MICROGRAPH (B) EDS MAP	78
FIGURE 5-31: EDS MAP SHOWING CHEMICAL COMPOSITIONS.....	79
FIGURE 5-32: EDS MAP SHOWING IN718 PRECIPITATES	80

FIGURE 5-33: CUBE SAMPLE A2.1 POROSITIES	82
FIGURE 5-34: CUBE SAMPLE A2.2 POROSITIES	83
FIGURE 5-35: CUBE SAMPLE B2.1 POROSITIES	84
FIGURE 5-36: CUBE SAMPLE B2.2 POROSITIES	85
FIGURE 5-37: CYLINDRICAL SPECIMEN 1 SHOWING POROSITIES	86
FIGURE 5-38: CYLINDRICAL SPECIMEN 6 SHOWING POROSITIES	87
FIGURE 6-1: SPECIMEN 8 (XY_AS). XY AS.....	91
FIGURE 6-2: SPECIMEN 6 (XY_HT)	91
FIGURE 9-1: (A & C) IMAGE J SAMPLE ANALYSIS (C) POWDER SIZE DISTRIBUTION (PSD).....	101
FIGURE 9-2: LATERAL SURFACE SHOWING THE PRIMARY CRACKS AS RESULTED DUE TO THE EFFECT OF MACHINING, LACK OF FUSION AND POROSITY	102
FIGURE 9-3: TENSILE FRACTURE SURFACE OF PERPENDICULAR (ZX) BUILT INCONEL 718 SAMPLE TESTED AS,	103
FIGURE 9-4: TENSILE FRACTURE SURFACE OF HORIZONTALLY (XY) BUILT INCONEL 718 SAMPLE TESTED HEAT TREATED, (A) OVERALL VIEW SHOWING A SMOOTH FLAT SURFACE,.....	104
FIGURE 9-5: CRACKS, LATERAL SURFACE PEELED/SPLIT, INTERGRANULAR FRACTURE ALONG THE BOUNDARY.....	105
FIGURE 9-6: DUCTILE FRACTURE, BRITTLE FRACTURE, INTERGRANULAR FRACTURE, TRANSGRANULAR FRACTURE, QUASI CLEAVAGE.....	106
FIGURE 9-7: INTERGRANULAR FRACTURE NEAR THE LATERAL SURFACE, CLEAVAGE RIVERS AND STAIRS, MICROVOIDS COALESCENCE, DIMPLES, DUCTILE AND BRITTLE FRACTURE	107
FIGURE 9-8: LACK OF FUSION, UNMELTED PARTICLES.....	108
FIGURE 9-9: DUCTILE FRACTURE, MICRO VOIDS COALESCENCE	109
FIGURE 9-10: SEM MICROGRAPH SPECTRUMS POINTS	110

Table directory

TABLE 1-1: SAE SPECIFICATION FOR INCONEL 718 CHEMICAL COMPOSITION	6
TABLE 2-1: OVERVIEW OF ANISOTROPIC CAUSES.....	24
TABLE 2-2: SUMMARY OF AM IN718 TENSILE PROPERTIES ANISOTROPIES.....	25
TABLE 4-1: CHEMICAL COMPOSITION OF IN718 SUPERALLOY.....	34
TABLE 4-2: SPECIMENS GEOMETRY AND ORIENTATION	35
TABLE 4-3: LPBF PROCESSING PARAMETERS FOR IN718 SUPERALLOYS.....	35
TABLE 4-4: TENSILE TEST PARAMETERS	40
TABLE 5-1: IN718 POWDER SIZES.....	46
TABLE 5-2: TENSILE ANISOTROPIES PROPERTIES OF INCONEL 718 SAMPLES.....	50
TABLE 5-3: MICROSTRUCTURE ANISOTROPIES	55
TABLE 5-4: IN-SITU TENSILE TEST RESULTS	74
TABLE 5-5: MECHANICAL PROPERTIES (INDICATIVE ONLY) [66]	75
TABLE 5-6: ANISOTROPY CHANGE FOR MODULUS AND ELONGATION	76
TABLE 5-7: ANISOTROPY CHANGE FOR YIELD STRENGTH AND UTS	77
TABLE 5-8: SUMMARY OF POROSITY VALUES IN FRACTIONS.....	88

Abbreviations

AM	Additive Manufacturing
AS	As built
BD	Build direction
DLD	Direct laser deposition
EBF ³	Electron beam freeform fabrication
E	Young's modulus
E_l	Elongation
E_d	Energy density
EDS	Energy dispersive spectroscopy
EDX	Energy dispersive X-ray
FCC	Face centered cubic
G	Temperature gradient
γ	Gamma
γ'	Gamma prime
γ''	Gamma double-prime
HD	Hatch direction
HT	Heat treated
In718	Inconel 718
LPBF	Laser powder bed fusion
OM	Optical microscopy
PBF	Powder bed fusion
PSD	particle size distribution
σ_y	yield strength
R	solidification rate

SLM	Selective laser melting
SEM	Scanning electron microscopy
SS	Scanning strategy
SMD	Shaped metal deposition
SD	Scan direction
TTT	Time-Temperature-Transformation
UTS	Ultimate tensile strength
XRD	X-ray diffraction

Symbols

E_d	$[J/mm^2]$ or $[J/mm^3]$	energy density
$P = P_v$	$[W]$	laser power
v	mm/s	scan speed
$a_1 = A_1$	$[-]$	hatch distance
t	$[mm]$	layer thickness
h	$[mm]$	scan spacing
σ_x	$[MPa]$	yield strength or UTS in x direction
σ_z	$[MPa]$	yield strength or UTS in z direction

1 Introduction

1.1 Main Topic

Superalloys consists of the austenitic fcc matrix phase γ and secondary phases. These secondary phases are carbides (MC , $M_{23}C_6$, M_7C_3), γ' , γ'' , δ , η and unfavorable phases (σ , μ and laves) [1]. There are three groups of superalloys, namely nickel-base, iron-nickel-base and cobalt-base superalloys.

Alloy 718 or Inconel 718 or In718 or UNS NO7718 is the nickel-base superalloy that can be operated at intermediate temperatures that vary between 450°C - 700°C and still maintains its resistance to oxidation and corrosion [2]. Also, In718 can be used in high temperatures of 816°C to the melting point of its alloys [1]. Due to incipient temperature of some alloys (e.g., Al) evaporation hinder the full capability of In718. In718 is strengthened by precipitation hardening of γ'' , $Ni_3(Nb, Ti, Al)$, tetragonal unit cell, space group: $14/mmm$) and γ' , $N_3(Ti, Al, Nb)$, cubic unit cell, space group: $Pm-3m$) [3] [4].

Additive manufacturing (AM) has enabled the production of products with complex geometries that are not easily processed by conventional processes (such as forging, casting and wrought).

In718 is a hard material, therefore, to fabricate components in In718 by conventional processes is challenging. By means of additive manufacturing, alloy 718 is an advantageous choice because of its good weldability [2] and little surface finishing is required.

Space and turbine engines industries have increased the use of this In718 superalloy due to the need of weight reduction and service operations at high temperatures [5].

Inconel 718 is used significantly approximately 34% [6] for jet engines (refer Figure 1-2) in aerospace industries, gas turbines and steam generators in nuclear power plants, where elevated temperatures are prevailing [7].

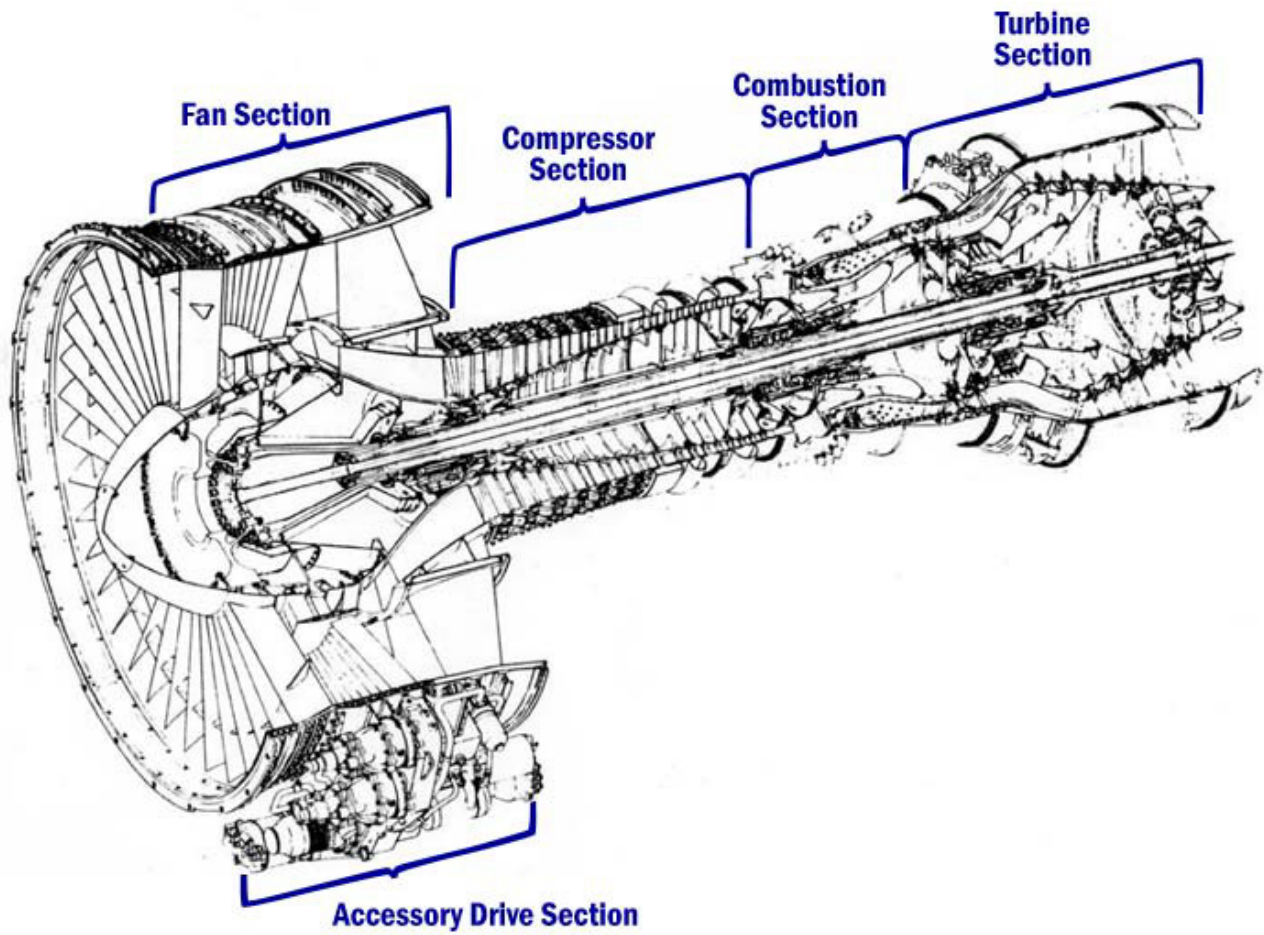


Figure 1-1:CF6-6 cutaway - Jet engine [8]

Also, In718 can be used in cryogenic applications [1]. Main advantages of In718 relates to its high strength, fatigue capability, rupture strength, corrosion and creep resistance [5].

The microstructure and mechanical properties anisotropies depend on grain texture, grain morphology, phases formation, melt pool and porosity [9]. Material crystallography textures, material phases and residual stresses are characterized by electron backscattering diffraction (EBSD), transmission electron microscopy (TEM) [10] and X-ray Powder Diffraction (XRD) [11] respectively. In this study only a brief description will be provided about these key characterization instruments.

This thesis presents the characterization of the tensile anisotropy of LPBF In718 by analysing fracture mechanism behavior in which the microstructures of In718 superalloy will be illustrated and explained. Specimens will be characterized by tensile test, SEM, EDS/EDX and OM [12]. Hence the microstructure anisotropies (columnar dendrites, equiaxed dendrite, porosities, melt pool) and tensile anisotropies (modulus, yield strength, UTS, elongation) are reported here.

1.2 Aim

Aim of this thesis is to investigate the fracture behaviour of In718 specimens by means of fracture surface analysis

In particular tensile specimens obtained in different deposition directions will be tested by means of static and fatigue tests and their fracture surfaces will be investigated by means of different analysis techniques.

The results will be compared with literature.

1.3 Organization of the thesis

Two types of bulk components were produced with In718 powder particles which are cylindrical specimens and cubes. Specimens were obtained with the axis parallel and perpendicular to deposition direction. Further processing, by lathe, mill and power saw, was used to obtain the desired designed shapes and sizes [refer Table 4-2] and Appendix A and B.

The cylindrical specimens were used in tensile testing machine to obtain the fracture surfaces that were examined by scanning electron microscope (SEM) for fracture morphology and the mechanical anisotropies properties (modulus, yield stress, UTS, Elongation) was evaluated from tensile data. However, the cubes were prepared for metallographic analysis in both optical microscopy (OM), SEM and Energy Dispersive Spectrometer (EDS) by Energy Dispersive X-ray (EDX) analysis method.

In brief the thesis will address the following topics:

Section 1: Introduction

Section 2: State of the art

Section 3: Problem statement and research objectives

Section 4: Results and discussions

Section 5: Conclusion and future work

Section 6: Finite element method (FEM) analysis

1.4 Inconel 718

Being of nickel base superalloy, its incipient melting temperatures are less than 1204°C, are a function of chemical composition and a choice PBF in AM [1]. The pure nickel has a melting temperature of 1453°C. According to Table 1-1, elements can be modified by reducing or increasing or adding new elements according to the designer to achieve certain mechanical properties. For example, addition of Yttria, rhenium, hafnium can alter the microstructure of In718.

1.4.1 Chemical composition

According to SAE, Inconel 718 [13] has the following elements shown in table 1-1.

Table 1-1: SAE specification for Inconel 718 chemical composition

Element	min	max
Chromium	17.00	21.00
Nickel	50.00	55.00
Molybdenum	2.80	3.30
Niobium (Columbium) ^N	4.75	5.50
Titanium	0.65	1.15
Aluminum	0.20	0.80
Iron*	(11.14)	(24.40)
Carbon, Manganese, Silicon, Phosphorus, Sulfur, Cobalt, Boron, Copper, Lead, Bismuth, and Selenium	-	≤ 1.00 each

In our work, the chemical composition has been modified refer table 4-1, but around the indicated range in table 1-1.

1.4.2 Properties

Pure nickel has a density of 8900 kg/m³ while the nickel-base superalloys densities range from 7800 to 8900 kg/m³. Therefore, the density reducing elements (such as aluminium, titanium, chromium) and increasing elements (i.e., tungsten, rhenium, tantalum) can cause anisotropies in both microstructures and tensile properties [1].

Superalloys have a modulus of elasticity of approximately 205 GPa. Directional grain or crystal orientation can give result in a moduli range between 124 to 310 GPa [1]. In the result section, it can be proved that island scan strategy in parallel deposition plane the elastic modulus higher than the perpendicular deposition plane as shown in section 5.2.3.

1.4.3 Inconel 718 Powder

According to Gruber et al., [14], by laser diffraction method In718 powder particles morphologies are categorized into four states as virgin(V), used(U), overflow(O) and spatter(S).

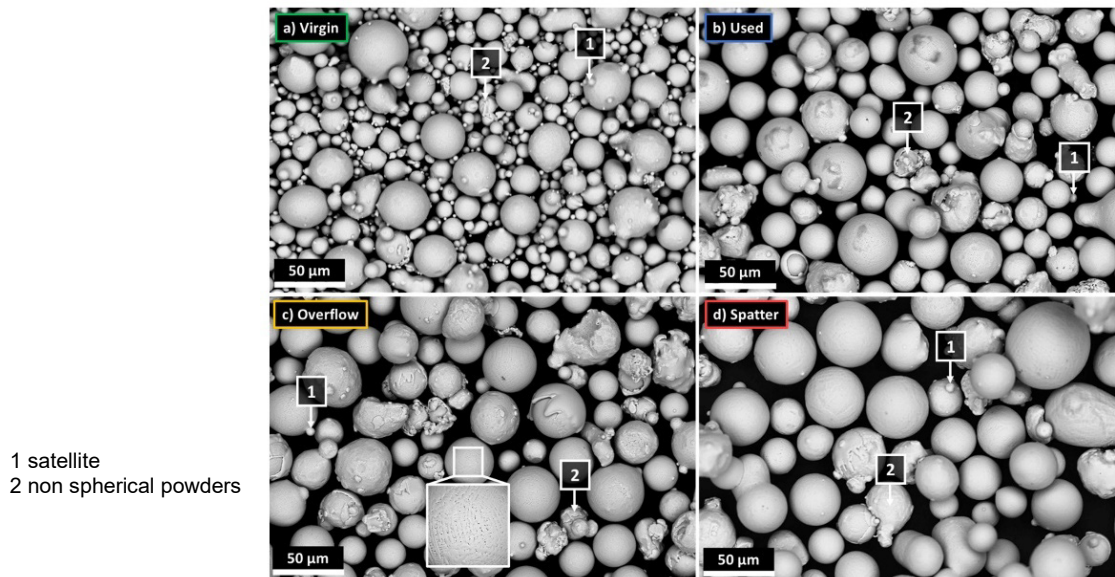


Figure 1-2: SEM characterization of states of In718 powder particles (a) virgin, (b) used, (c) overflow, (d) spatter [14]

As observed in Figure 1-1, that virgin configuration has particles sizes less than 10 µm with highest number of particles with satellites (1) morphologies and lower number of non-spherical powders (2) which can be due gas atomized processing defects. The used, overflow and spatter (has PSD of 10–45 µm) configuration particles are opposite to the characteristics of the virgin configuration [14].

Corresponding powder SEM images were imported to binarized images and Image J analysis software analysis for particle size and shape distribution (PSD) [14]. In another paper [7], demonstrated that the PSD of In718 powder used in PBF ranged between 15 to 63 µm.

In our work, we will adopt this method where high magnification SEM images with Image J were used to analyse the In718 powder morphologies and sizes as discussed in section 5.1.

According to Spierings et al., [7] [15], flowability of powder particles is measured by a hall funnel flow meter, a bulk density by EV2 volumeter, a tapped density by ETD 1020 automatic tester, an angle of repose by Hall funnel BEP2 Flowability Tester and the Hausner coefficient computed as the ratio of the free bulk density to the tapped density.

1.5 Additive Manufacturing

ISO/ASTM defines AM as “the process of joining materials to make parts from 3D model data, usually layer upon layer as opposed to subtractive (e.g., lathe turning, milling) and formative (e.g., forging, casting, wrought) manufacturing methodologies” [refer figure 1-3] [16].

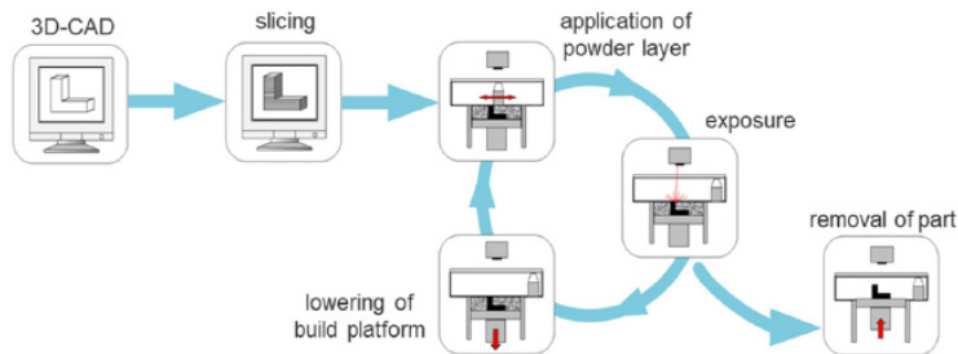


Figure 1-3: SLM process chain [17]

High performance materials such as In718 which take advantage of SLM process due to its capability to operate at high temperatures so the laser power will fuse its powder particles without affecting its final crystal structure. As illustrated in figure 1-4, *part orientation* either in deposition plane or perpendicular to it is the key to understand the anisotropies included in each deposition orientation. Then, *machine preparation* can influence the outcome of microstructure such as defects. In the *building process* many things are involved, for example laser power, scan strategy, quality of powder particles and layer thickness [18] [16]. In post-processing, involves powder removal and heat treatment. The latter, heat is required for annealing (that is stress relieving, solution treatment and homogenization) to remove induced stresses during LPBF in AM, to dissolve γ' , γ'' , δ , and laves phases; to close the pores; and to produce more γ'' and γ' phases for hardening of In718 [18].

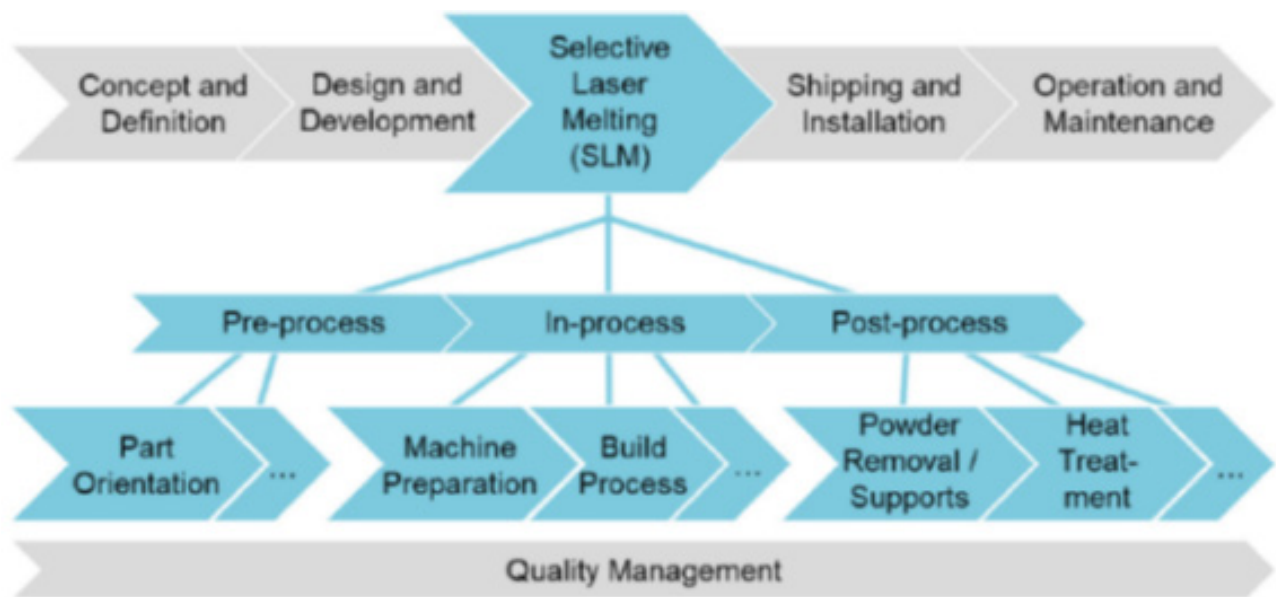


Figure 1-4: Schematic of LPBF process [19]

One of the benefits of AM is to produce complex shapes [16]. While the challenges of AM are reproducibility due to thermal gradient and solidification rates, reliability, anisotropy of mechanical properties and low build-up rates of the processes [20].

1.5.1 Selective laser Melting

Selective laser melting (SLM) is a powder bed fusion (PBF) technology [17] in which according to scan strategy (e.g. island) powder particles are melted and fused with a high laser energy to form a part in a powder bed [refer figure 1-5] [21] [22] [23].

Also, SLM is known as Laser Beam Melting (LBM), Laser Powder Bed Fusion (LPBF), Laser Metal Fusion (LMF), Laser Cusing or Direct Metal Laser Sintering (DMLS) [17].

Figure 1-5 describes LPBF process in which virgin powder particles from powder reservoir are fed into the building platform by recoater arm that moves back and forth. Laser energy is selectively directed to the powder particles in the building platform to melt the first layer then the building platform goes down. Again, the recoater arm spread again the powder particles, in this second time the laser melts the powder particles to fuse this second layer upon the first one. So, the process goes on until the desired shape is obtained.

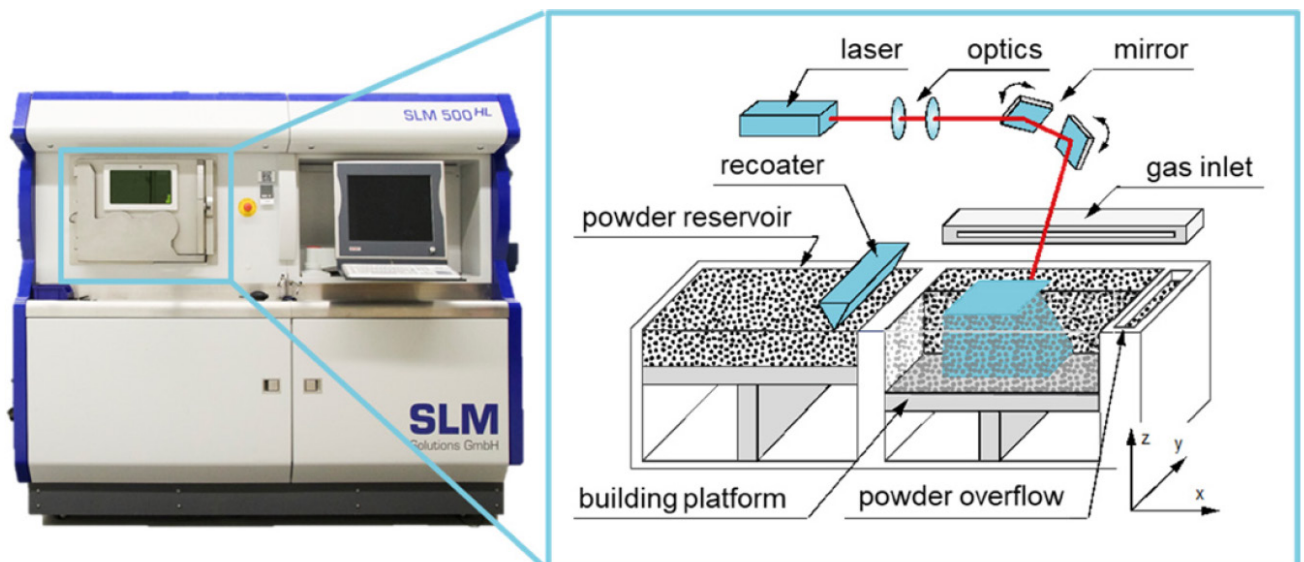


Figure 1-5: Working principle of LPBF processing chamber with main components [21]

LPBF is adopted for production of our experimental In718 superalloys specimens.

1.5.2 LPBF Process parameters

LPBF processing parameters emphasize on controlling parameters, such as laser power ($P = P_v$), scan speed (v), layer thickness (t), scan spacing (h) and scan strategies [16] [23].

In other studies, energy density (E_d) parameter with a unit of (J/mm^2) without layer thickness is used, given by the following equation:

$$E_d = \frac{P(W)}{v(mm\ s^{-1}) \times h(mm)} \dots\dots\dots 1.1$$

Hatch distance (a_1) equation is given by:

$$A_1 = a_1 = \frac{\text{scan spacing } (\mu m)}{\text{track width } (150\ \mu m)} \dots\dots\dots 1.2$$

These parameters are directly linked with material properties, such as porosity, strength, surface roughness [24]. Hence, in this study, we are using volumetric energy density (J/mm^3) equation [25] written as:

$$E_d = \frac{P}{v \times t \times h} \dots\dots\dots 1.3$$

In their work [25], the authors used layer thickness of $20\ \mu m$ while in our work a layer thickness of $30\ \mu m$ is used. All layers thicknesses are constant.

1.5.3 Scan strategy

The scan strategy is the path in which the laser energy density melt powder particles in a PBF to create a layer upon layer at a time. Example of scanning strategies are shown in Figure 1-6.

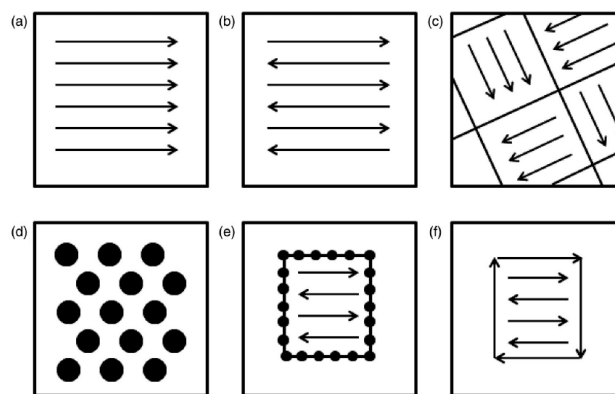


Figure 1-6: Figure: types of scan strategies (a) unidirectional (b) bi-directional (c) island scanning (d) spot melting (e)spot melting contours with snaking fill (f) line melting contours with snaking fill [26]

Figure 1-7 illustrates the types of scan paths which are contour path and fill path found in LPBF. The former is used to fill the edge of the sample while latter melt the powder particles of the sample [27].

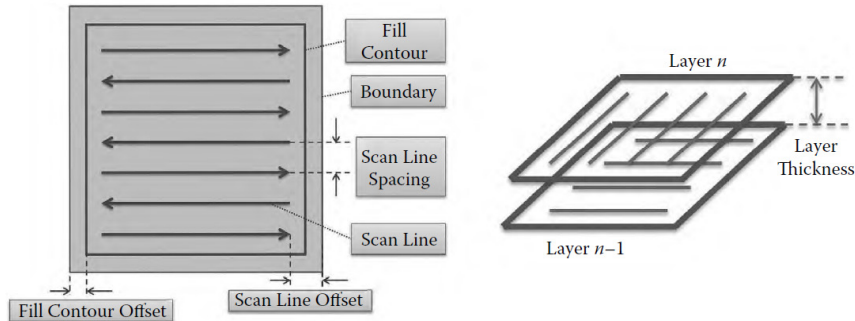


Figure 1-7: Two types of scan paths in LPBF [27]

Scanning strategies with short scanning vectors improve the process stability (refer figure 1-8), reduce the porosity and lower the residual stresses [28]. In other paper, it was explained that scan strategies has effect on the texture component and texture intensity [29].

It has been studied that LPBF operation window as shown in figure 1-8 (in red line), is important to avoid keyholes, lack of fusion, porosities and droplets [30].

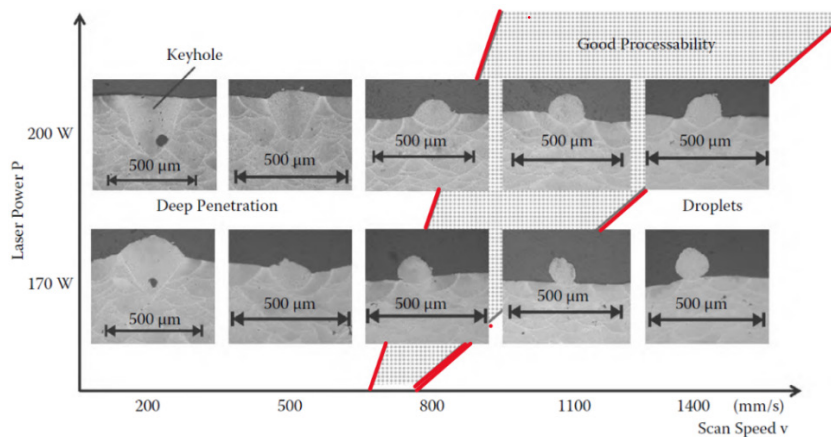


Figure 1-8: Laser power versus scan speed where Processing window is shown in red lines [27]

For example, in case of island strategy shown in figure [1-6 c], no interaction with transverse grain is present and then the structure is similar to many single crystals grouped together (see micrographs in section 5.3.3). The idea is that when this layer has independent single crystals in an island coupled with low modulus in that plane, it can result in 3 to 5 times improvement of rupture life [31].

It has been studied that columnar dendrites grow parallel to building direction of the part [32]. This means that elongation of grains can cause microstructure anisotropies. However, the selection of the correct scan strategy will reduce the heat build up and large island strategy starting with 5 mm x 5 mm lowers residual stresses and no visible effects on the part density and tensile properties anisotropies [33].

Therefore, island scan strategy of 5 mm x 5 mm for a cube specimen of 20 mm x 20 mm x 20 mm, will be adopted for our work [34].

1.5.4 AM Sample orientations

ASTM/ISO design rules [35] requirements for cylindrically and symmetric samples are reported in figure 1-9.

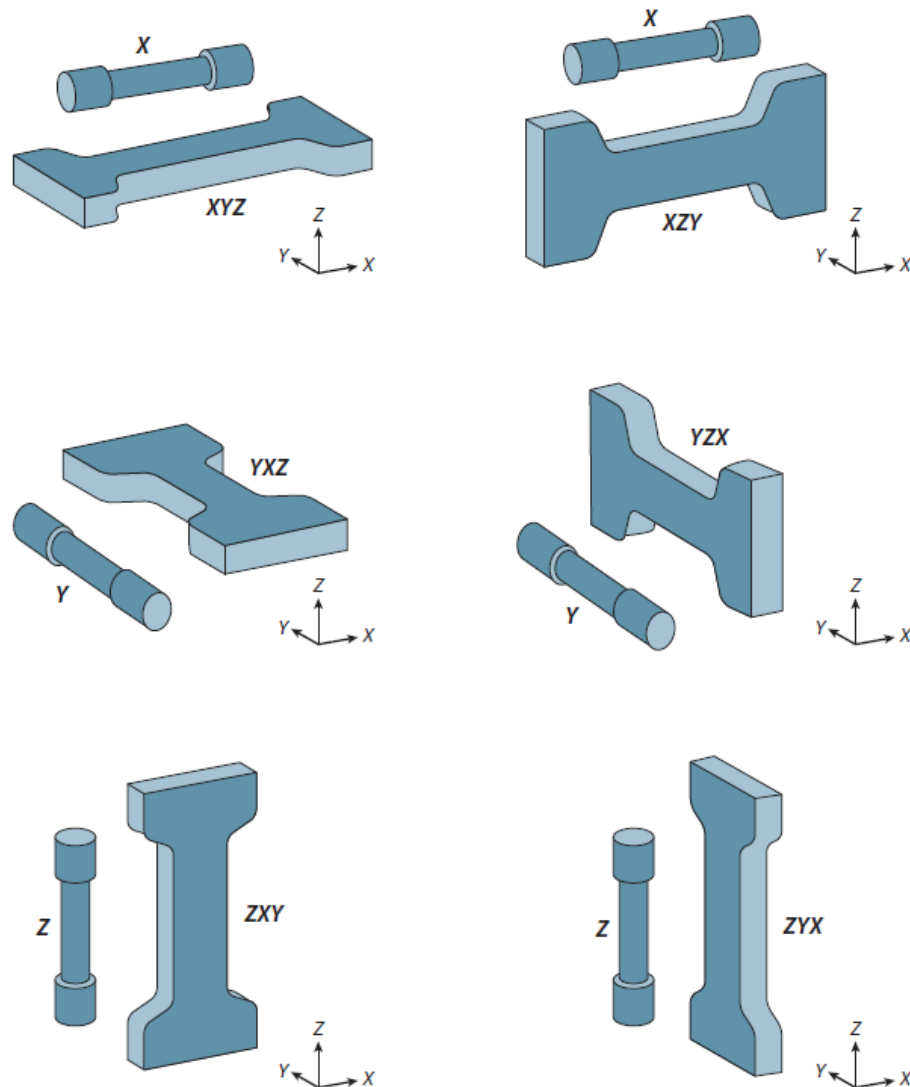


Figure 1-9: Orientation designation for mechanical testing of AM materials

Part build orientation is the key to obtain the required mechanical properties of components [36]. For example, ZX build orientation specimens show lower yield strength compared to XY build orientation specimens.

In this work ZX plane will be used throughout this text meaning that Z axis build direction is longer than X axis and the same definition applies for XY plane. And vertical and horizontal build directions will be termed as perpendicular and parallel deposition build directions in that order.

1.6 Components post processing

This step involves (refer Figure 1-4) both powder removal/supports and heat treatment.

In718 requires heat treatment for residual stress removal. Figure 1-10, TTT illustrates strengthen precipitation of the material is under the guidelines of AMS 5662, 5663 and 5664 [37] [38] in three steps. Also, heat treatment is used to reduce mechanical anisotropy and to produce more isotropic materials or to take advantage of anisotropy for microstructure sensitive design.

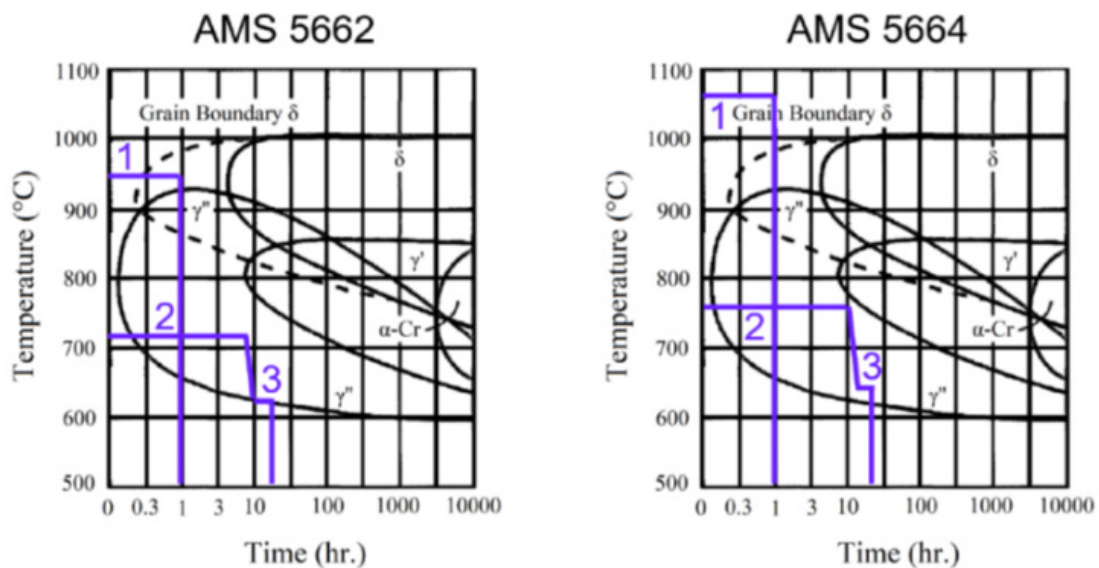


Figure 1-10: Transformation time temperature (TTT) diagram of In718 superalloys [37]

Three steps heat treatment as shown in Figure1-10: 1) is solution treatment, 2) is ageing 1 and 3) is ageing 2.

AMS 2773E has described the following heat treatment steps by considering homogenization, solution heat treatment, stress relieving, stabilization heat treatment, precipitation heat treatment, air cooling, rapid air cooling and thickness of the component.

According to Caliarì et al., [39], heat treatment was performed in three steps (refer to Figure1-11). At 1095°C/1h residual stress removal is obtained. Then, at 955°C/1 h solid solution (carbides and intermetallic phase are fused into γ matrix, boundary segregation is removed) is obtained. The last two ageing steps consist in: ageing 1 (γ' precipitates at 720°C formation) and ageing 2 (precipitates of γ'' at 620°C formation).

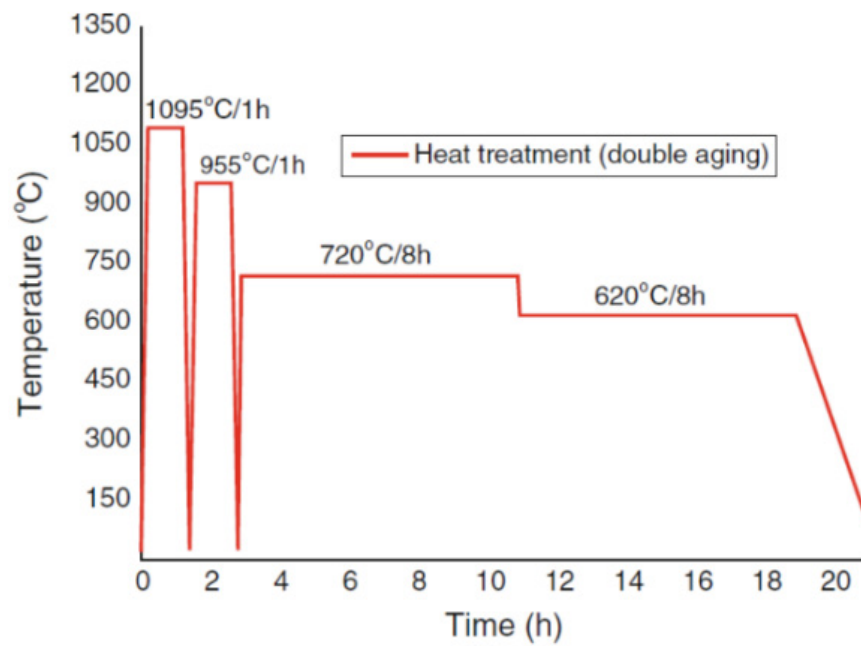


Figure 1-11: Stages of heat treatment for In718 superalloys [39]

1.6.1 Temperature gradient and solidification rate control in AM

Figure 1-12 b, illustrates the solidification rate (R) and temperature gradient (G) variables, which are very important during the AM. An adequate control of these two variables (G and R) results in the reduction of anisotropies sources in both microstructure (porosities, melt pools, elongated grains, crystallographic texture) and mechanical properties (E , σ_y , UTS , E_i).

Heat input (Q_s) is from laser power (P_v) for melting powders on the PBF, hence it is represented by the following equation [40] [41]:

$$Q_s = \frac{f \cdot P_v}{\pi \cdot d^2 \cdot h} \exp\left(-3 \frac{R^2}{d^2}\right) \left(1 - \frac{h}{z}\right) \dots \dots \dots 1.4$$

Where:

Q_s heat input

P_v absorbed laser power

f factor of heat distribution

d beam radius

h depth of the energy source

R radial distance from the laser beam center

z current depth in the thickness direction

Figure 1-12 a, shows the relation between cooling rates and microstructure: lower cooling rate leads to columnar dendrites while faster cooling results in equiaxed dendrites.

Ongoing research has found that elongated grains results in anisotropic tensile properties and microstructure anisotropic. Grain morphology (figure 1-12 b) is given as a ratio of thermal gradient, G to the solidification rate, R [42] [43].

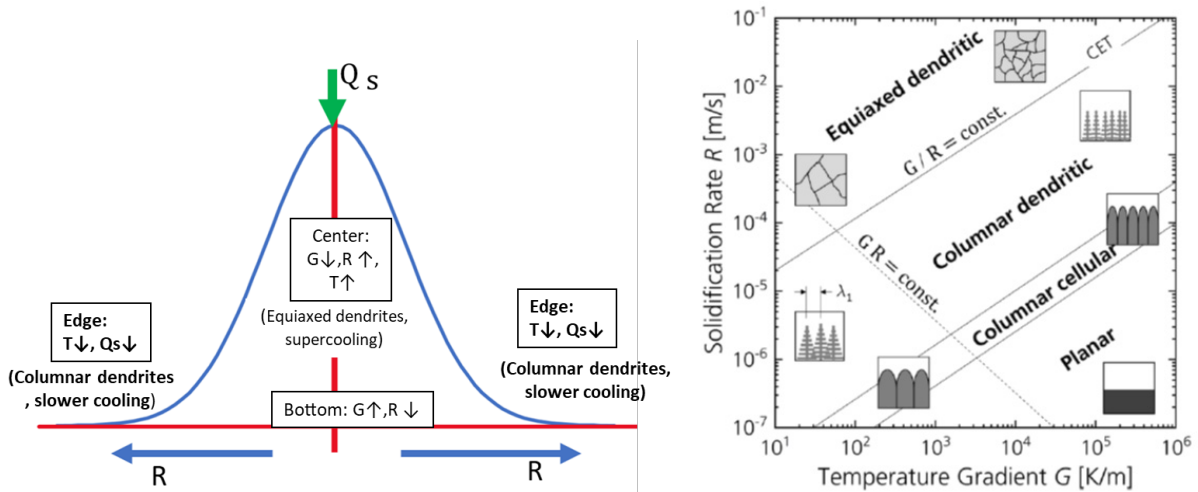


Figure 1-12: (a) schematic curve to show relationship between heat input, grain growth and cooling of melt pool (b) graph showing solidification rate versus temperature gradient [42]

1.7 Types of fracture in monotonic tensile test

Typical tensile fractures are classified into two groups: brittle and ductile fractures. Brittle fracture can be recognized in different forms such as cleavage fracture [44] (figure 1-13 e) where red mark and arrow indicate crack initiation point, transgranular (figure 1-13 a) and intergranular (figure 1-13 b). Ductile fracture can be recognized by the formation of micro voids coalescence (figure 1-13 d) [45] [46]. In our study, cleavage has been mostly observed in all fractures because the tensile test was performed at room temperature. It can be theorized that, as shown in figure 1-13 c, at room temperatures (15-21° C), cleavages and intergranular fractures are prevalent because these fractures absorb less energy than ductile one.

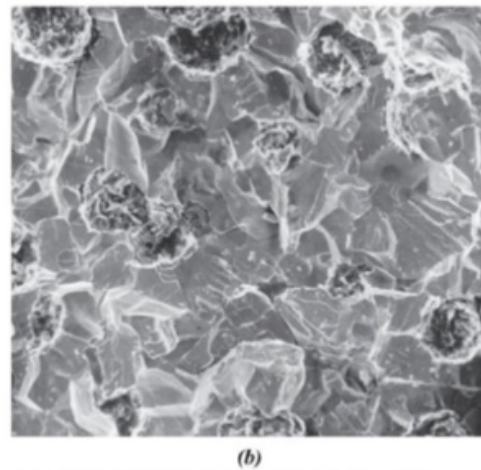
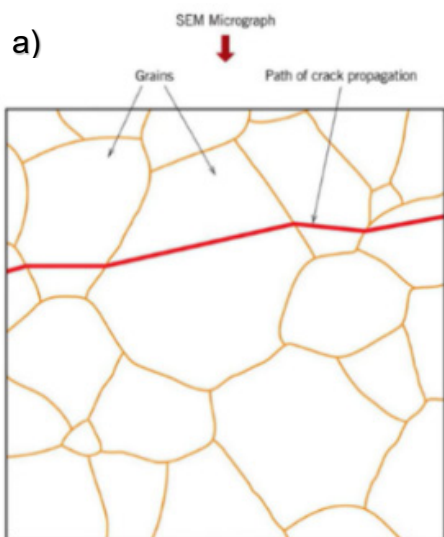


Figure (b) from V. J. Colangelo and F. A. Heiser, *Analysis of Metallurgical Failures*, 2nd edition. Copyright © 1987 by John Wiley & Sons, New York. Reprinted by permission of John Wiley & Sons, Inc.

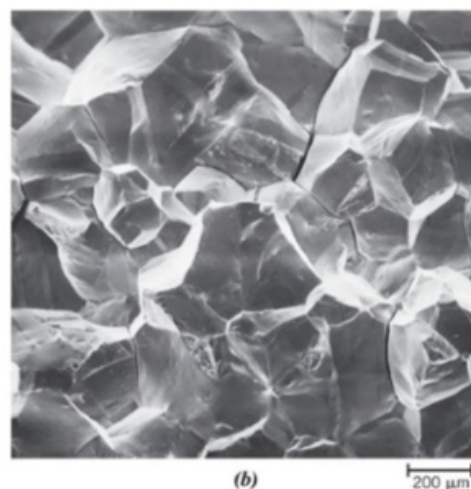
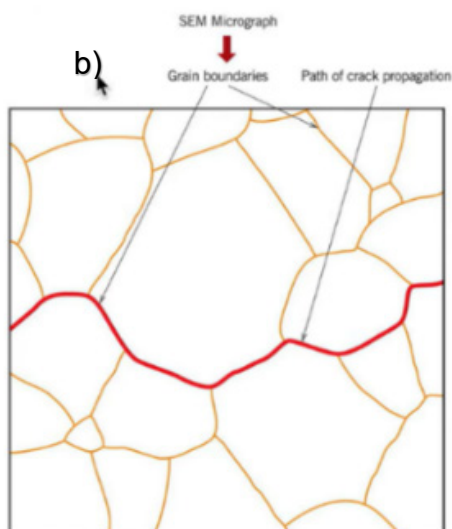


Figure (b) reproduced with permission from *ASM Handbook*, Vol. 12, *Fractography*, ASM International, Materials Park, OH, 1987.

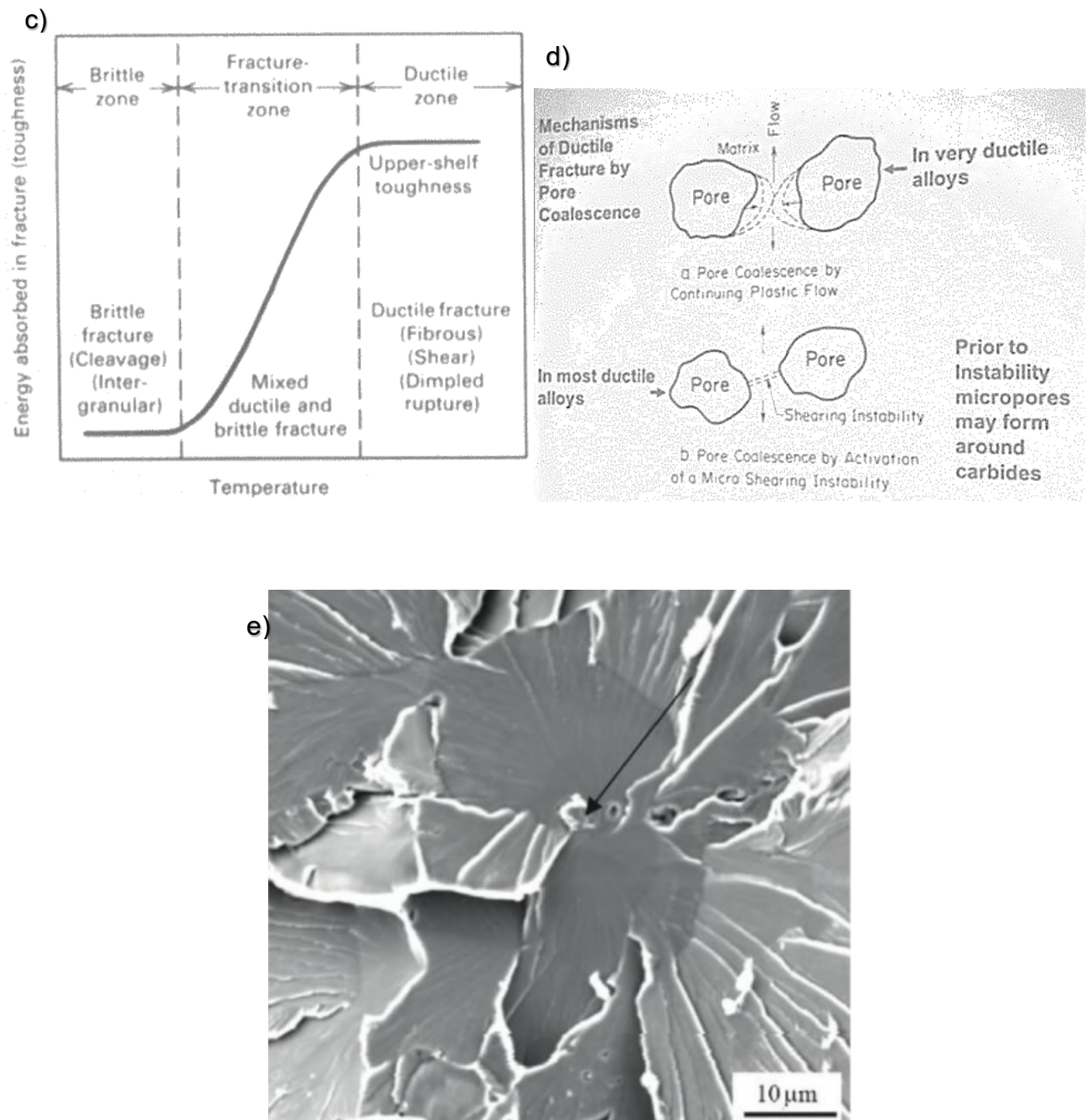


Figure 1-13: (a) brittle fracture due to transgranular fracture, (b) brittle fracture due to intergranular fracture, (c) temperature versus energy absorbed during fracture, (d) ductile fracture due to micro voids formation (e) cleavage fracture [45] [46]

1.8 In718 microstructure defects

By examining the microstructure samples, the quality of parts produced by LPBF can be assessed. In most cases, microstructure cracks and porosities (voids) are characterized by using OM, SEM, EBSD and TEM.

Carter, et al. [47] defined pores are defects of $area > 500 \mu m^2$ ($\varnothing 25 \mu m$). However, cracks (refer to figure 1-14 a) are measured by Feret diameter and are termed as the smaller aspect ratio defects [47] along the build direction. According to Carter [47], large voids with partially melted powder particles occurs in low energy density configuration (refer figure 1-14 b).

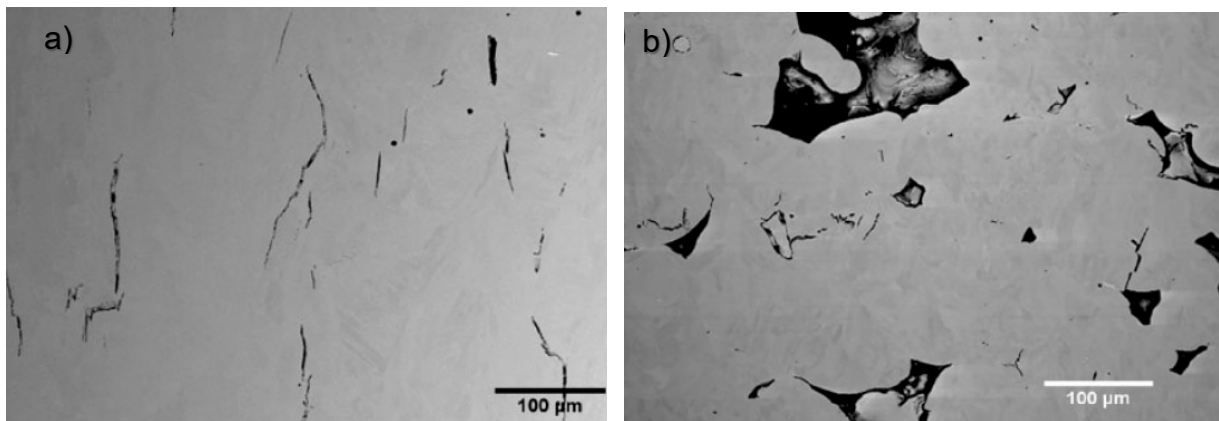


Figure 1-14: Characterization by BSE SEM showing (a) cracks (b) porosities [47]

2 State of the art

2.1 LPBF

In [9], Laser Powder bed fusion, as shown in Figure 2-1 a, was used to manufacture cylindrical rod specimens in three orientations namely perpendicular (ZX), parallel (XY) and inclined at 45° deposition planes as shown in Figure 2-1 (b). The laser power and scan strategies were not stated. As one of the important machines, PBF is widely used in Powder Metallurgy (P/M) to manufacture complex and hard material which cannot be manufactured by conventional processes such as casting, forging and wrought processes.

The key parameters in this LPBF process are laser power, scan speed and powder sizes etc. in order produce the required product in this case Inconel 718 superalloy.

In718 superalloy has **good welding properties**, and this is the reason to be used by AM [2]. Cylindrical specimens (Figure 2-1b) were used in tensile testing in order to obtain their yield strength, ultimate tensile strength and elongation at fracture.

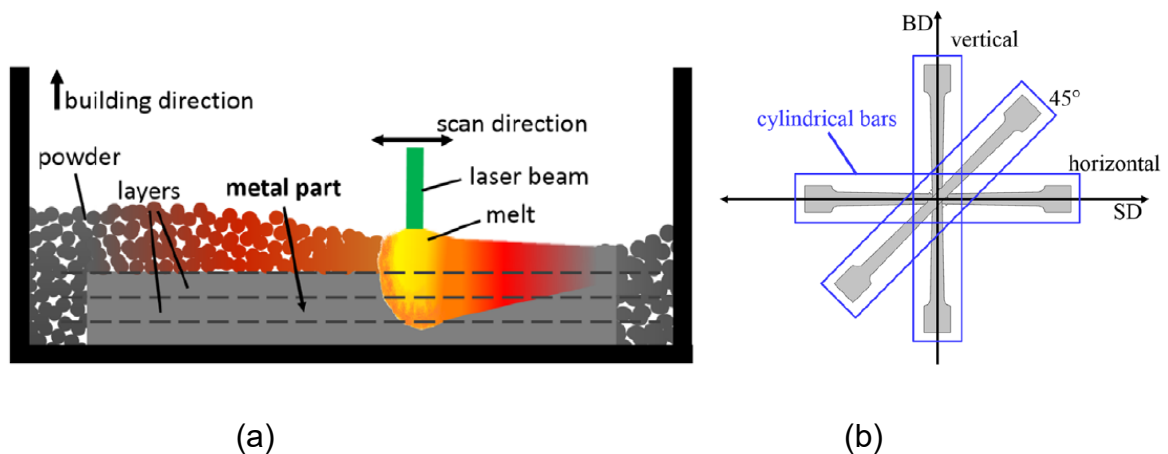


Figure 2-1: (a) Laser Powder Bed Fusion(L-PBF), (b) Cylindrical Dog bones at different build orientations Horizontal (XY) build, and vertical orientation build (ZX) and at an angle of 45° [9]

Figure 2-2 shows the specimens obtained with laser power of 950 W and 250 W used during manufacturing of cube specimens [9]. Later, these workpieces were etched by Kalling's reagent to reveal their microstructures under OM. No scan strategy was explained.

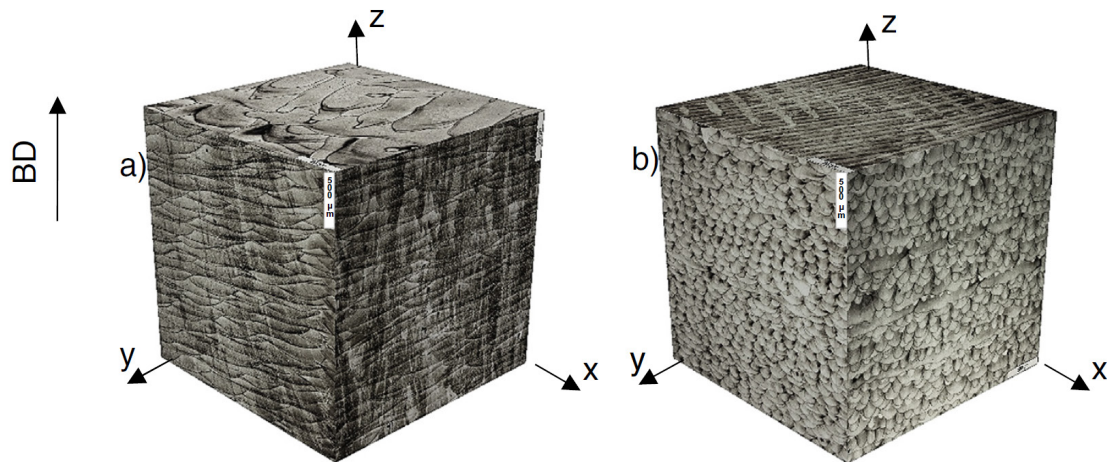


Figure 2-2: 3D cubes of 2 mm³ showing the top view (XY), right view (YZ), front view (ZX) microstructures processed power of (a) 950 W and (b) 250 W at a magnification of 500 μm [9]

Samples in Figure 2-1 and Figure 2-2 are different than the ones of our work because of the difference in chemical composition, crystal texture and laser operating parameters.

2.2 Anisotropic Mechanical properties

Causes of tensile anisotropy properties (including elastic modulus (E), yield strength (σ_y), ultimate tensile strength (UTS), elongation (E_l)) are elongated grains and texture [48] [49]. In Table 2-1 the characterization methods to observe and quantify these tensile anisotropies are summarized.

Table 2-1: Overview of anisotropic causes

Causes of anisotropy	Main tensile property anisotropy	Minor tensile property anisotropy	characterization instruments
Crystal texture	E, σ_y	UTS, E_l	EBSD, XRD
Elongated columnar dendrites		σ_y	OM, SEM, EBSD
phases	E_l		OM, SEM, EDS, EBSD, TEM
Lack of fusion defects	E_l		OM, X-ray microtomography
Melt pools	E_l		OM, SEM

2.2.1 Tensile property anisotropy:

E_l anisotropy is due to elongated columnar dendrites, undesirable phases, lack of fusion, porosities and melt pools. While σ_y , UTS and E anisotropies are caused by the crystallographic texture.

Tensile properties anisotropies can be quantified by equation 1.5 [50]:

$$\frac{\sigma_x - \sigma_z}{\sigma_x} \times 100\% \dots \dots \dots 1.5$$

In our work, σ_x means UTS or σ_y in X direction while σ_z means UTS or σ_y in Z direction; same applied for the E and E_l .

2.2.2 AM of In718 tensile properties anisotropies from literature review

Table 2-2: Summary of AM In718 tensile properties anisotropies

Machine type	Post processing	Speciment orientation	E (MPa)	Yield strength (MPa)	Ultimate tensile strength (MPa)	Elongation (%)	Reference
SLM	HT	XY	-	1227±1	1447±10	10.1±0.6	[18]
		Z		1136±16	1357±5	13.6±.2	
	AS	XY	-	816±24	1085±11	19.1±0.7	
		Z	-	737±4	1010±10	20.6±2.1	
EOS M280	HT	XY	-	1068	1344	27	[51]
		Z		1034	1309	27	
EOS M280	AS	SS XY	-	562.22	720		[29]
		SS X		621.46	821		
-	HT	Flat built(0°)		1295	1484		[52]
		Upright(90°)		1240	1398		
SLM 280HL	AS	-	-	569 - 646	851 - 1002	9.8-31.7	[53]
	HT	-		1160	1350	17,6	
Laser/wire	HT	-	-	1079	1314	20.4	[54]
DLD	HT	-	-	1034	1276	12	[55]
DLD	HT			1097.6	1321	9.8	[56]
EBF ³	HT	XY	174	986	1114	-	[57]
		YX	192	998	1162		
	AS	XY	138	655	978		
		YX	194	699	936		
EBF ³	AS	XY	159	580	910	22	[58]
Laser	HT	-	-	1133	1240	9	[59]
	AS			590	845	11	
DLD	HT	Z	-	1257	1436	-	[60]
	AS			650	1000		
SMD	AS	XY	-	473±6	828±8	28±2	[61]

The chemical composition from the literature review in Table 2-2 is different from our samples. This means that there is difference in order of magnitude results as shown in table 5-1.

According to Matthew., et al [1], varying microstructures will result in varying test results (such as yield strength, *UTS*, creep strength, stress-rupture strength, fatigue strength, dynamic modulus, crack growth rates, fracture toughness thermal expansion coefficient and density). Therefore, varying microstructures can be caused by a number of reasons such as sample deposition plane (XY or ZX), chemical composition, post processing, quality of powder (virgin, used, overflow, spatter), laser power, temperature and so on.

2.3 Anisotropic microstructures:

Main causes of microstructure anisotropies are crystallographic texture, lack of fusion defects, elongated grains, melt pools, and residual stresses. A texture is characterized by a component (crystal orientation) and its intensity (multiple of uniform distribution or *m.u.d.*). Wang Y., et al, showed nickel base superalloy In718 texture control with laser power and laser power profile shape [62].

2.3.1 Electron backscattering diffraction (EBSD)

Microstructure texture or crystallographic texture are characterized by SEM-EBSD. This is very important technique to observe the appearance of the grain growth in In718 superalloys.

Helmer et. al. analysed the appearance of texture in perpendicular deposition plane and it resulted that the elongation of texture can be highlighted as in figure 2-3 in red colour [36]. Elongated grain are obtained with $E_d=1.8 \text{ Jmm}^{-2}$ and equiaxed grains are produced at $E_d=1.9 \text{ Jmm}^{-2}$.

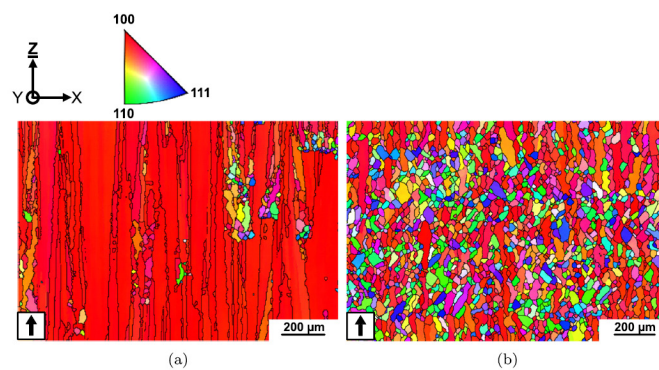


Figure 2-3: EBSD orientation maps in longitudinal section to ZX orientation (a) elongated columnar grains (b) equiaxed grains

Figure 2-4, SEM-EBSD shows microstructure of parallel deposition orientation where an island scan strategy is seen and can be compared to figure 5-10 a. Red color shows elongated columnar grain across the microstructure [32].

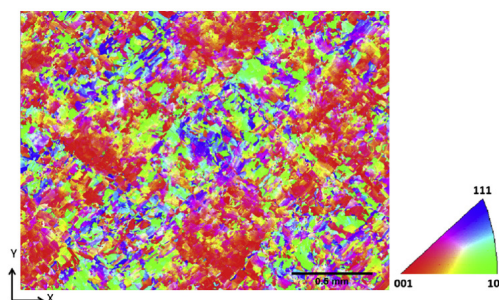


Figure 2-4: IPF EBSD map showing the effect of the scan pattern on grain orientation [32]

2.3.2 Transmission Electron Microscope (TEM)

TEM is used to characterize the phases of alloys as shown in figure 2-5. In this case, what phases (for example laves and γ matrix [63]) are in the material and other precipitates (γ' , γ'' , σ , δ , μ ,) can be observed.

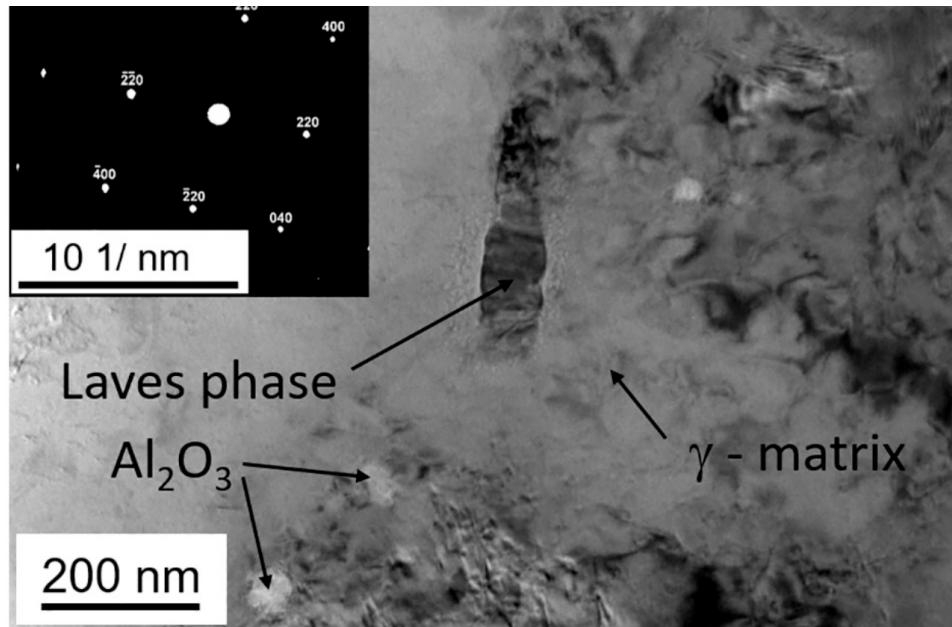


Figure 2-5: TEM micrographs with SAED patterns of Laves phases [63]

2.3.3 Scanning Electron Microscope (SEM)

2.3.3.1 Fractography analysis

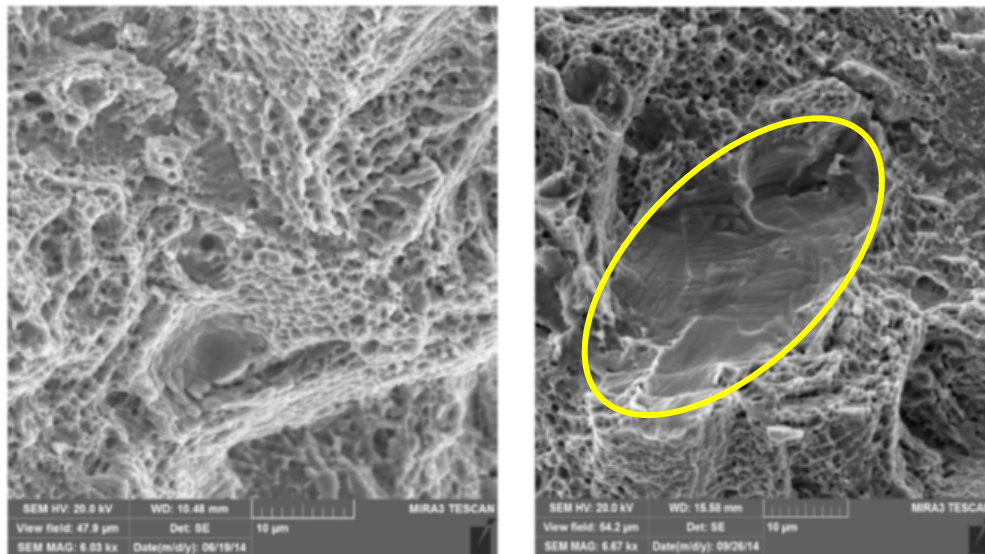


Figure 2-6: Fractography surfaces of In718 superalloys samples (a) AS sample (b) HT sample [53]

Popov et al., [53], SEM micrograph in Figure 2-6 a and b, shows a ductile transgranular fracture due to the micro voids coalescence and dimples. But, in figure 2-6 b, illustrates the HT sample with brittle undulate facet (yellow ellipse) surrounded by large number of micropores which are ductile.

2.3.3.2 Microstructures analysis

Figure 2-7 a, OM illustrates AS perpendicular orientation where elongated columnar dendrites grows parallel to the heat input. A transverse section shown in figure 2-7 b, shows melt pool with columnar dendrites [53].

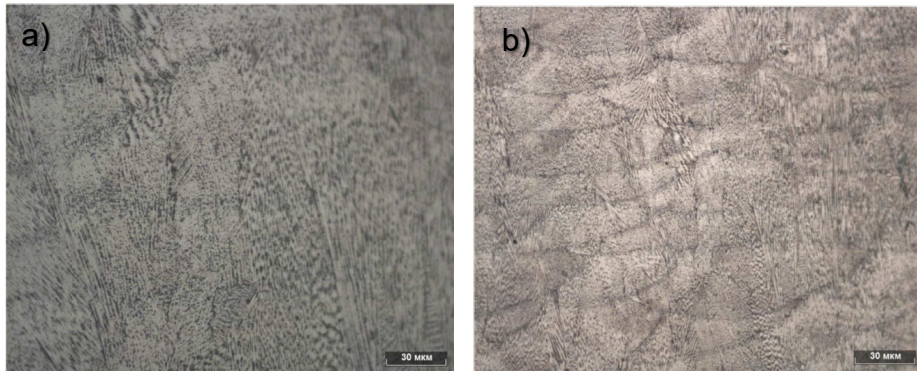


Figure 2-7: In718 superalloys samples AS produced by SLM: a) longitudinal section, b) transverse section [53]

After ageing the microstructure of In718 as shown in Figure 2-8, uniformly distributed precipitates are achieved [53] to both the longitudinal and transverse sections.

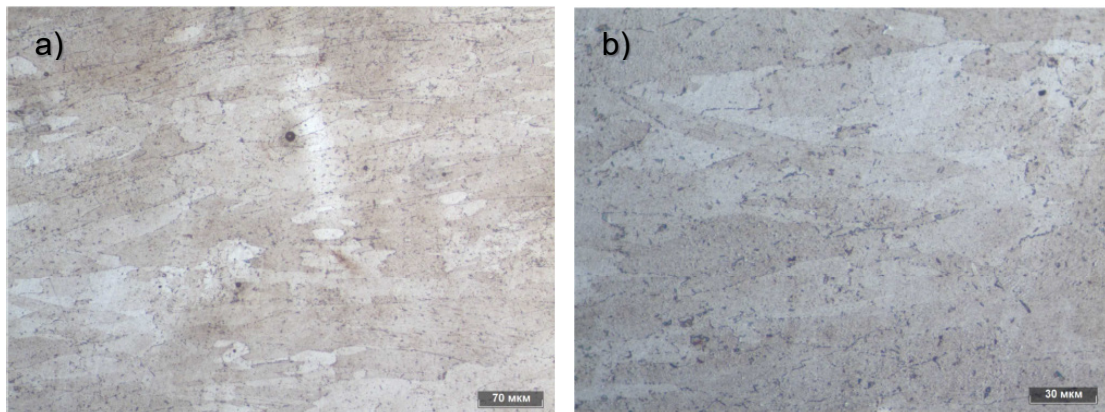


Figure 2-8: In718 superalloys samples after homogenization + aging produced by SLM: a) longitudinal section, b) transverse section [53]

3 Problem and research objective

Motivation question to be investigated:

- To identify the main sources of tensile and microstructures anisotropies in Inconel 718 superalloys samples produced by Laser powder bed fusion (LPBF) in AM.

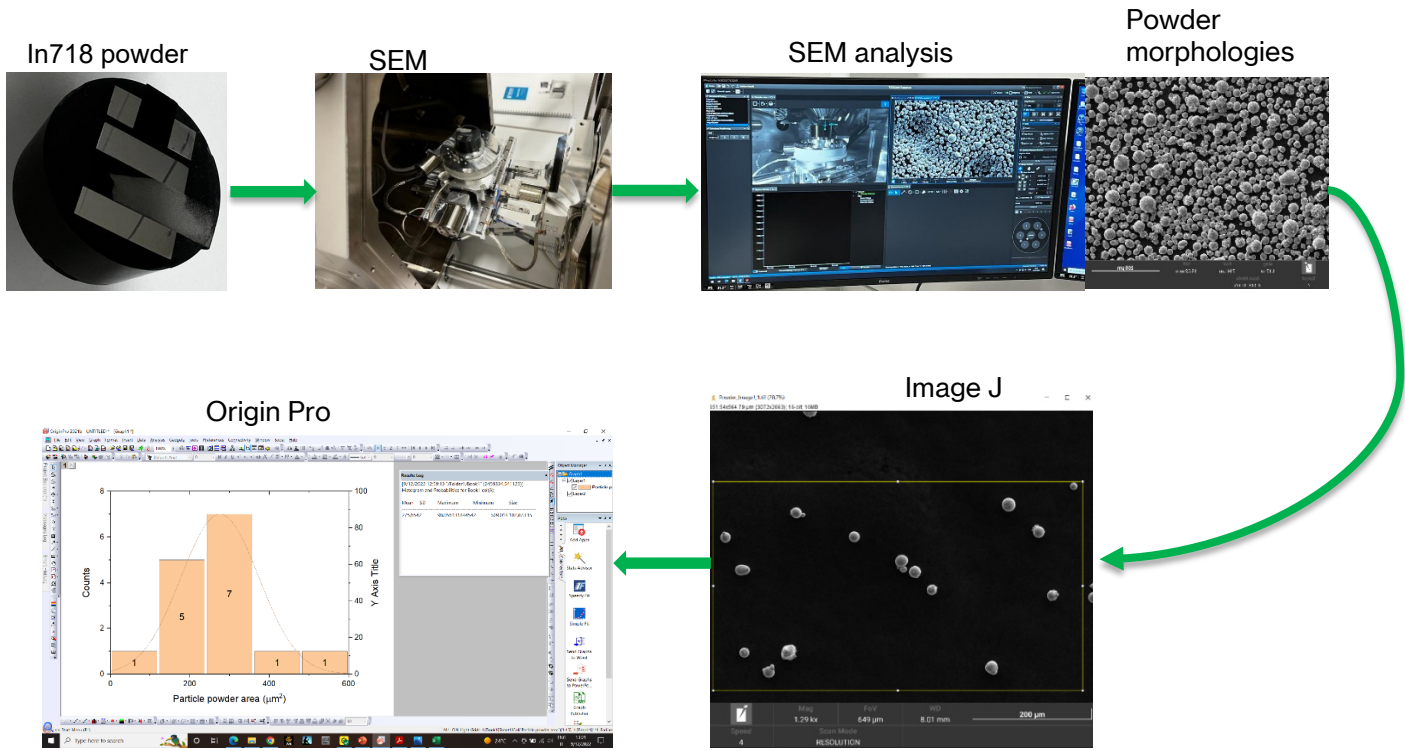
Specific Objectives:

- Perform tensile test on cylindrical samples to obtain the fracture surfaces.
- Analyze **AS cylindrical specimens fracture surface on SEM** for perpendicular (ZX) sample. Note for AS parallel (XY) sample is not available.
- Analyze **HT- cylindrical rod specimen fracture surface on SEM** for parallel (XY) orientation samples. Note for HT perpendicular (ZX) sample is not available.
- Analyze the **AS cubic microstructures on Optical Microscopy (OM)** for both specimens in perpendicular (ZX) and parallel (XY) orientations
- Analyze the **HT-cubic microstructures on Optical Microscopy (OM)** for both specimens in perpendicular (ZX) and parallel (XY) orientations

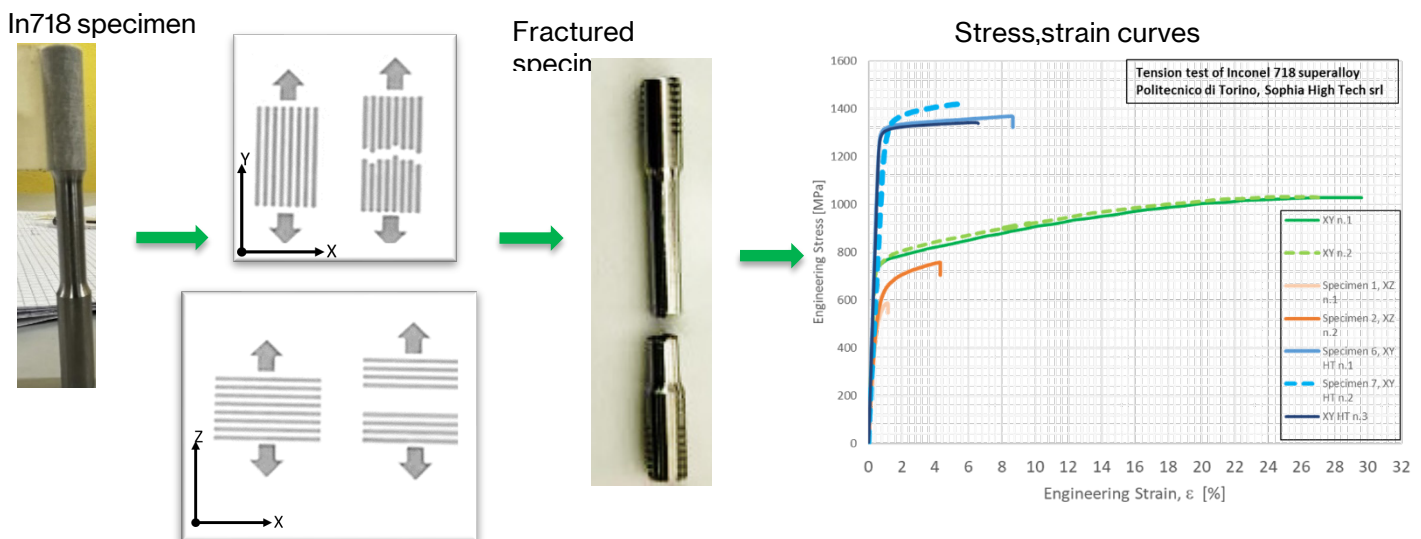
4 Materials and methods

4.1 Experimental plan

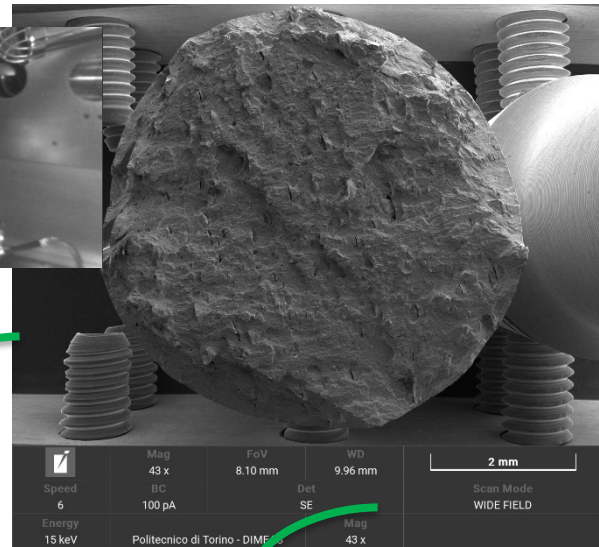
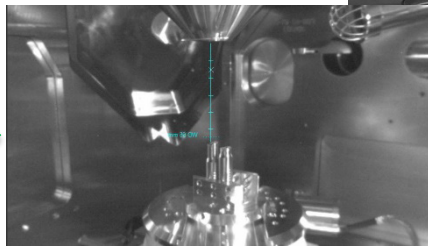
4.1.1 Powder morphologies and size distribution



4.1.2 Data acquisition to compute yield strength, UTS, elongation

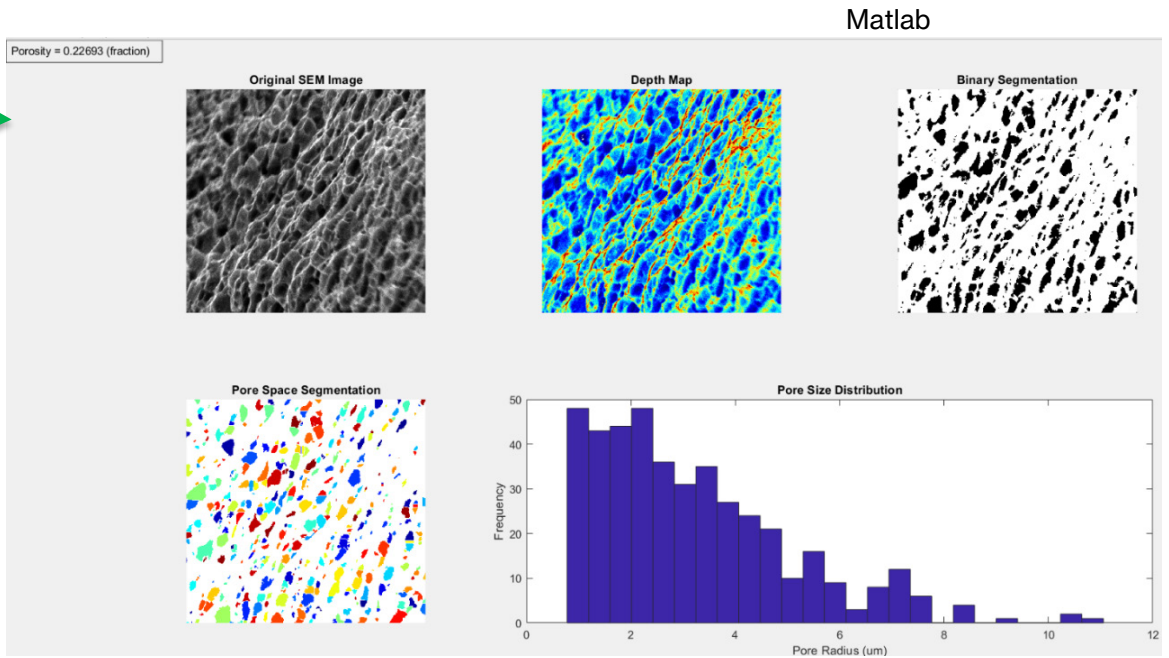
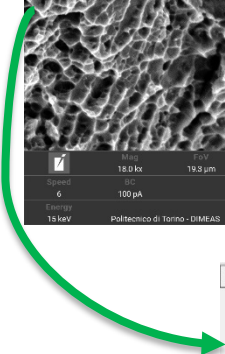
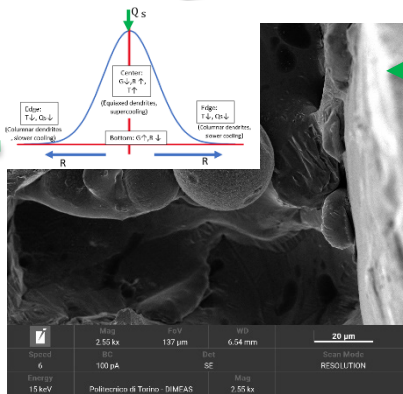
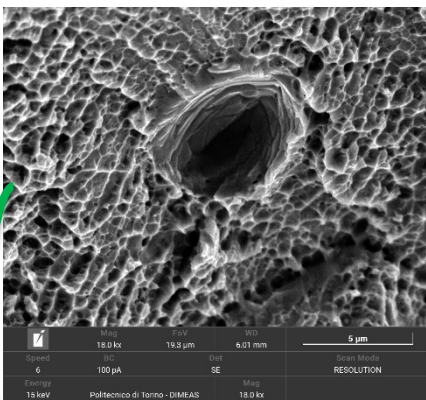


4.1.3 Analyse the anisotropic microstructures of fractured surfaces and defects

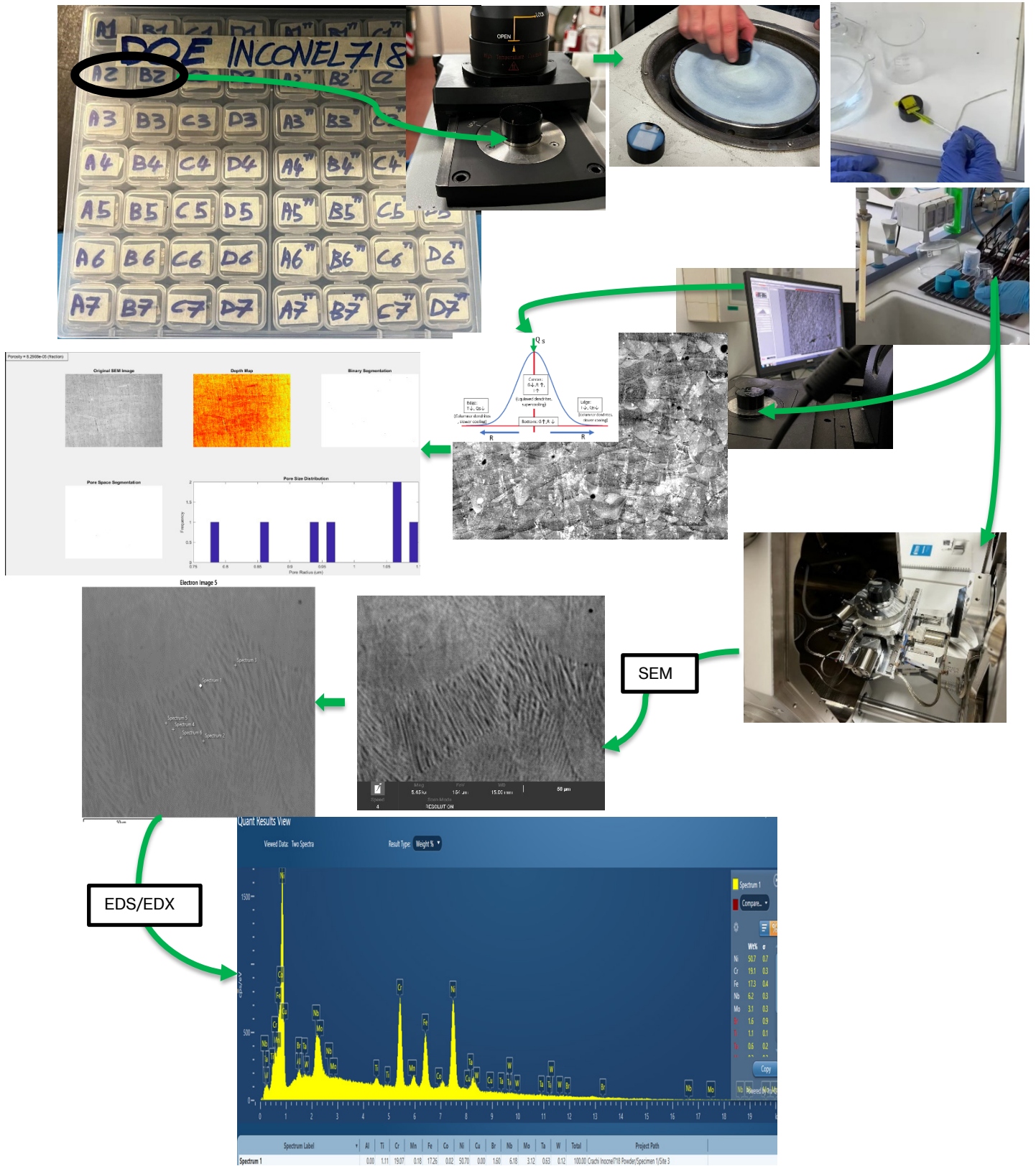


Microstructure at high magnification

Microstructure at high magnification



4.1.4 In718 superalloy cubes: analysing the anisotropic microstructures and chemical composition



4.2 Specimens

4.2.1 Chemical compositions

The chemical composition of In718 was obtained from Sophia High Tech s.r.l, table 4-1 and were later compared by EDS map as explained in section 5.5.

Table 4-1: Chemical composition of In718 superalloy

Elements	Name	Units	Min	Max	Result
C	Carbon	Weight %	0	.08	.03
Fe	Iron	Weight %	bal		Bal (= 18.924)
N	Nitrogen	Weight %	0	.03	.01
O	Oxygen	Weight %	0	.03	.01
Cu	Copper	Weight %	0	.3	<.1
B	Boron	Weight %	0	.006	<.001
Co	Cobalt	Weight %	0	1	.1
Al	Aluminium	Weight %	.2	.8	.53
Ti	Titanium	Weight %	.65	1.15	1.01
Nb + Ta	Niobium + Tantalum	Weight %	4.75	5.50	4.92
Mo	Molybdenum	Weight %	2.8	3.3	3.10
Ni	Nickel	Weight %	50	55	52.30
Cr	Chromium	Weight %	17	21	18.9
S	Sulphur	Weight %	0	.015	.001
P	Phosphorus	Weight %	0	.015	.004
Si	Silicon	Weight %	0	.35	.04
Mn	Manganese	Weight %	0	.35	.02
Total					81.076+ Bal (18.924)

Nickel as the main alloying element has 52.3% by weight followed by Iron and chromium at 18.92% and 18.9% by weight respectively. This is the reason is called nickel-base superalloy because % weight of nickel is more than half of other alloying elements.

4.2.2 Specimen orientations and geometry

Our specimens were produced both in ZX and XY orientations refer table 4-2. Refer for detail views in appendix A and B.

Table 4-2: Specimens Geometry and orientation

Specimens	ID	Post processing	
Cylindrical: Parallel orientation(XY)	Specimen 6	-	HT
	Specimen 7	-	HT
Cylindrical: Perpendicular orientation(ZX)	Specimen 1	AS	-
	Specimen 2	AS	-
Cube: perpendicular orientation(ZX)	A2.1	AS	
	A2.2		HT
Cube: parallel orientation(XY)	B2.1	AS	
	B2.2		HT

4.2.3 Laser Process parameters

The following data (table 4-3) were obtained from The Sophia High Tech s.r.l and Politecnico di Torino (DIMEAS) that were used during the production of our In718 superalloy specimens.

Table 4-3: LPBF Processing parameters for In718 superalloys

Body	Layer thickness[mm]	0.03
	Spot size[mm]	0.15
	Trace width [mm]	0.105
	Overlap factor A1	0.7
	Power[W]	192
	Body velocity[mm/s]	600
Contour	Power[W]	192
	Spot size [mm]	0.15
	Beam compensation [mm]	0.075
	Contour velocity[mm/s]	1600
	Hatch zone boarder [mm]	0.065

4.2.4 Heat treatment of In718 samples

According to Mostafa, et al., [49] as shown in Figure 4-1, Time-Temperature-Transformation (TTT) has been adopted to our work.

The specimens underwent stress relief 1050 °C/ 1h and then solution annealed approximately 950 °C/ 1 hours and air cooled (AC). Next, the specimens underwent ageing 1 starting at 720°C/8h/FC and at last ageing 2 was applied at 620°C/8 hours/AC.

According to **AMS 2773E** the material must undergo homogenization, solution heat treatment and ageing. The first ageing is the formation of γ' precipitates on the γ fcc matrix and the second ageing is to cover γ' with precipitates of γ'' hence strengthened hardened by precipitates.

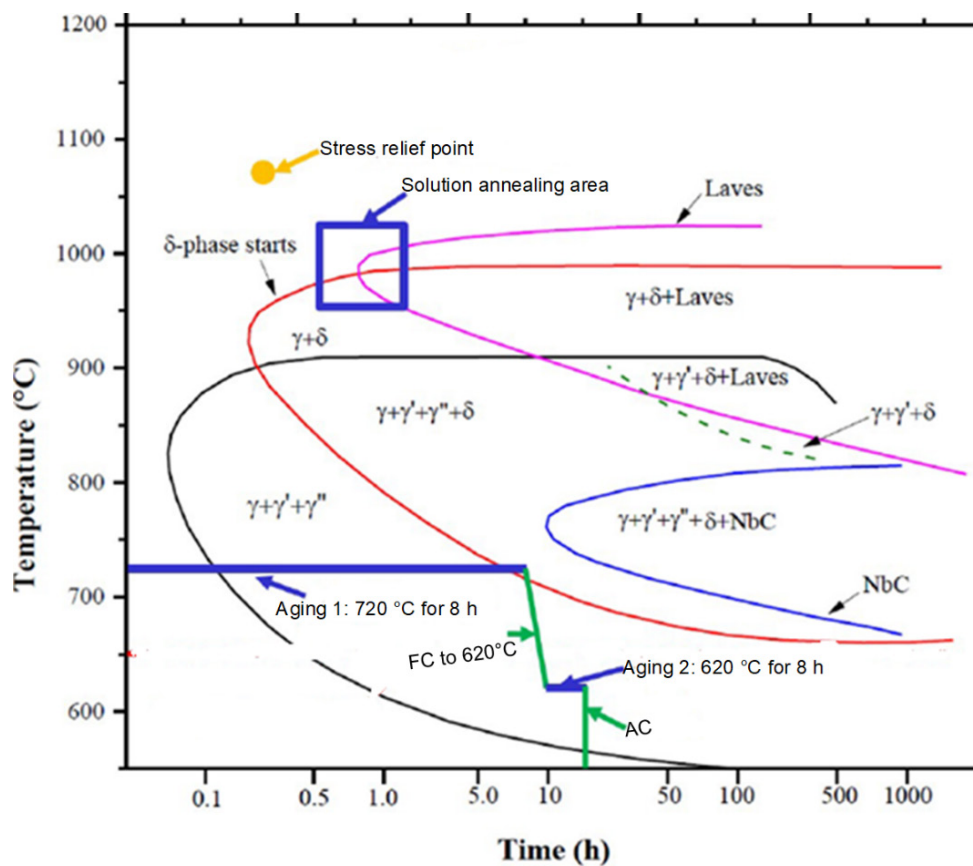


Figure 4-1: TTT diagram for In718 [49]

4.3 Equipments

4.3.1 Tensile test machine



MACHINE FEATURES	
Constructor	Zwick/Roell
Model	Z050 THW
Load F_N in tensile/compression direction	50 kN
Load cells	- XForce HP 5 kN accuracy class 1 (from 0,2% of F_N): 10 N - XForce HP 50 kN accuracy class 1 (from 0,2% of F_N): 100 N
Test area width	640 mm
Height of lower test area, without accessories	1325 mm
Height of upper test area, without accessories	1365 mm
Crosshead speed up to 110% of test load (v_{min} ... v_{Nom})	0,0005 ... 600 mm/min
Increased crosshead return speed(at reduced force)	1000 mm/min
Drive system's travel resolution	0,31789 nm
Testing temperature	RT up to 1200 °C
Non-contact strain measurement without marking	laserXtens 2-220 HP - Class 0,5 EN ISO 9513 - Resolution 0,07 μ m according to EN ISO 9513 under real testing conditions - Gauge length 3 – 200 mm - Max. following speed on the specimen 500 mm/min
Furnace specifications	MAYTECH HTO-39-DSO Double slot furnace up to 1200 °C - Max. heating rate: 20 °C/min - Protective gas: Argon - Inner heating area: diameter 100 mm, height 300 mm - 3 Termocouples: Type N to measure the temperature of sample in the upper, middle and lower part

Figure 4-2: Tensile test machine, type Zwick mod 50kN (DIMEAS)

4.3.2 Polishing machine



Figure 4-3: Metallographic preparation machines (a) specimen mold machine (b) polishing machine (DIMEAS) (c) Polishing machine (DISAT)

4.3.3 *Optical microscopy*

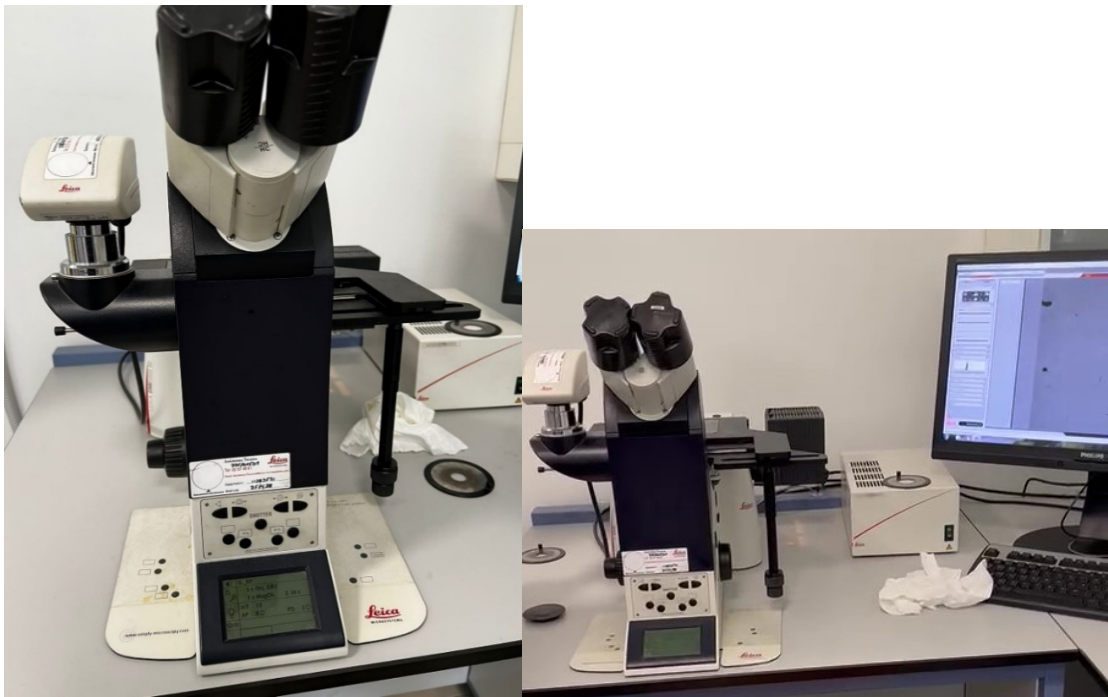


Figure 4-4: Optical microscopy (DISAT)

4.3.4 *SEM*

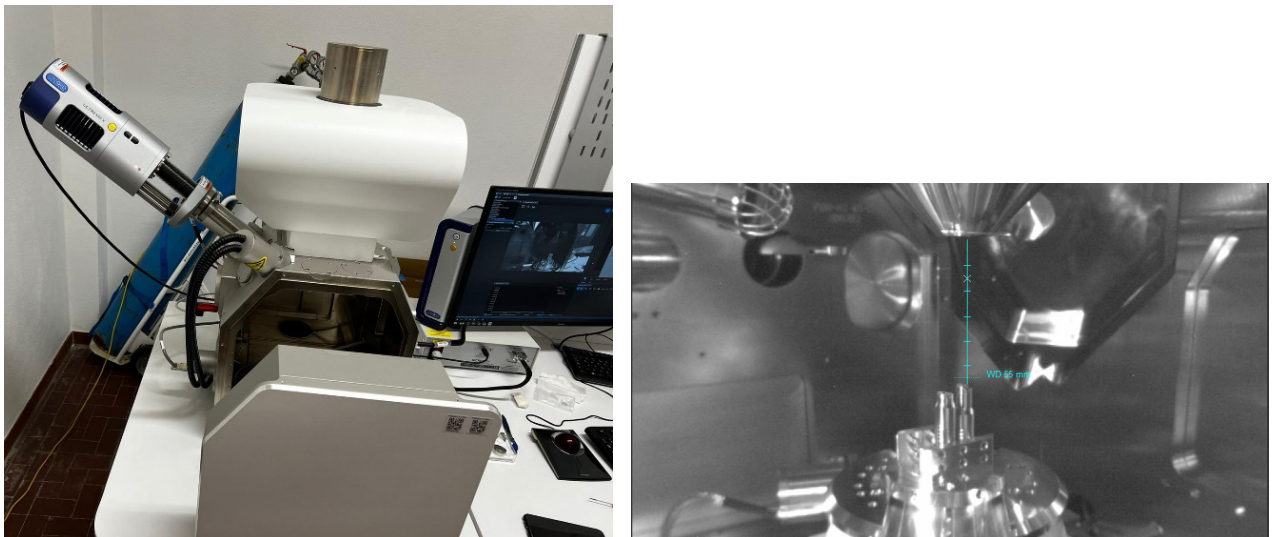


Figure 4-5: Scanning Electron Microscopy (DIMEAS)

4.4 Tensile test and characterization of In718 samples

4.4.1 Tensile test procedure

In order to reveal the fracture surface of In718 cylindrical specimens, a Zwick mod 50kN tensile testing machine (refer figure 4-2) was performed at room temperature. Table 4-4, describes the tensile test settings that were used. The AS perpendicular and HT parallel deposition build specimens with a diameter of 6.249 mm and 6.24 were tested respectively. The strain rate was 2 mm/min until the fracture occurred.

Table 4-4: Tensile test parameters

Test location	Politecnico di Torino	Politecnico di Torino
File name	inconel_AD_P2	inconel_AD_P6
Testing equipment	Zwick mod 50kN	Zwick mod 50kN
Speed [mm/min]	2	2
Diameter [mm]	6.249	6.24
Area [mm ²]	30.67	30.58
Preload [MPa]	5	5
L ₀ gauge length [mm]	20	20
Deposition direction	Z	XY
TT	NO	YES
Test Number	2	1

4.4.2 Acquired data

After the completion of the tensile test the tensile strain (%) and stress (MPa) data were collected. These two parameters will be used for computation of E , $Rp_{0.2}$, UTS, E_t .

4.4.3 Tensile test parameters:

The following parameters were computed E , $Rp_{0.2}$, UTS, E_t . For 0.2% offset strain the following equation were used:

$$y = mx + b \dots \dots \dots 4.1$$

$$\sigma = E\varepsilon + b \dots \dots \dots 4.2$$

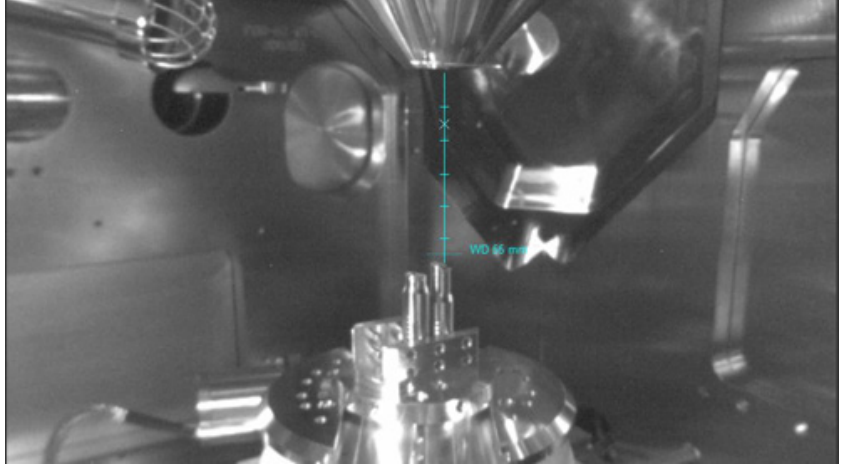
$$x = -\frac{b}{m} \dots \dots \dots 4.3$$

These parameters from equation 4.1 to 4.3 were used to plot the engineering strain versus engineering stress, the result graphs are in section 4.2.

4.4.4 SEM: Fracture surface analysis



SEM vice with broken In718 samples



Inside SEM chamber

Procedures:

- 1 Wear gloves before touching anything
- 2 Vernier caliper: Measure the specimen size in relation to setting the beam height
- 3 Dust remover: Spray on the specimen and SEM vice then mount the vice to SEM chamber
- 4 Secure the vice onto the SEM chamber with screw driver
- 5 Close the SEM ready for visualizing the fracture surfaces/cube and In718 samples
- 6 Analyse the fracture surface by SEM software and save the images results

4.4.5 OM : metallography preparation

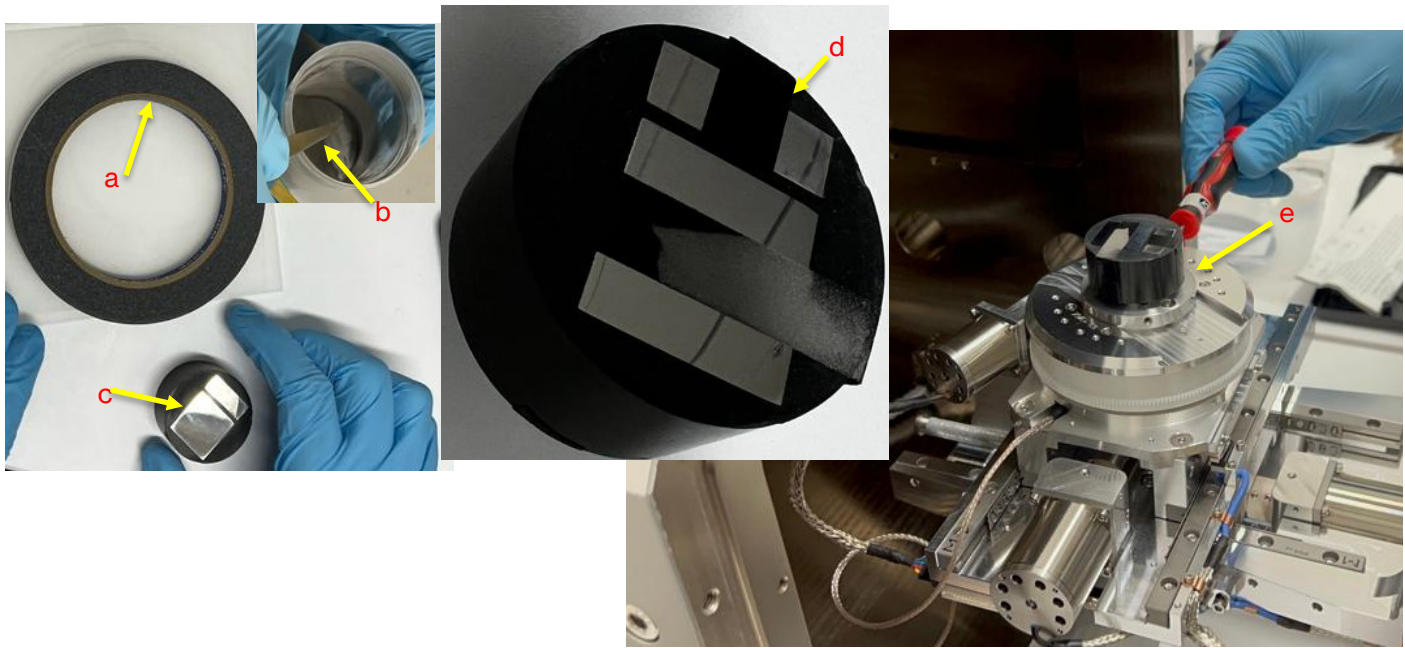


a	Kalling's chemical bottles
b	Kalling's reagent (2g CuCl_2 , 40 ml HCl, 40-80 ml Ethanol)
c	Magnetic mixer
d	Water to clean the cube surface after etching
e	Cube specimens in ZX and XY under chemical etching by Kalling's

Procedures:

- 1 Prepare chemical etchant
- 2 Chemical attack the cube surface for 5 seconds
(Otherwise, the chemical will burn the surface and start the whole process of polishing)
- 3 washes with clean water
- 4 dry the specimen before place on OM
- 5 place the etched surface to observe/characterize the microstructure
- 6 analyse the microstructure and save the images results

4.4.6 EDS maps : Chemical analysis on the microstructure and In718 powder



a	Double side sole tape
b	In718 powder particles
c	Cube specimens
d	Cube specimens and In718 powder
e	SEM chamber where cube specimens and In718 powder are mounted

Procedures:

- 1 Sole tape: divide etched area and unetched area of both ZX and XY
- 2 In718 powder is spread on top of the sole tape
- 3 Secure the specimen into the SEM chamber, close and pressurize the chamber
- 4 Analyse the microstructure by EDS/EDX software and save the images results

5 Results and discussions

5.1 Inconel 718 Powder analysis

5.1.1 In718 powder particle morphology

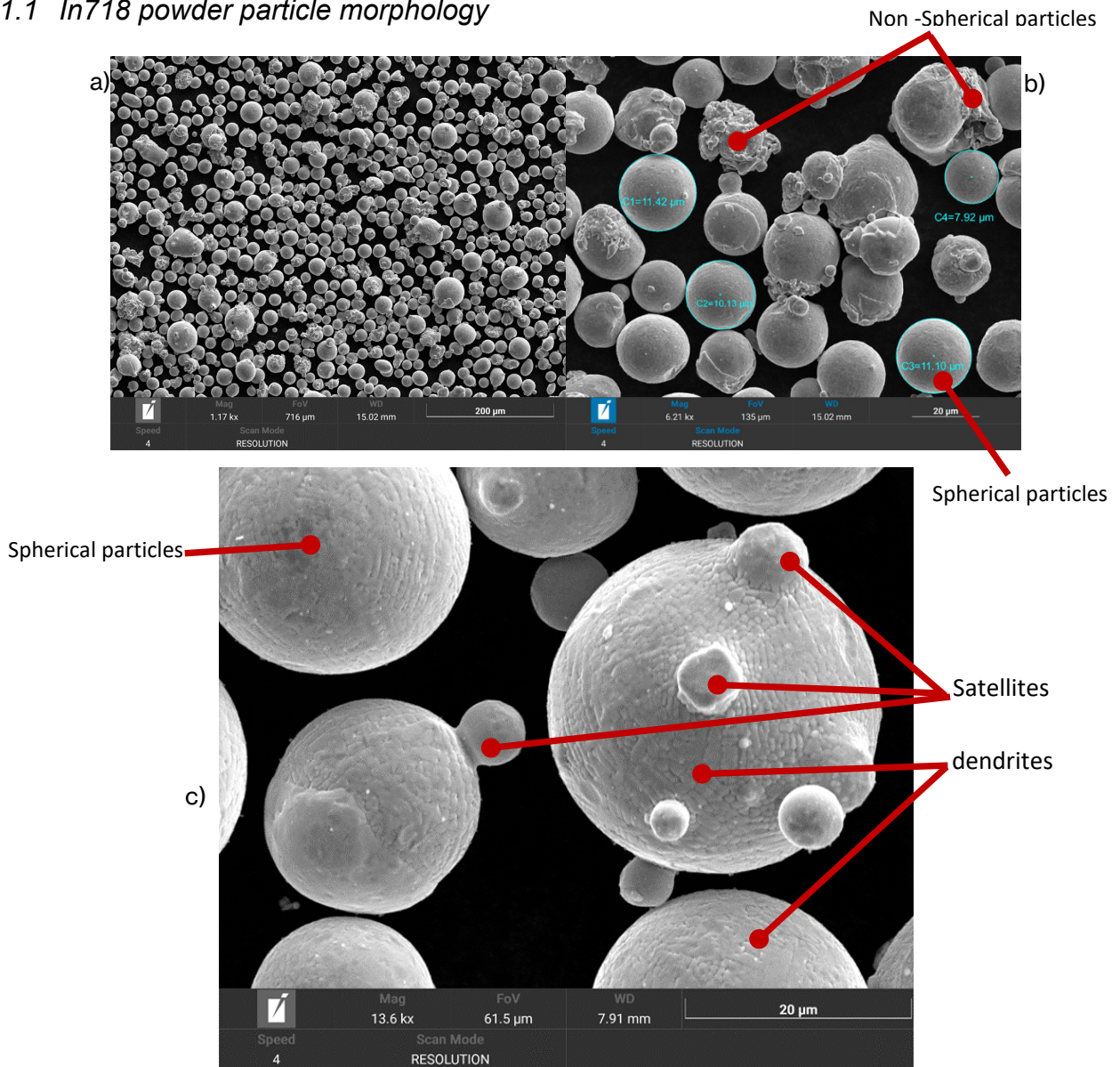


Figure 5-1: In718 powder SEM images (a - c) virgin (c) high magnification showing dendritic features

In718 powder particles produced by gas atomization method as shown in figure 5-1(a - c) shows the morphology such as satellite shape, spherical shape, non spherical shape and dendrites while figure 5-1(b) In718 powder particles circumference measured range between 7 -12 μm.

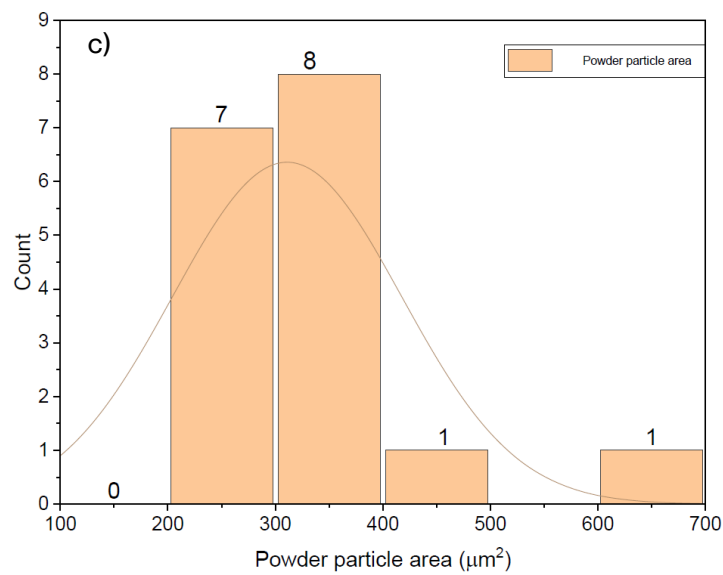
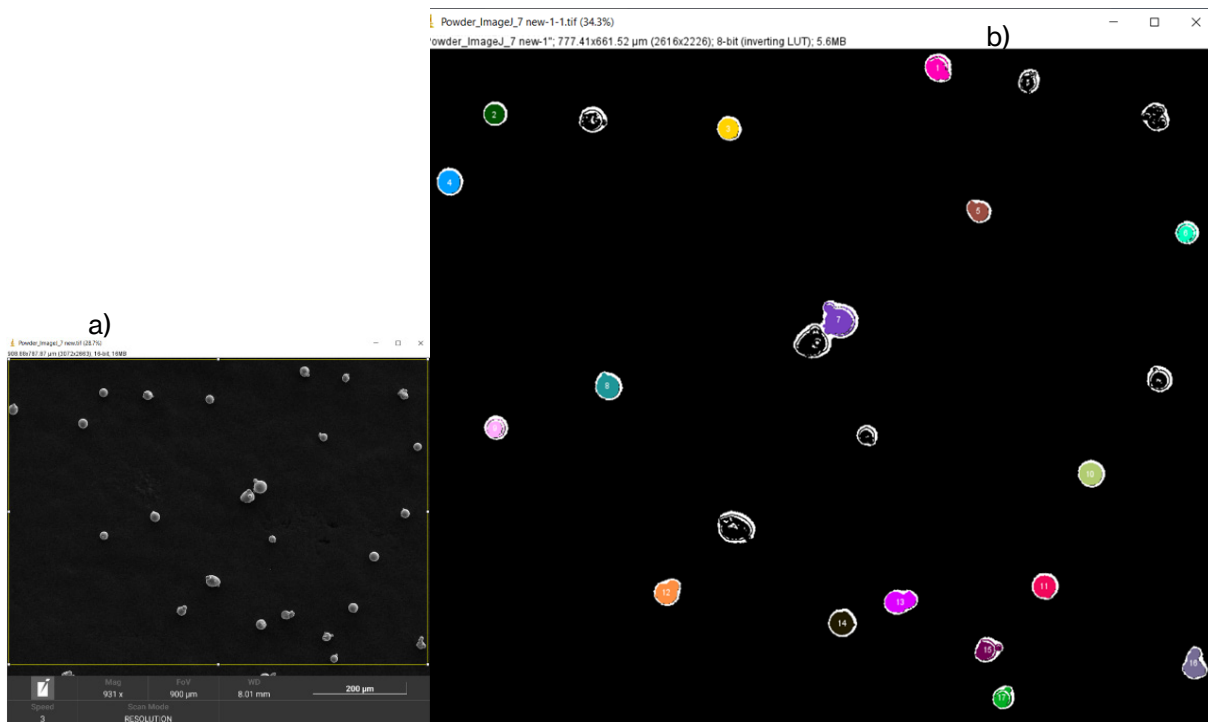


Figure 5-2: (a & b) Image J sample analysis (c)PSD

Image J software (refer Figure 5-2 a & b) is used to characterize the IN 781 powder particles sizes and morphologies. Then, the data of powder diameters were inserted into excel and by Origin pro enabled to draw the particle distribution(PSD). It is found that most of the particles are spherical means that the In718 powder particles used in our work is of virgin state and the diameter range from 20-50 μm. Some particles have non spherical shapes due to the defect of gas atomization process of this powder particles.

Figure 5-3, summarizes the importance of powder particle sizes in order to obtain the required mechanical properties in this case tensile strength is improved with grain sizes of 25-50 μm during LPBF.

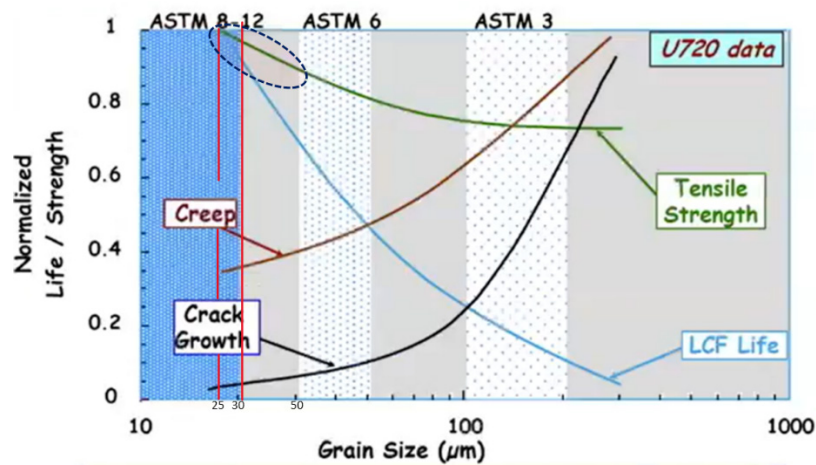


Figure 5-3: Normalized life and strength versus grain size [64]

The data in table 5-1, was provided by Sophia high tech s.r.l are comparable to the SEM image and image J characterization results of In718 powder PSD as reported in Figure 5-2. $D_v(10)$, $D_v(50)$ and $D_v(90)$ is the mean the particle sizes at 10% vol, 50% vol, and 90% vol, of samples respectively [7]. Laser size diffraction characterized the In718 particles in a range of 21.7 – 57.8 μm as reported in table 5-1.

Table 5-1: In718 powder sizes

SIEVE ANALYSIS - ASTM B214					
	Units	Min	Max	Result	Approved
+63 μm	weight %	0	0	0	Pass
+53 μm	weight %	0	1	0	Pass
+45 μm	weight %	Info Only	-	5.18	Pass

LASER SIZE DIFFRACTION - ASTM B822					
	Units	Min	Max	Result	Approved
$D_v(10)$	μm	Info Only	-	21.7	Pass
$D_v(90)$	μm	Info Only	-	57.8	Pass
$D_v(50)$	μm	Info Only	-	35.9	Pass
-5 μm	volume %	0	0	0	Pass
-15 μm	volume %	0	10	1	Pass

HALL FLOW - ASTM B213					
	Units	Min	Max	Result	Approved
FR_H	s/50g	Flow	-	14	Pass

APPARENT DENSITY - ASTM B212					
	Units	Min	Max	Result	Approved
Bulk Density	g/cm^3	Info Only	-	4.12	Pass

5.2 Tensile test results

5.2.1 Stress-strain curves of Inconel 718 superalloys:

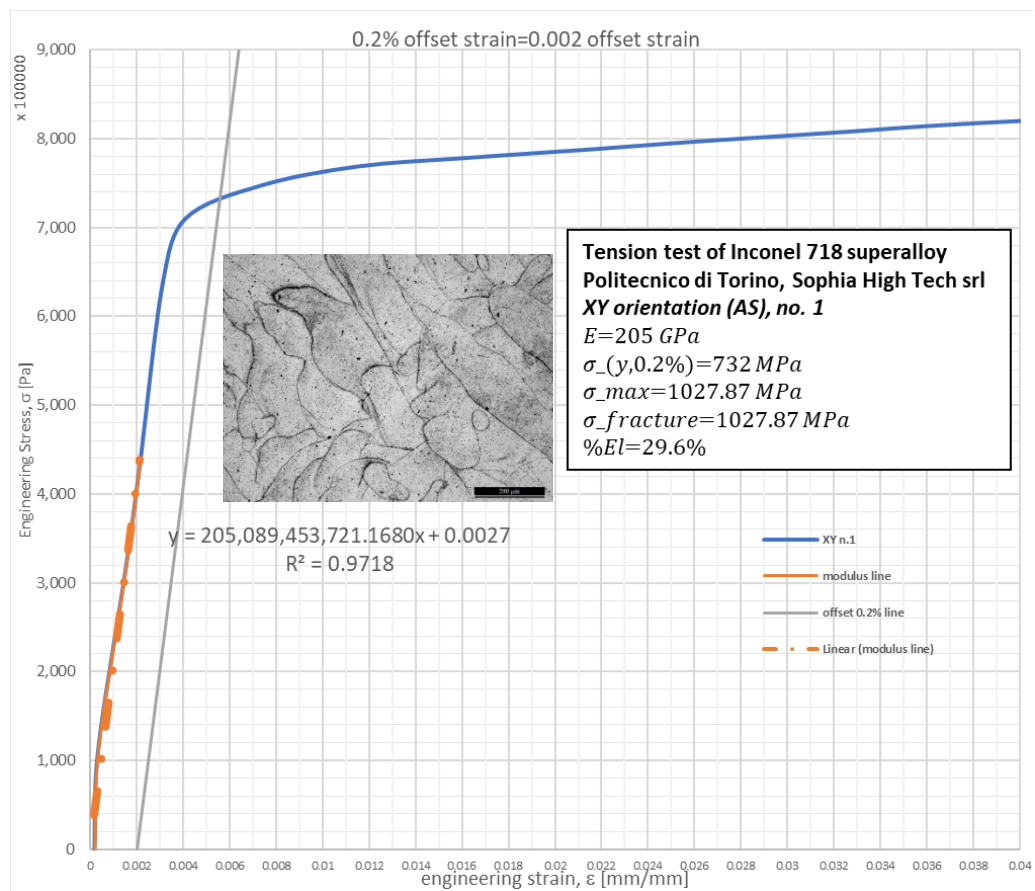


Figure 5-4: XY AS n.1

Figure 5-4 shows engineering strain versus engineering stress of **AS no. 1 in XY** plane orientation with $R_{p0.2}$, E , and UTS of 732 MPa , 205 GPa and 1027.87 MPa respectively. E_l is nearly 30% hence it has some properties of ductility. Island scan strategy has improved the UTS due to columnar dendrites (refer figure 5-18) as single crystals and no transverse crystals.

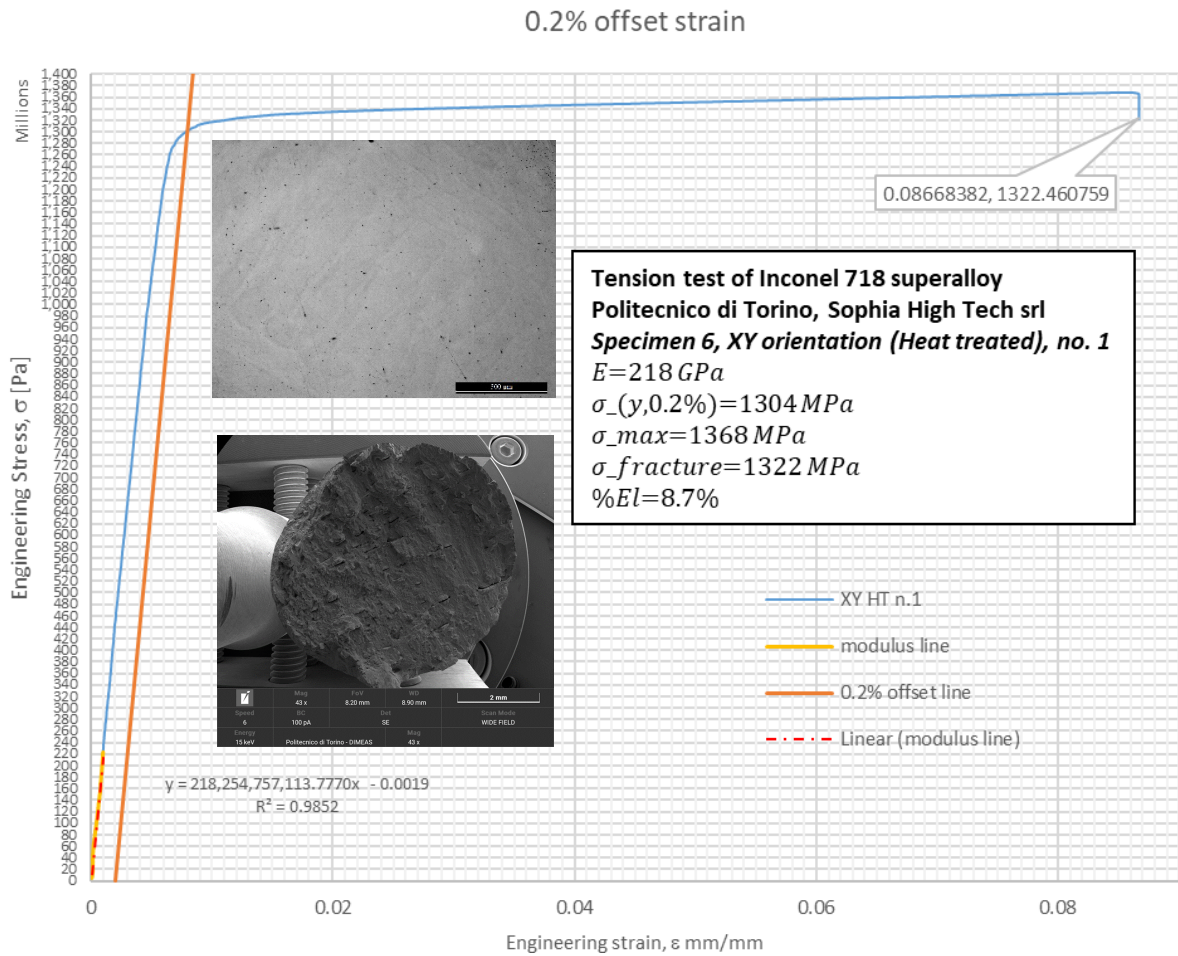


Figure 5-5: Specimen 6, XY HT n.1

Figure 5-5, shows engineering strain vs engineering stress of **specimen 6, HT no. 1 in XY** plane orientation with σ_y , E , and UTS of 1304 MPa , 218 GPa and 1368 MPa respectively. E_l is slightly 9 % hence it has some properties of brittleness, and its fracture surface is smooth. HT has improved the E , σ_y and UTS when compared to AS XY sample. But E_l has been affected by reduction of nearly 21% from AS XY. This can be due to recrystallization of grains during HT.

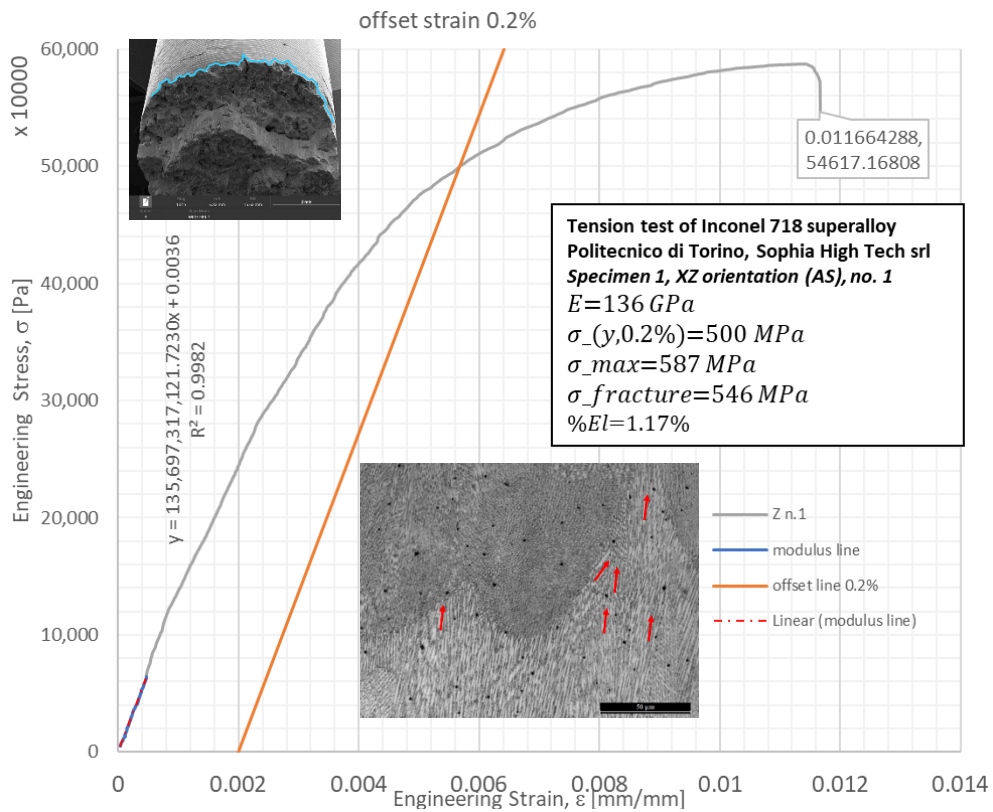


Figure 5-6: Specimen 1, ZX AS n.1

Figure 5-6, shows engineering strain vs engineering stress of **specimen 1, AS n.1 in ZX** plane orientation with σ_y , E , and UTS of 500 MPa , 136 GPa and 587 MPa respectively. E_l is slightly 1.2 % hence it has properties of brittleness. Melt pools, elongated columnar dendrites, porosities and key holes are seen on its microstructure. These are some of the reasons of anisotropy between ZX_AS and XY_AS.

5.2.2 Stress- strain trend for all samples of Inconel 718 superalloys

Figure 5-7 shows anisotropies In718 cylindrical rods in ZX and XY orientations for HT and AS configurations. Specimen 1 and specimen 2 have lower E_l compared to XY no. 1 and XY no. 2. While specimen 6, specimen 7 and XY HT no. 3 have higher modulus, yield strength, UTS but with low ductility. Table 5-2 summarizes tensile anisotropies properties of In718 of Figure 5-7.

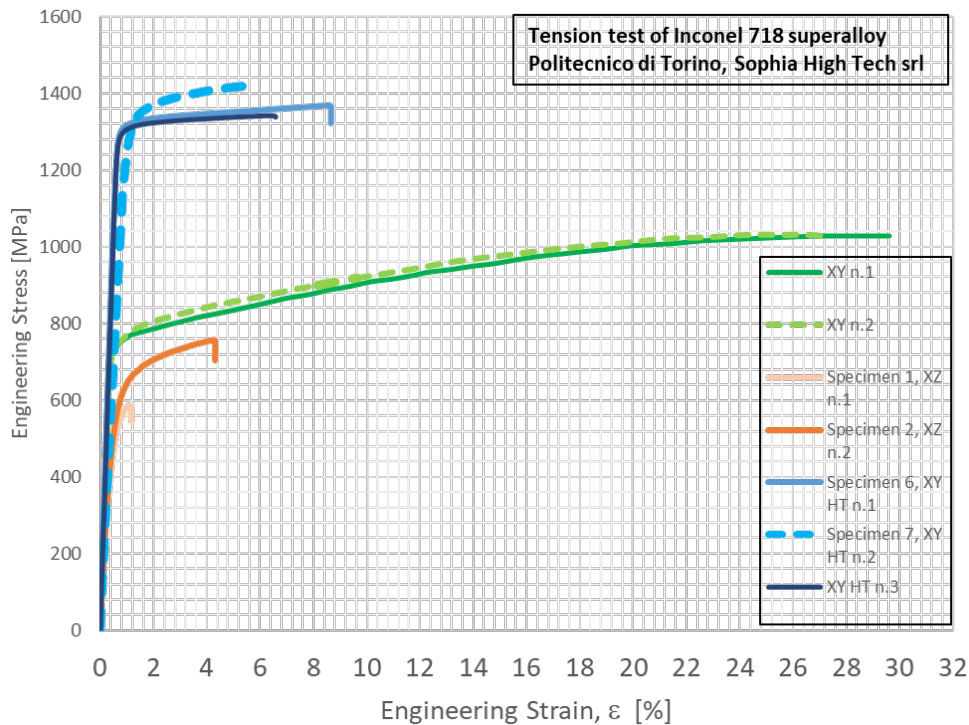


Figure 5-7: Engineering Stress - strain anisotropies for all samples of In718 superalloys

5.2.3 Summary of tensile anistropies of Inconel 718 samples

Table 5-2: Tensile anisotropies properties of Inconel 718 samples

Specimens	Orientation	Tensile anisotropies parameters				
		E [GPa]	σ_y [MPa]	UTS [MPa]	Sigma R [MPa]	Elongation To Fracture [%]
	XY AS n.1	205	732	1027.87	1027.87	29
	XY AS n.2	224	730	1030	1033	27
Specimen 1	ZX AS n.1	136	500	587.175605	546	1.17
Specimen 2	ZX AS n.2	135	561	756	750	4.3
Specimen 6	XY HT n.1	218	1304	1368	1322	8.7
Specimen 7	XY HT n.2	212	1303	1417	1417	5.5
	XY HT n.3	206	1295	1342	1342	6.5

5.3 Optical micrography for microstructure analysis

5.3.1 Sample A2.1: AS

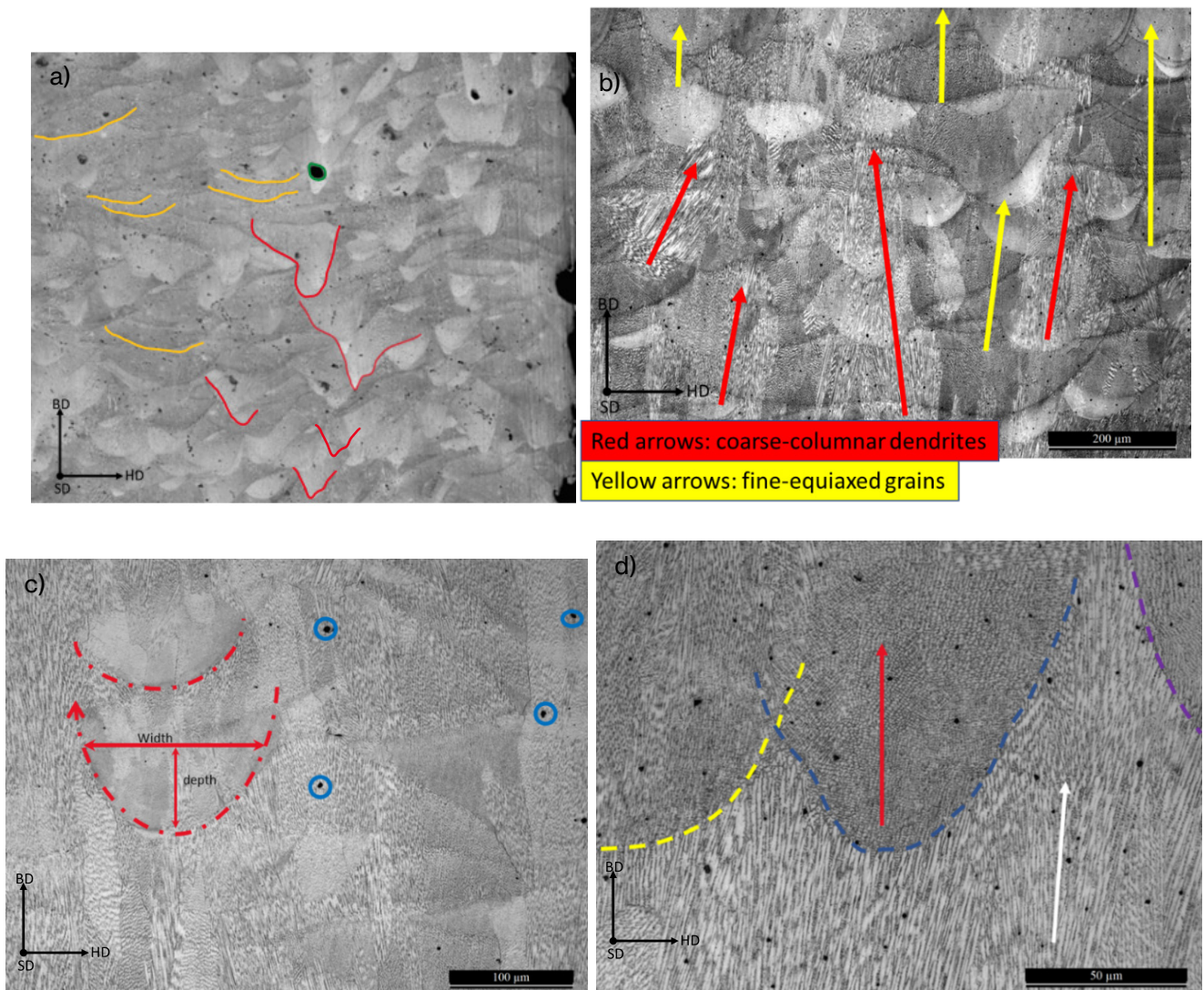


Figure 5-8: Sample A2.1 AS showing (a) melt pools, porosities and keyhole (b) elongated columnar dendrites and equiaxed dendrites growth direction (c & d) melt pool sizes and porosities on elongated columnar dendrites and equiaxed dendrites

Figure 5-8 a, shows melt pools (yellow colour) with key holes (red colour) while in Figure 5-8 b, red arrows indicate the random growth of columnar dendrites through the melt pools. And Figure 5-8 c, blue circles show porosities in the elongated columnar grains and size of melt pool is shown in red colour. Figure 5-8 d, hidden lines indicating melt pool boundaries and red arrow shows the growing direction of equiaxed grains while white arrow shows growth of columnar dendrites. Random growth can be seen near the melt pool which is the cause of cracks.

5.3.2 Sample A2.2: HT

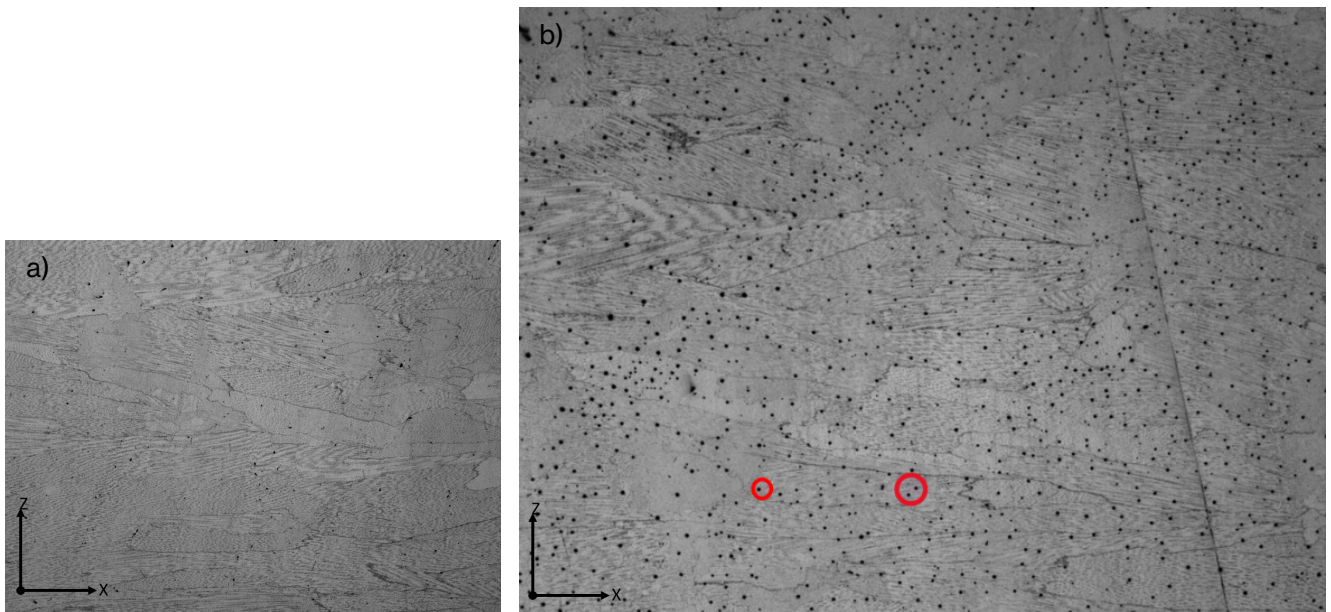


Figure 5-9: Sample A2.2 HT (a) elongated columnar dendrites grows randomly (b) porosities in red arrow

Figure 5-9 a, describes after heat treatment the columnar dendrites were homogenized and uniformly distributed. Figure 5-9 b, can confirm the existence of porosities in In718 as the cause of the fracture and this microstructure has a large number of porosities.

5.3.3 Sample B2.1: AS

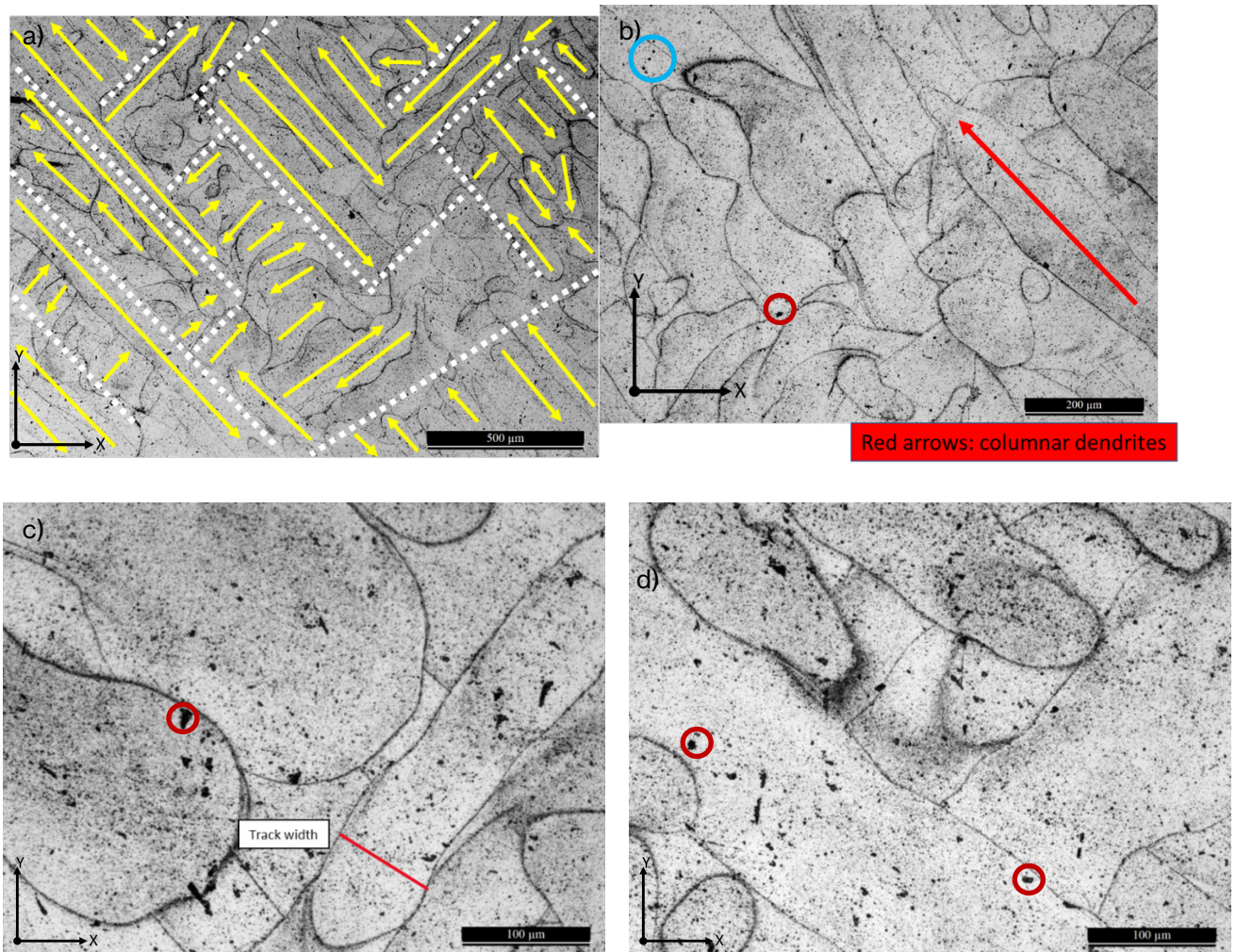


Figure 5-10: sample B2.1 showing (a) island scan strategy (b-d) direction of cellular dendrites

Figure 5-10 a, shows the random orientation of island scan strategy. Single crystals are observed. The dimension of each island is 5 mm x 5 mm. Also, can be seen that some columnar dendrites are longer than the others. Figure 5-10 b-d, shows direction of columnar dendrites is shown in red arrow, the track width, and porosities are spotted in blue circle while red circles represents keyholes.

5.3.4 Sample B2.2 HT

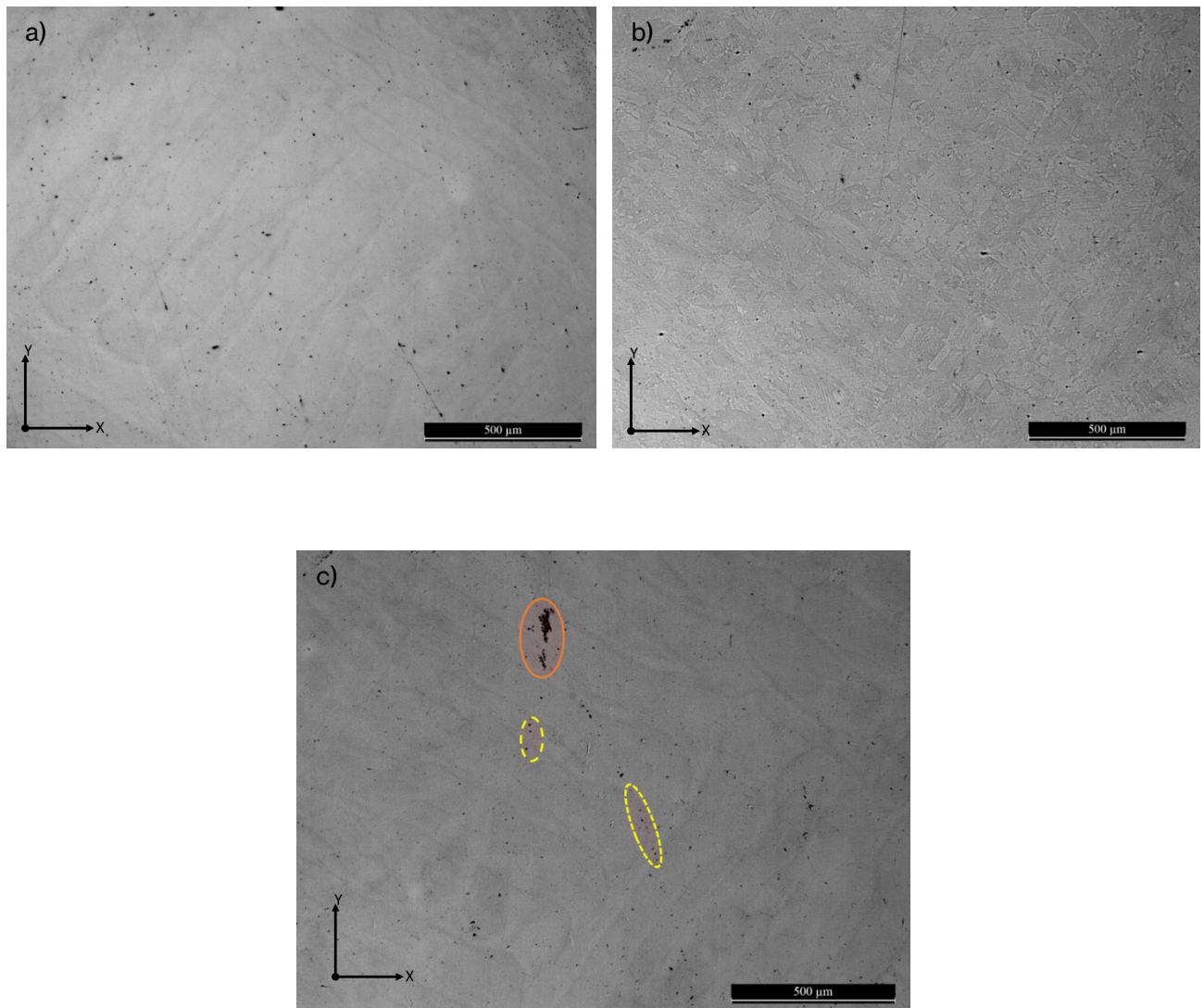


Figure 5-11: Sample B2.2 (a & c) island scan strategy and porosities (b) sample homogenization with porosities

Figure 5-11 a & c, still show island scan strategy, columnar and equiaxed dendrites are fused together and porosities are seen. While Figure 5-11 c, shows keyholes or etchant burnt with porosities around. The specimen microstructure is homogenized.

5.3.5 Microstructure anisotropies characterization

Table 5-3: Microstructure anisotropies

AM Process	Microstructure						
	Specimens	Orientation	Post process	Porosity [%] by MatLab	Grain morphology	Crystal texture	Residual stresses
LPBF	A 2.1	ZX	AS	0.53	Elongated columnar dendrites with porosities, keyholes, melt pools	-	-
	A2.2	ZX	HT	0.0083	Shortened columnar dendrites associated with low porosities, invisible melt pools	-	-
	B2.1	XY	AS	0.40	Elongated cellular dendrites and short culalar dendrites with porosities	-	-
	B2.2	XY	HT	0.41	Columnar dendrites seen as scan strategy with porosities, key holes	-	-

Table 5-3 summarizes the anisotropies sources such as porosities, elongated grain and melt pools that have been seen on the cube specimens in both perpendicular and parallel deposited build orientations which were characterized by OM and MATLAB code for porosities. The values of the porosities can confirm that there will be different measured values for parallel and perpendicular orientation due to the microstructure anisotropy property.

5.4 SEM Fracture surfaces analysis

5.4.1 Specimen 1: ZX orientation

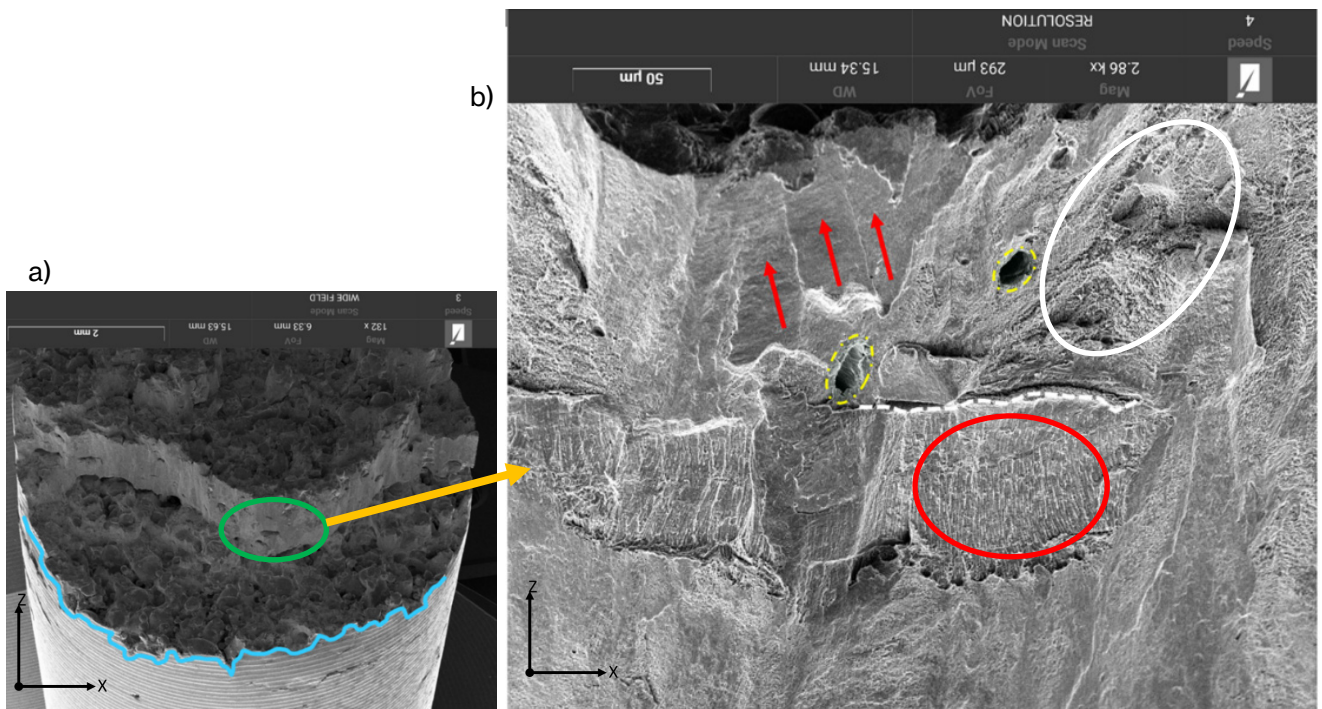


Figure 5-12: Specimen 1 showing (a) shear surfaces/facets (b) magnified facet showing the porosities, dimples, cleavages, elongated columnar dendrites

Figure 5-12 a, illustrates the shear surface or facet in green ellipse. Figure 5-12 b, a magnified facet can observe cleavage planes (in red arrows) towards the overload zone III, while red circle indicates the elongated columnar dendrites on the shear surface and dimples and lack of fusion (dashed yellow ellipses). A white ellipse indicates vertical intergranular and transgranular fracture. dashed white line shows vertical intergranular fracture at the boundary.

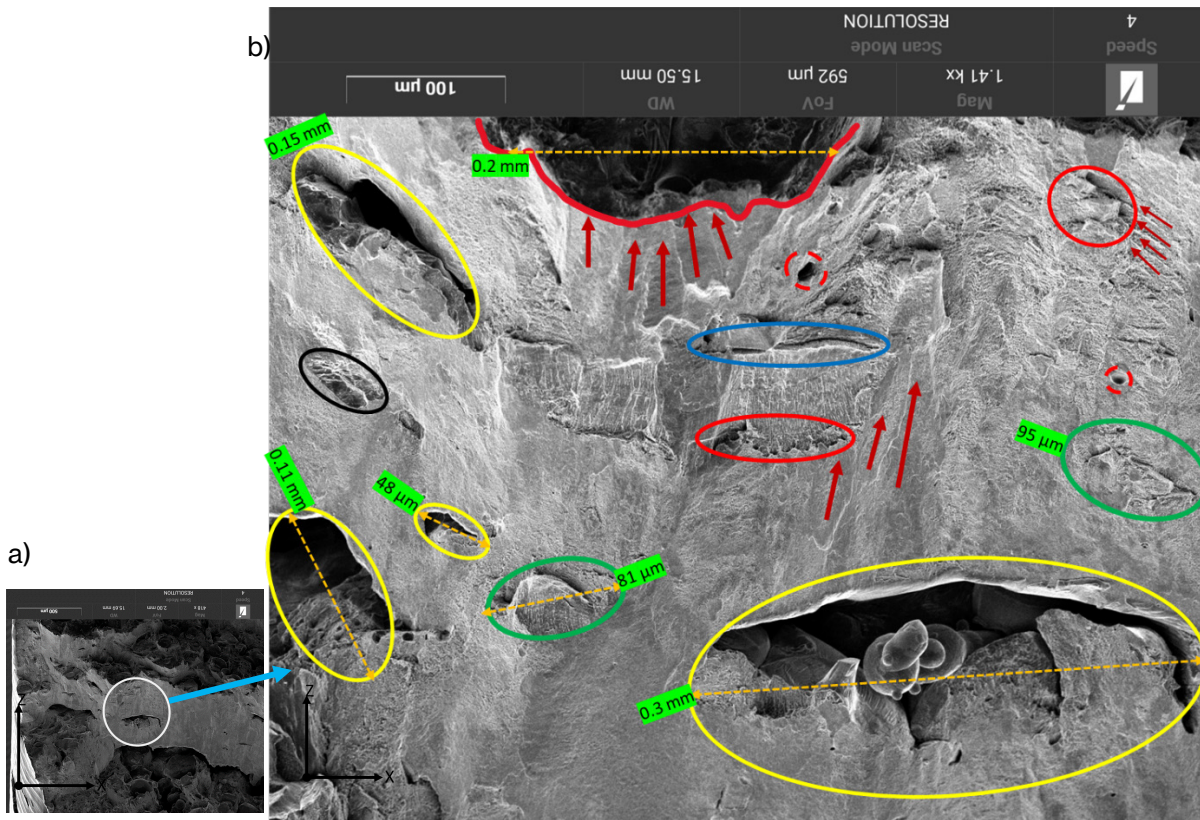


Figure 5-13: (a) shear surface (b) magnified shear surface

Figure 5-13 a, white circle represents portion of the stair or shear surface or facet and magnified into Figure 5-13 b. Cleavages (red arrows) prevail near the top of the shear surface (red curve, 0.2 mm) and vertical intergranular fractures (blue, red ellipses) where the separation by fracturing into zone III and grain boundaries is observed respectively. Brittle vertical transgranular fracture (black ellipse) and lack of fusion pores (yellow ellipses, with unmelted and partially melted powder particles) with dimensions of 48 μ m, 0.11mm, 0.15mm and 0.3 mm. Porosities are seen with dashed red circle.

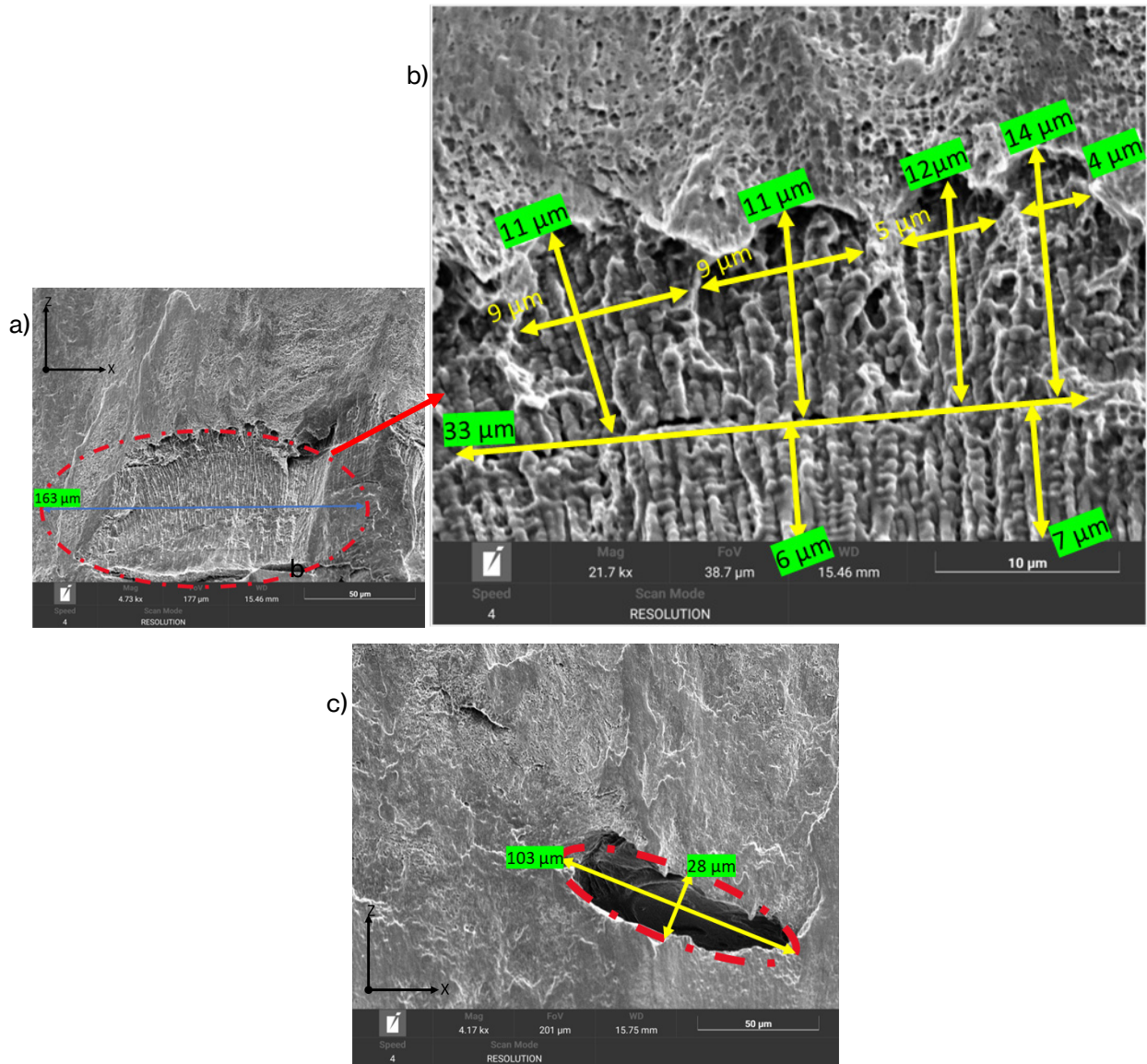


Figure 5-14: Shear surface

Figure 5-14, shows overall peeled columnar dendrites in a shear surface of 163 μm. In a magnified view Figure 5-14 b, there are four selected micro voids coalescence with a length range from 4- 9 μm and beneath there are elongated columnar dendrites with the heights that range from 11-14 μm. While Figure 5-14 c, shows lack of fusion pore with vertical transgranular fracture inside with a size of 103 μm x 28 μm.

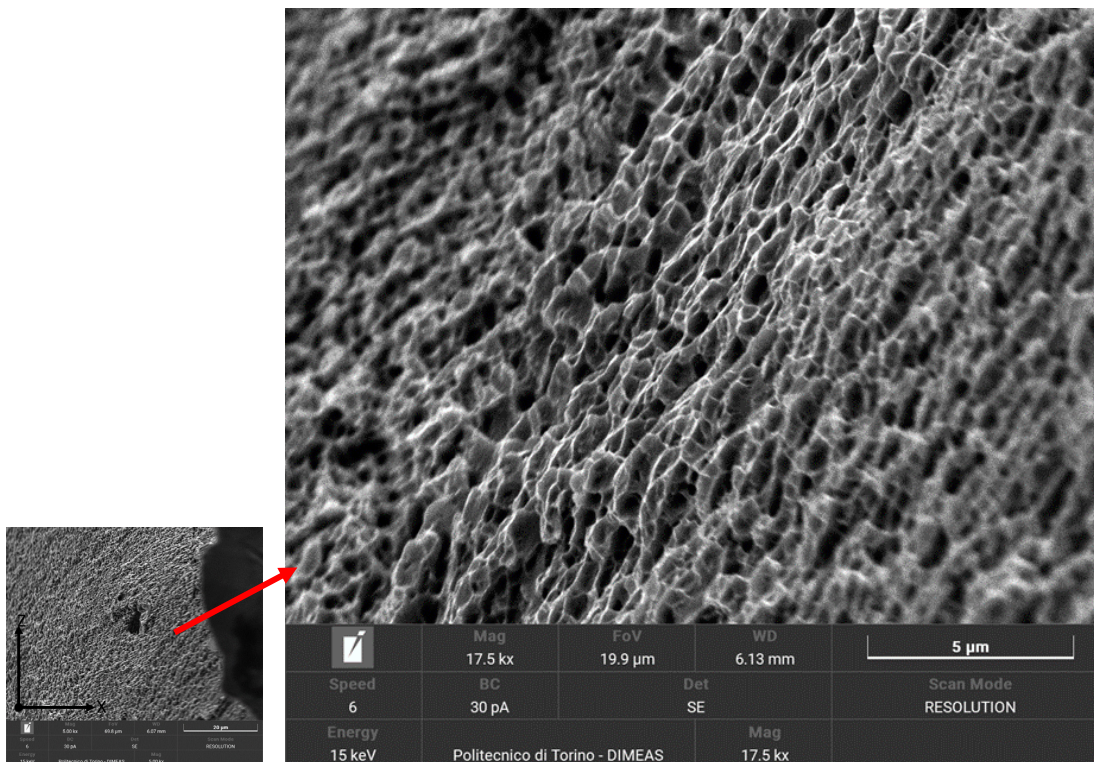


Figure 5-15: Ductile fracture

Figure 5-15 shows the magnified ductile fracture where micro voids are formed due to horizontal transgranular fracture.

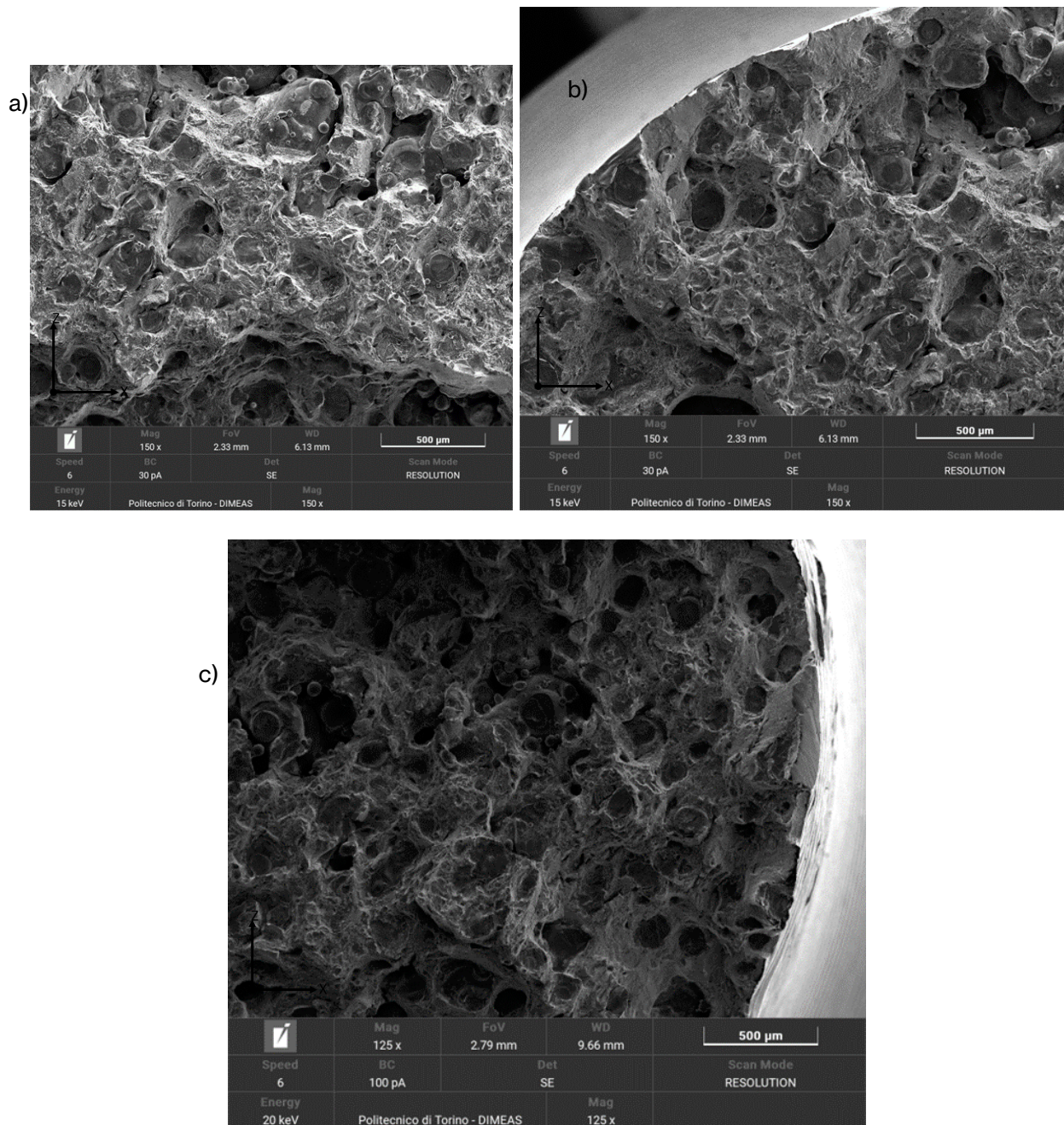


Figure 5-16: Vertical Intergranular fracture mixed with vertical transgranular fracture with cup and cone

Vertical transgranular fracture with cup and cone shape (represented by dark spots) in Figure 5-16 a-c. It means the fracture is passing through the grains. While around there are vertical intergranular fracture which is passing through the layers/ boundaries of the ZX plane. Also there are porosities (refer Figure 5-16 b) near the lateral surface with unmelted and partially melted powder particles.

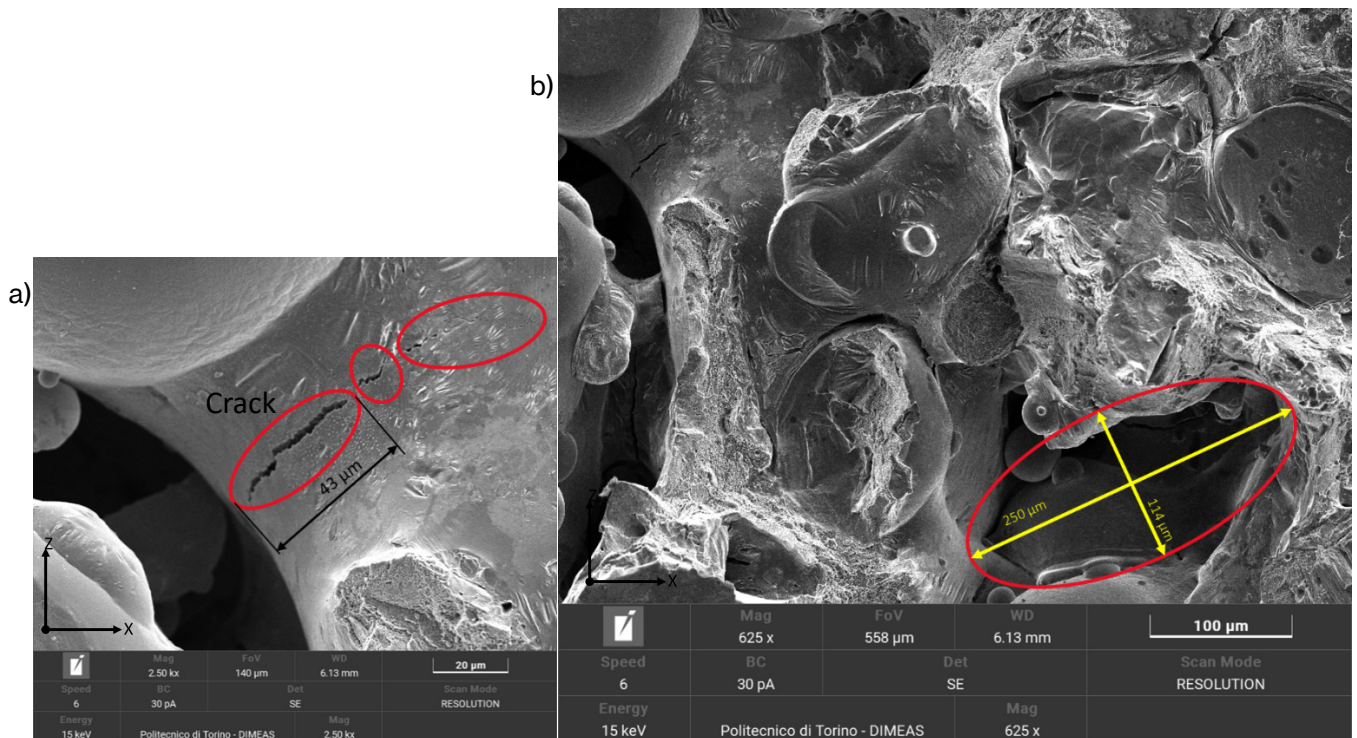


Figure 5-17: Ductile fracture mixed with brittle fracture

Figure 5-17 a, illustrates the lack of fusion surface has a crack with a length of 43 m and other smaller cracks. And Figure 5-17 b, lack of fusion pore of 250 x 114 μm has un-melted and partially melted powder particles. It surrounded with vertical intergranular and transgranular fracture.

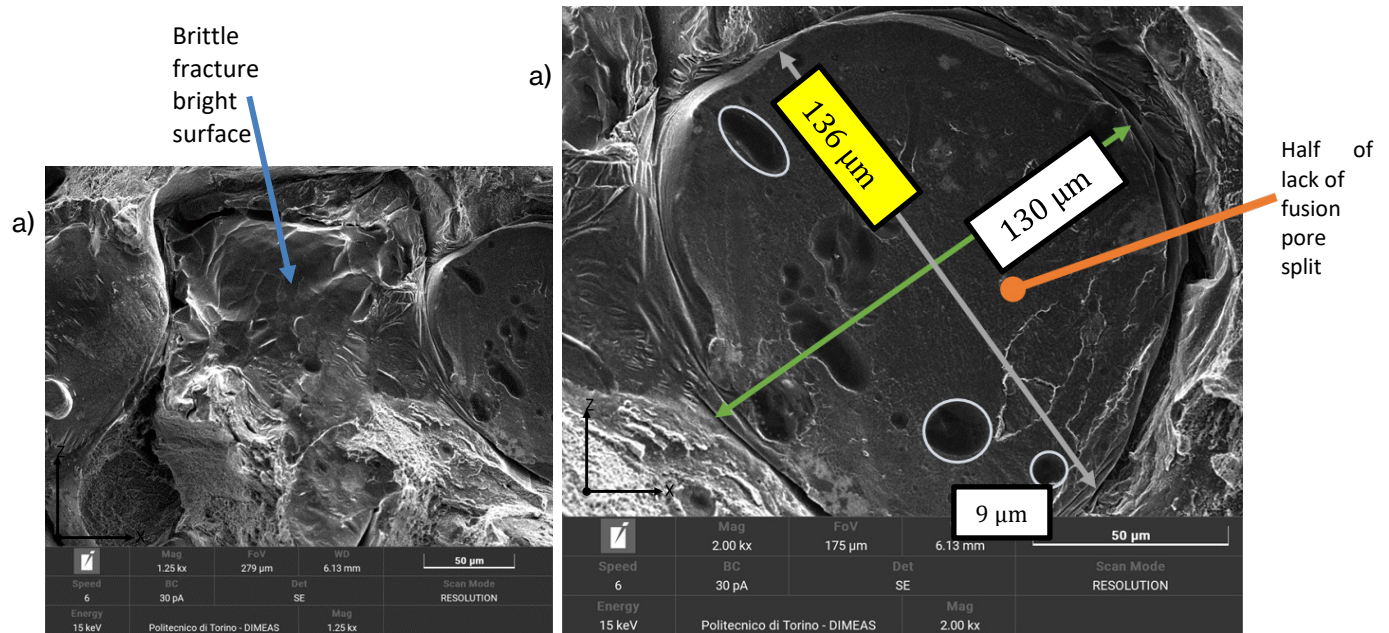


Figure 5-18: (a) Lack of fusion pore split and brittle fracture (b) Lack of fusion pore split

Figure 5-18 a) shows brittle fracture together with split lack of fusion pore. And Figure 5-18 b), magnified view describe the dimensions of the split lack of fusion pore size of 130 x 136 μm . And this is a very big pore that is responsible for the fracture of this specimen.

Fracture surfaces of In718 can be generally divided by appearance into four areas. The overall appearance of an In718 fracture surface AS (refer Figure 5-19) at different zones, with the initiation sites indicated by red arrows and a dashed circle.

In zone I, experience both cracks on the lateral surface and within has porosities filled with unmelted powder particles. In zone II, (width of 1.8 mm) reveals a **rough area outside the initiation site** as visible between red arrows and dashed yellow lines. It can be demonstrated that this region has lack of fusion pores distributed all over the area and has a shear surface (height of 0.33 mm). While in zone III (width of 3.1 mm) is particularly a wide fracture surface with visible large lack of fusion pores and are very deep down as a result causes the shear surface (height of 0.44 mm) towards the zone IV as can be seen between green solid line and dashed yellow line. The stairs/shear surfaces/facets have elongated columnar dendrites as in figure above 5-14. Now, it can be hypothesised that elongated columnar dendrites is where fracture will happen. At last the Zone IV is the final stage (width 0.6 mm) of the fracture where lack of fusion, dimples and rough surface are apparent due to overload.

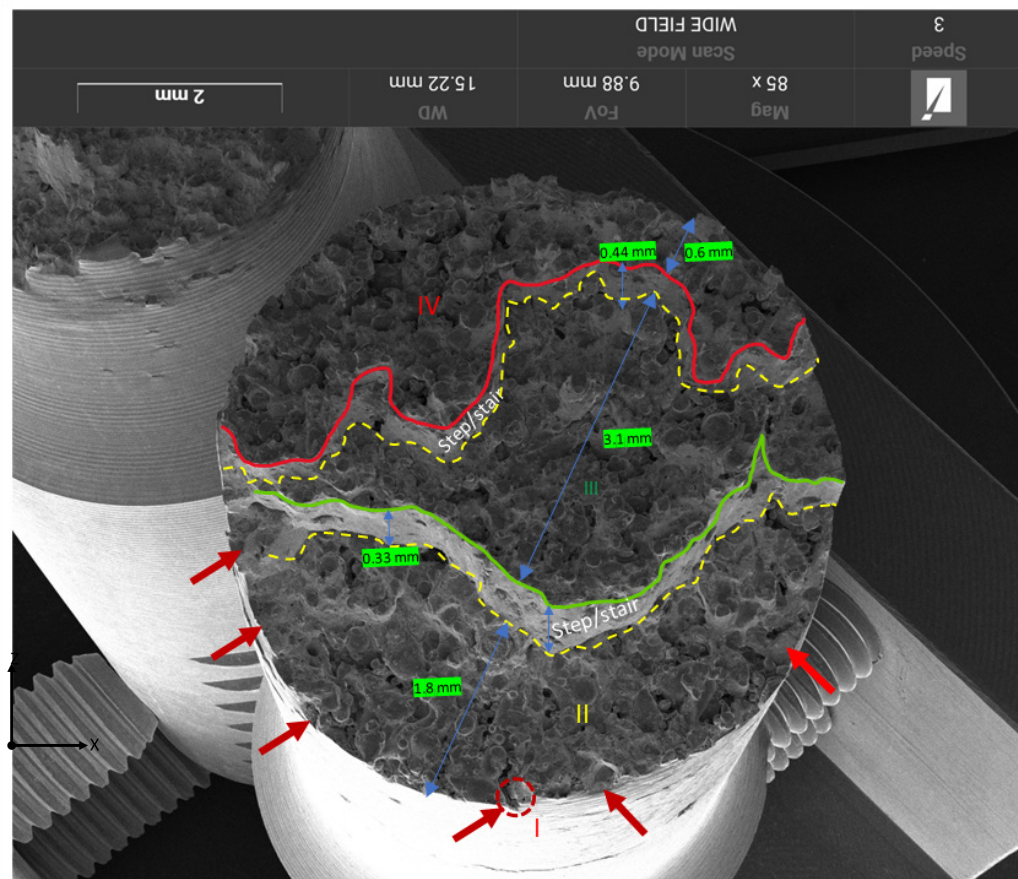


Figure 5-19: Four zones indicating the stages during crack initiation and propagation

5.4.2 Specimen 6: HT, XY orientation

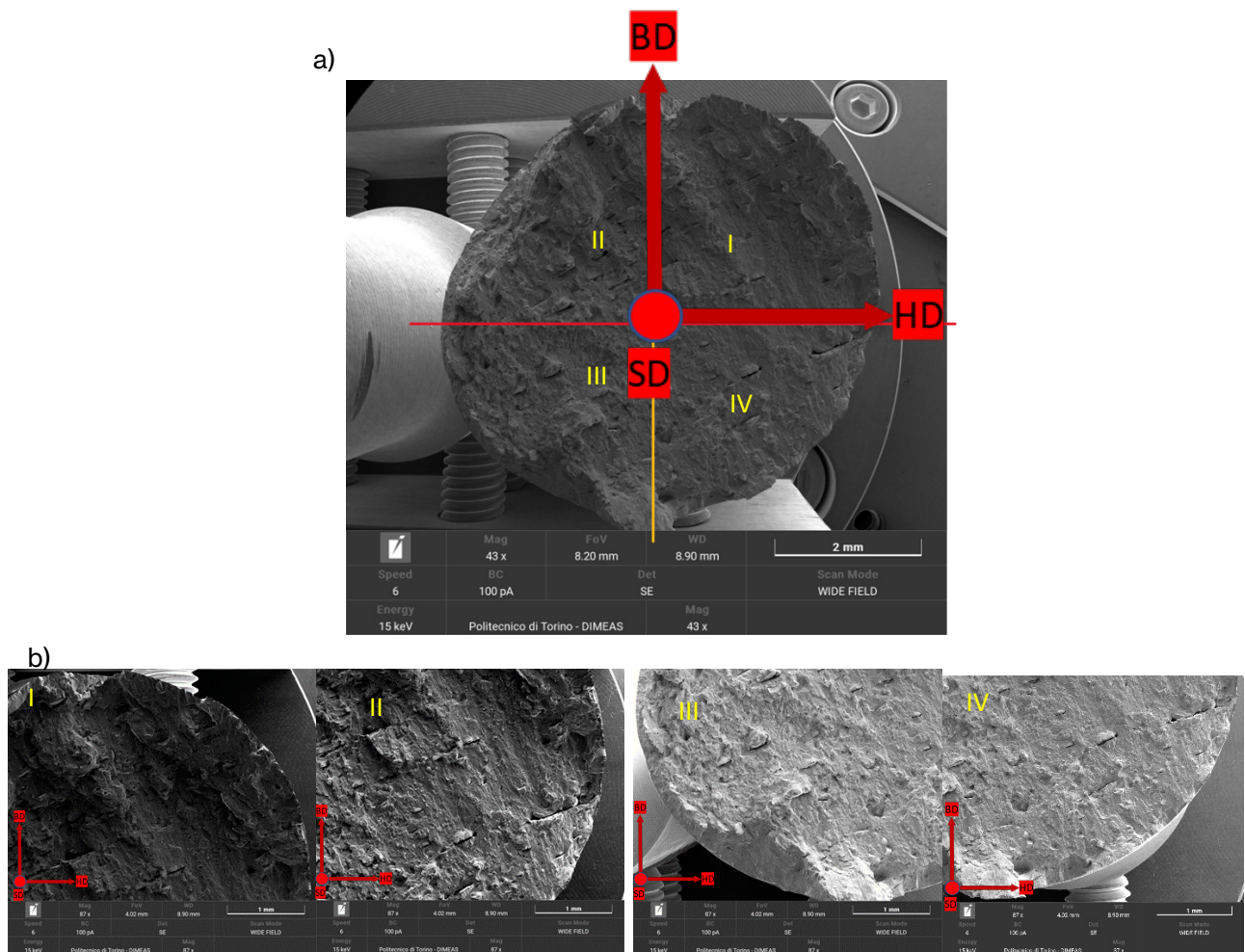


Figure 5-20: Specimen 6 shows (a) overall view showing a smooth flat surface, (b) ductile fracture and dimples (c) horizontal intergranular (d) horizontal transgranular

Figure 5-20 is divided into four quadrants I,II,III and IV.

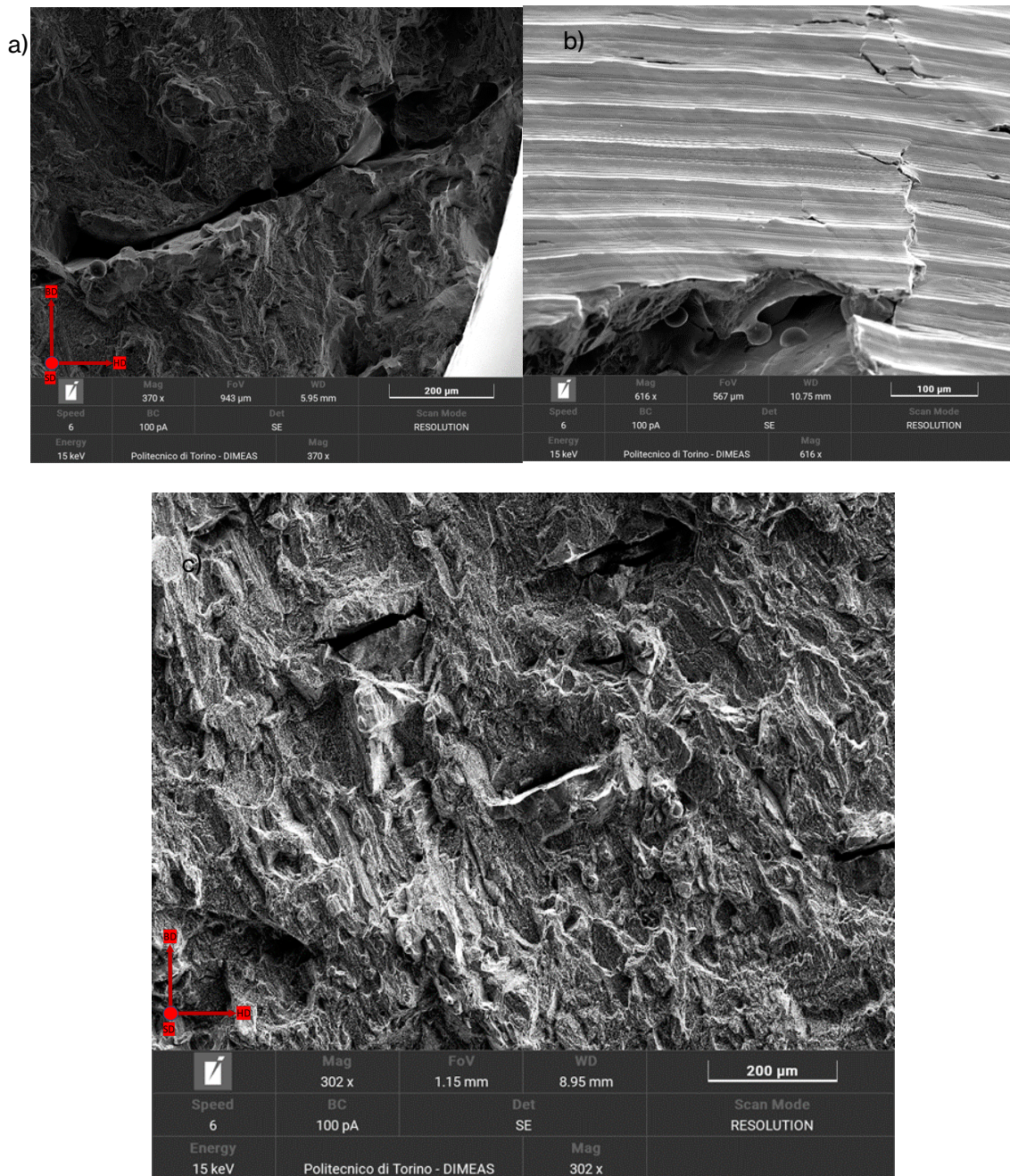


Figure 5-21: Specimen 6 shows (a) Horizontal intergranular fracture (b) lack of fusion pore near lateral surface (c) horizontal intergranular and quasi cleavage fracture

Figure 5-21 a, shows horizontal intergranular fracture where the fracture passes through grain or layer boundaries. While in Figure 5-21 b, lack of fusion pore is observed near the lateral surface of the specimen filled with partially or unmelted powders. And Figure 5-21 c, represent the horizontal intergranular fracture mixed with quasi cleavages surface fracture.

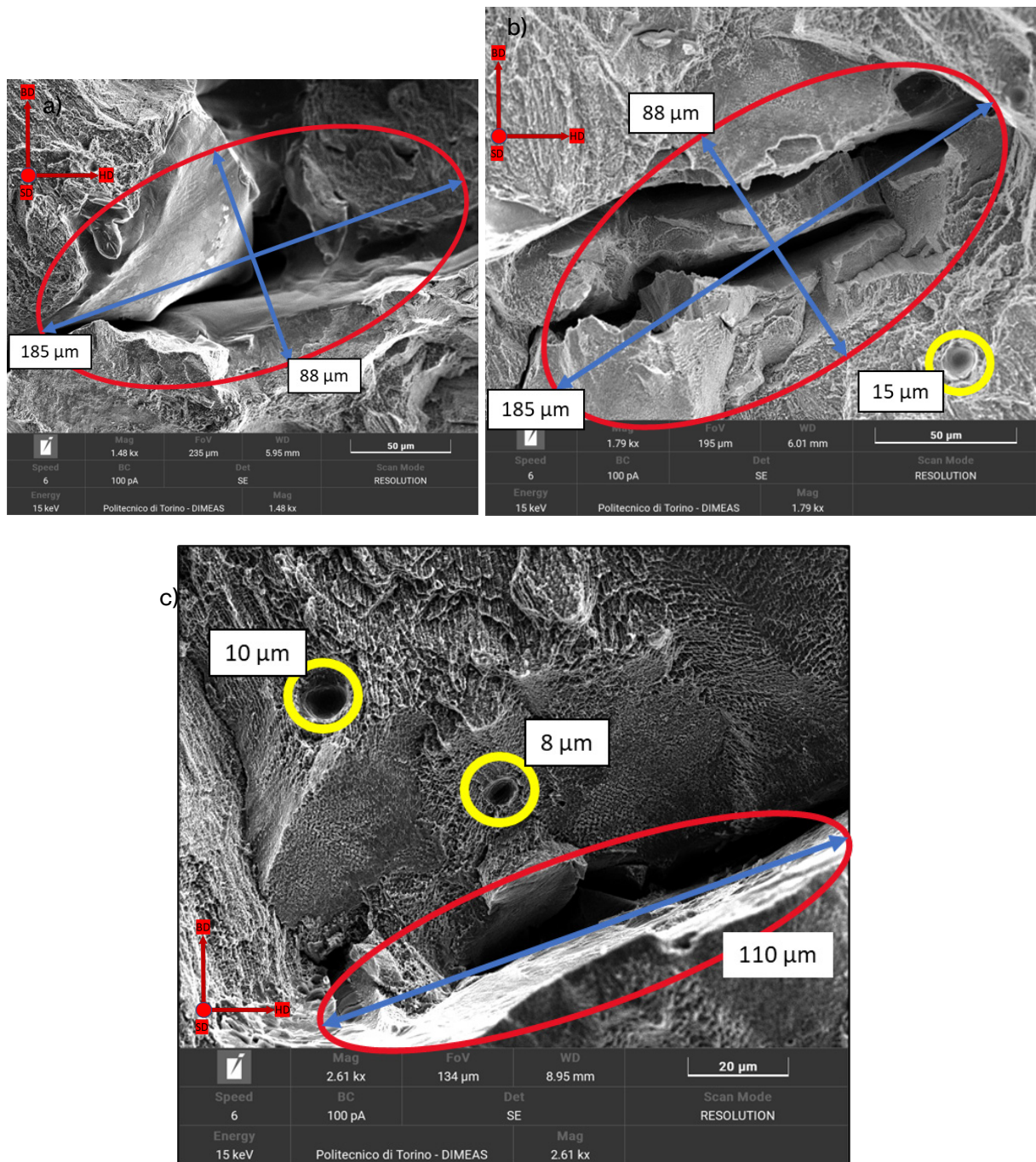


Figure 5-22: (a) T shape horizontal intergranular fracture (b) horizontal intergranular fracture (layer to layer split) (c) facets, dimples and horizontal intergranular fracture

Figure 5-22 a, red ellipse shows the T shape-horizontal Intergranular fractures equal to a length of 185 μm x 88 μm. In Figure 5-22 b & c, describe dimples (in yellow circles) have a diameter of 8 – 15 μm.

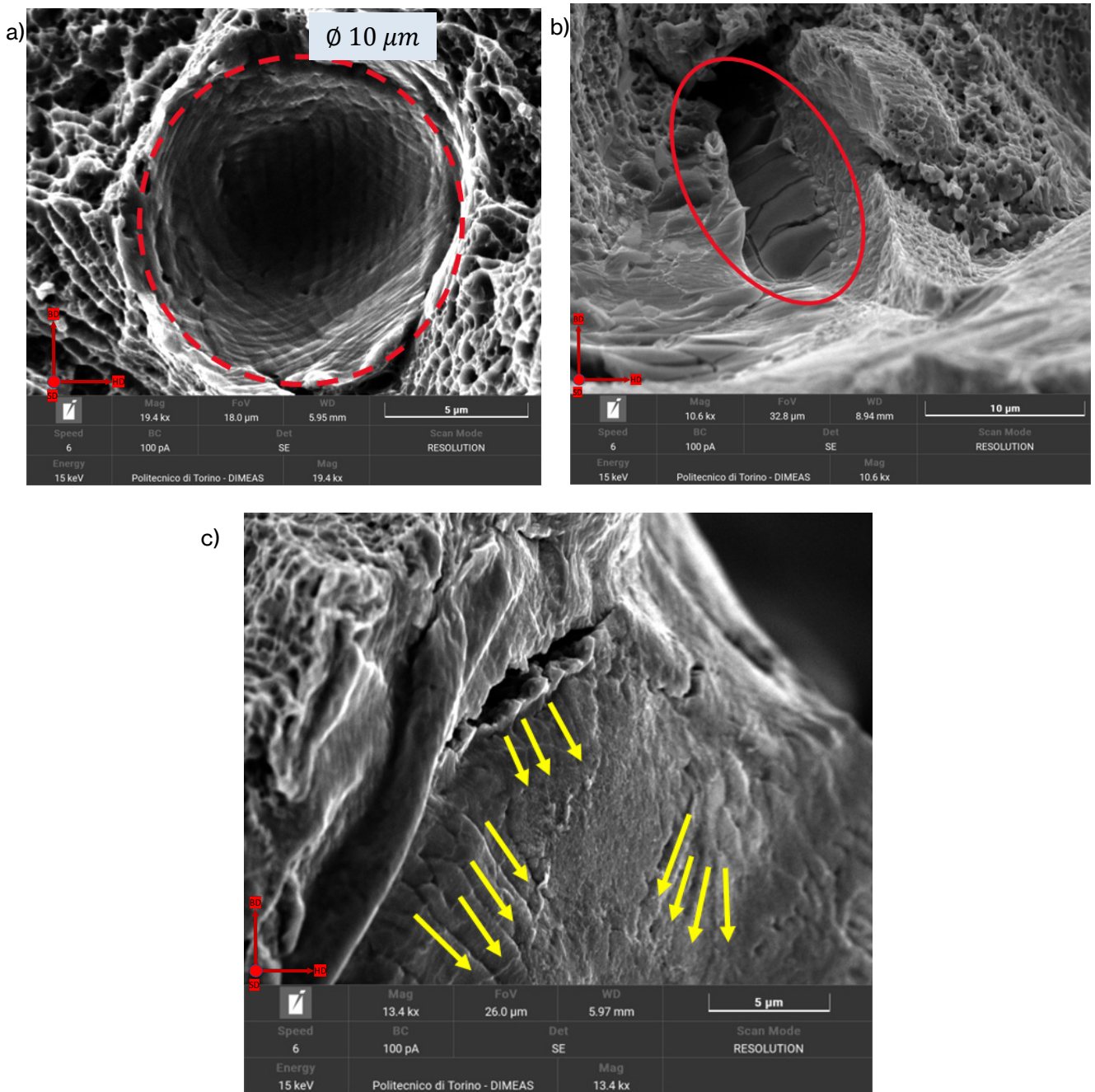


Figure 5-23:(a) pore ($\varnothing 10$) with horizontal transgranular fracture and micro voids coalescence (b) horizontal transgranular fracture inside lack of fusion pore, micro voids coalescence (C) intergranular mixed with cleavages fracture

In Figure 5-23 a, pore (dashed red circle) of a $\varnothing 10 \mu\text{m}$ with horizontal intergranular fracture on the inside and micro voids coalescence are outside around the pore. For Figure 5-23 b, transgranular fracture (red ellipse), micro voids coalescence and intergranular fracture. And Figure 5-23 c, indicates intergranular fracture, micro voids coalescence and cleavages (in yellow arrows).

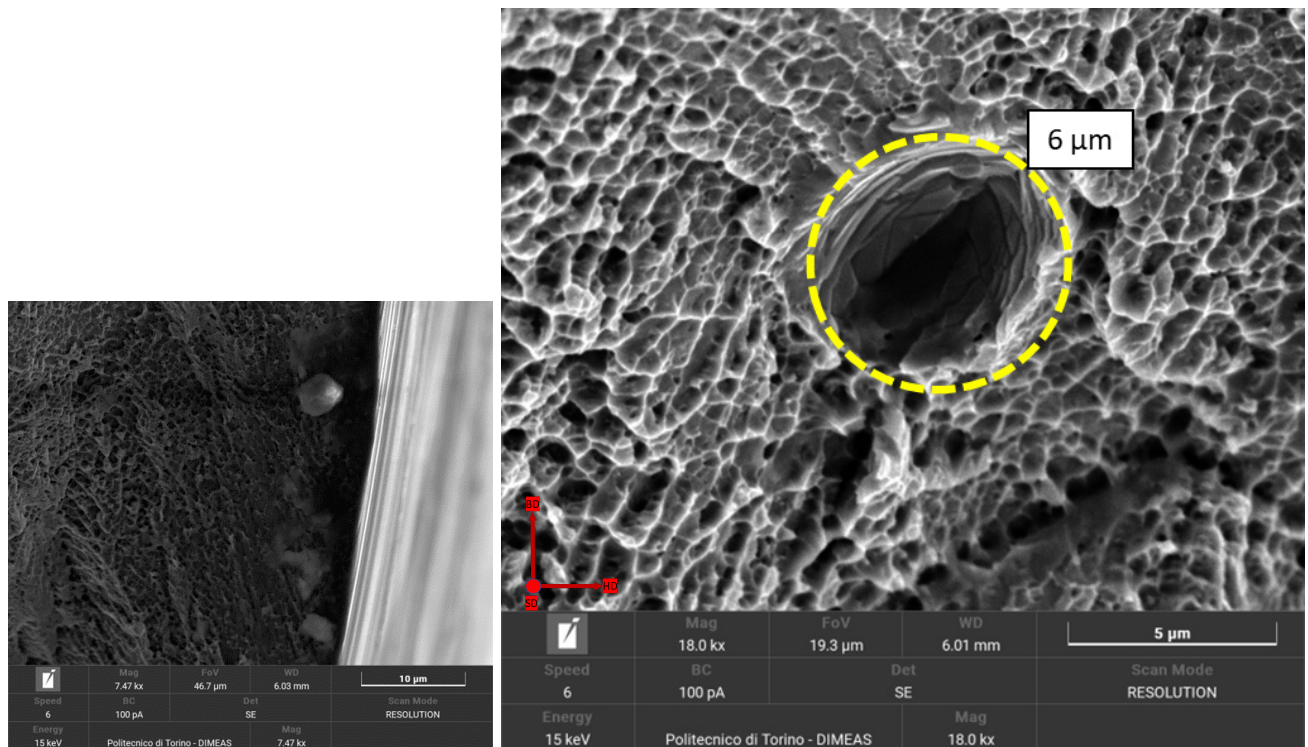


Figure 5-24: Lack of fusion pore with brittle intergranular fracture mixed with ductile fracture (micro voids coalescence)

Figure 5-24, illustrates a pore $\varnothing 6 \mu m$ inside revealing brittle intergranular fracture of dendrites. Ductile fracture due Micro voids coalescence (effects of elongated grains which causes anisotropies) is observed around the pore.

Specimen 7

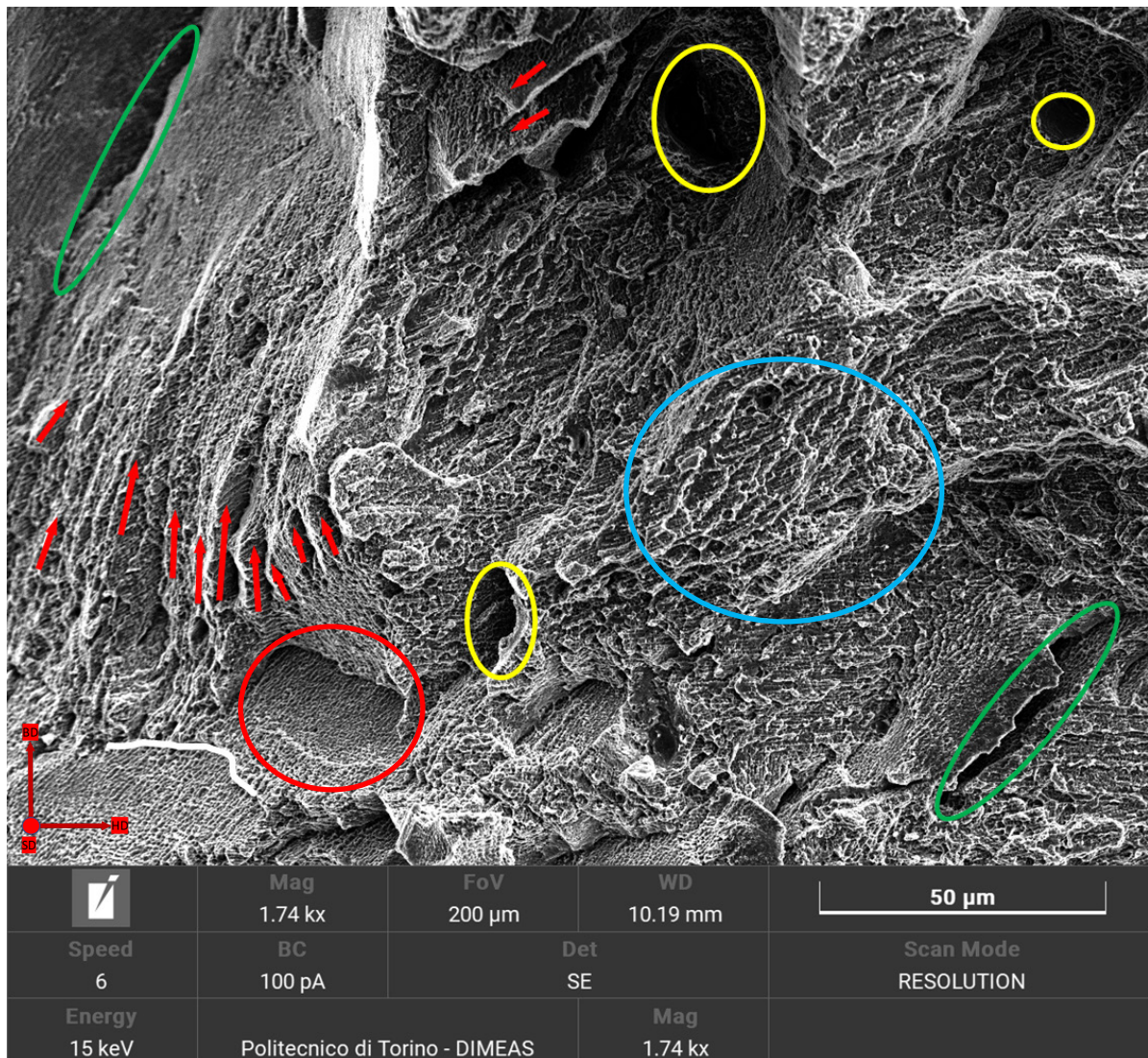


Figure 5-25: Brittle and ductile fracture mixed

Figure 5-25, describes the intergranular fracture (in green ellipse), cleavage rivers (in red arrows) and facets (red circles), dimples (yellow circles) and micro voids coalescence (blue circle)

5.4.3 External surface analysis

According to Kayak et al., [64] suggest that Transmission electron microscopy or atomic force microscopy can reveal the effect of the AM post-process and its ability to modify and enhance the microstructure by Finish machining (FM), drag finish (DF) and vibratory surface finish (VSF).

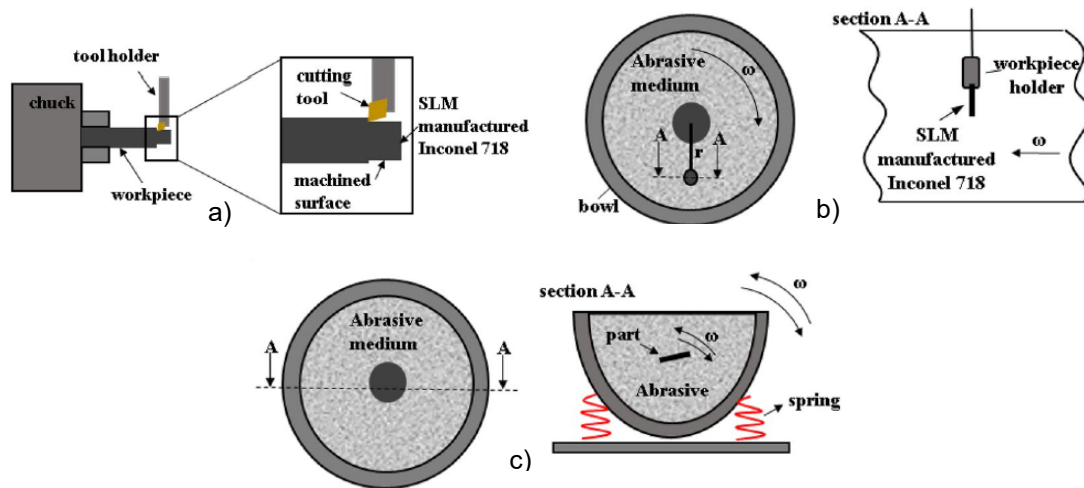


Figure 5-26: Surface enhancement operations (a) Finish machining (b) Drag finish (c) vibratory surface finish [65]

Therefore, according to Kayak et al., the following SEM images means that the cracks were not due to FM, DM and VSM. Consequently, tensile test is responsible to initiate these cracks due to the porosity, lack of fusion, partially and unmelted powder particles beneath the surface of cylindrical components.

More examination will be required to be able to characterize well these specimens surfaces before and after tensile testing. In this thesis only the analysis has been done after the tensile testing as shown below figures 5-27 to 5-29.

Specimen 1 (ZX orientaton)

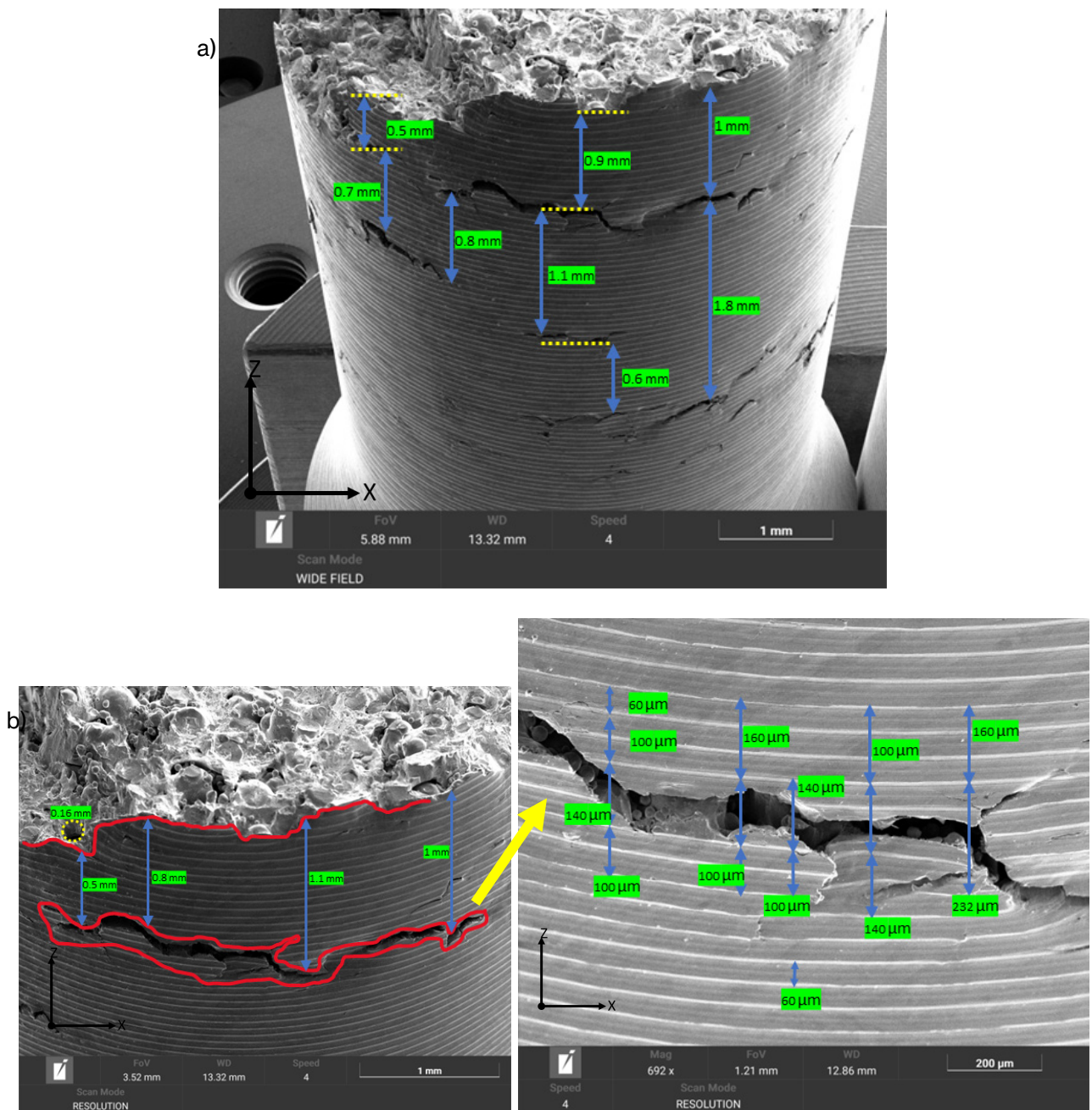


Figure 5-27: (a) Primary and secondary cracks (b) magnified primary crack magnification 692 x

In ZX crack are prevalent as shown in Figure 5-27, for example there are more than five primary cracks towards the secondary crack (where fracture ensued). Primary crack has a behaviour of specific height of 140 μm. Figure 5-27 b, dimples/lack of fusion pore of 0.16 mm are seen within the specimen and at a height of 0.5 mm from one of the primary crack. It means that perpendicular BD has many crack before failure than parallel BD. Also perpendicular layers (are like pages of a book) opening up because crack is parallel to the build direction. Layers are broken up easily.

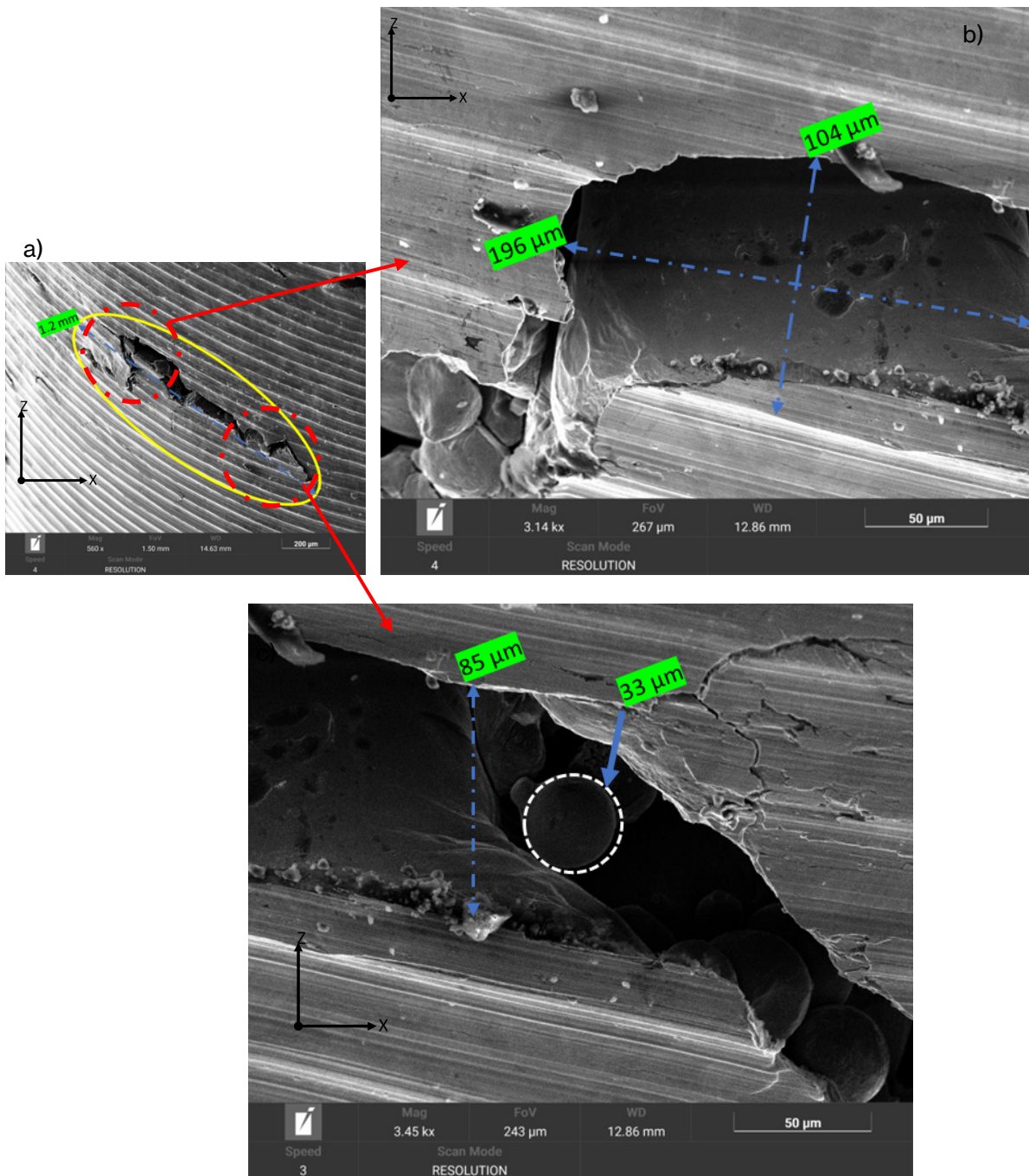


Figure 5-28: (a) primary crack (b & c) magnified views

Figure 5-28 a, illustrates the primary crack of 1.2 mm. In Figure 5-28 b, shows the magnified left hand side of the crack with dimensions of 104 μm x 196 μm which is a lack of fusion pore near the lateral surface of the specimen. And Figure 5-28 c, shows the right hand side of the crack with a height of 85 μm which is a lack of fusion filled with unmelted powder particle of $\varnothing 33 \mu\text{m}$.

Specimen 6 (XY build orientation)

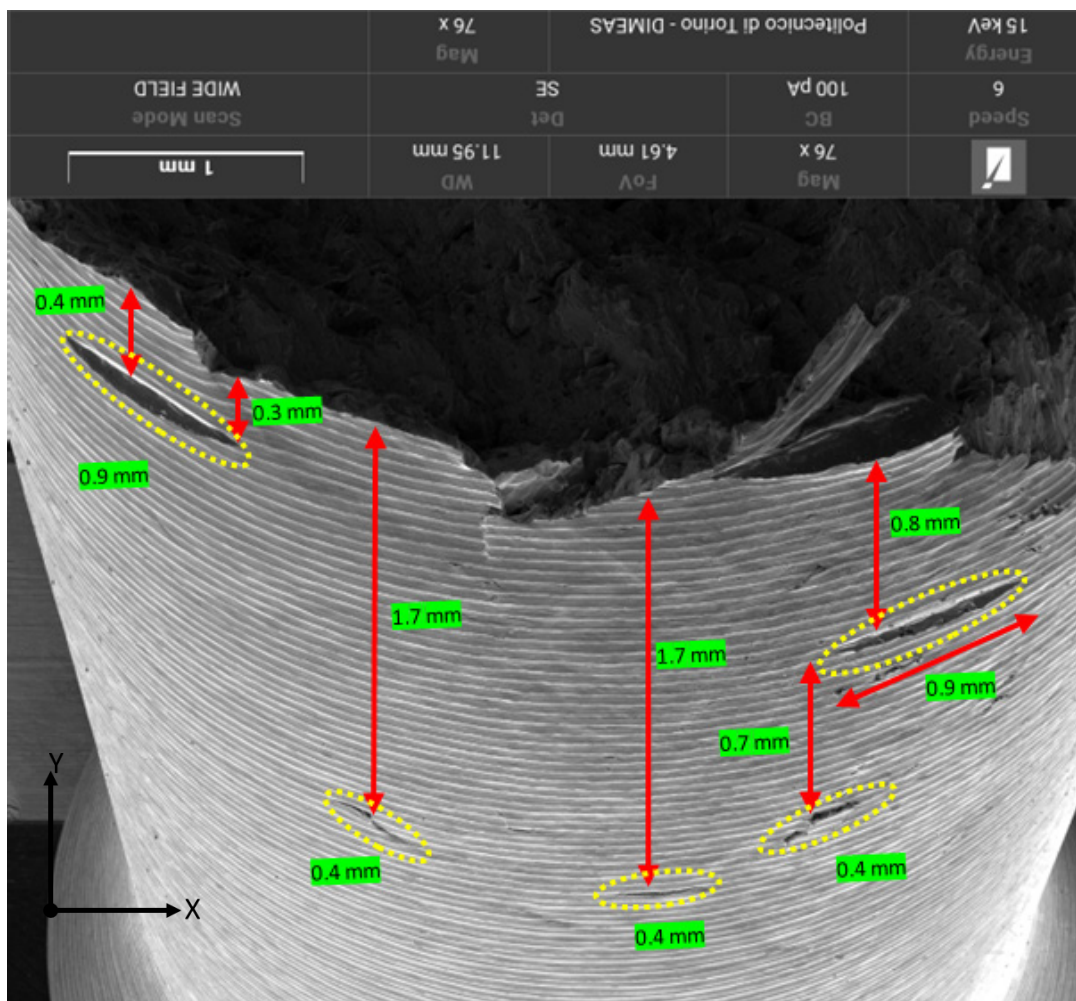


Figure 5-29: specimen 6 display lateral surface crack in XY orientation

Also, layers of XY build orientation breaking up because crack is perpendicular to the build direction. It is very difficult to break layers in XY orientation and can be observed that there are less cracks compared to ZX. Primary cracks sizes are 0.4 mm in length and 1.7 mm from the secondary crack. Again, it can be hypothesised that primary cracks sizes of 0.9 mm in length and 0.3-0.8 mm from the secondary crack is where initiation crack originated because they are bigger than the other cracks.

Hence, parallel BD has low number of cracks before failure than parallel BD. Also parallel layers cracks propagate perpendicular to the build direction. Layers are difficult to break.

5.4.4 Tensile anisotropies characterization

Table 5-4: In-situ tensile test results

		Tensile test results					
Specimen	Orientation	Post process	Modulus of elasticity (GPa)	Yield strength (MPa)	Ultimate tensile strength (MPa)	Elongation (%)	Fracture surface
Specimen 1	ZX	AS	136	500	587.175605	1.17	Elongated columnar dendrites dendrites, melt pools, lack of fusion, porosities
Specimen 2			135	561	756	4.3	
Specimen 6	XY	HT	218	1304	1368	8.7	Elongated columnar dendrites grains, melt pools, lack of fusion, porosities
Specimen 7			212	1303	1417	5.5	

*Elongation values are highly dispersed

Table 5-5: Mechanical properties (indicative only) [66]

Specimen	Orientation	Tensile test results					Note
		Post process	Modulus of elasticity (E) (GPa)	Yield strength (MPa)	Ultimate tensile strength (UTS) (MPa)	Elongation (%)	
Specimen x1	ZX	AS	114 - 134	568 - 684	804-1030	12 - 28	1
Specimen x2		HT	155 - 175	900 - 1000	1150-1250	10 - 14	
Specimen x6	XY	AS	108 - 178	709 - 830	998-1100	22 - 32	
Specimen x7		HT	155 - 175	900 - 1000	1200 - 1300	10 - 14	
		AS		HT			
Hardness [HVD.5]	319-344		420-440			2	
Coefficient of thermal expansion [m/mK]	14 x 10 ⁻⁶					3	
Thermal conductivity [W/mK]	10 - 12						

Note:

1	Mechanical testing in accordance with ISO 6892
2	Hardness test in accordance with ASTM E384-11
3	In the range of 20°C(68°F) to 100°C(212°F)

Table 5-6: anisotropy change for modulus and elongation

Specimens	Tensile anisotropies parameters			
	E [GPa]	E [GPa] Anisotropies (%)	Elongation To Fracture [%]	Elongation To Fracture Anisotropies (%)
XY AS n.1	205	33.7	29	96 (14)
ZX AS n.1(specimen 1)	136		1.17 (25)	
XY AS n.2	224	39.7	27	84.1 (11)
ZX AS n.2(specimen 2)	135		4.3 (24)	
XY AS n.3	(178)	24.7	(32)	(12.5)
ZX AS n.3 (Estimated from table 5-7)	(134)		(28)	
XY HT n.1(specimen 6)	218	19.7	8.7 (11)	(9)
ZX HT n.1(estimated from table 5-7)	(175)		(10)	
XY HT n.2(specimen 7)	212	22.2	5.5 (13)	(8)
ZX HT n.2 (estimated from table 5-7)	(165)		(12)	
XY HT n.3	206	24.8	6.5 (12)	(17)
ZX HT n.3 (estimated from table 5-7)	(155)		(10)	
Anisotropy change 1		14		(5)
Anisotropy change 2		(17.5)		(3)
Anisotropy change 3		(-0.1)		(-4.5)

Estimated data are data represented in closed brackets (), were taken from table 5-5. The reason is that the experimental data are below the limit indicated in table 5-5.

From table 5-6, It can be observed that E , the anisotropy of the HT sample is improved by (43 MPa) 19.7% reduction compared to AS sample. Also, E_t has shown a slight improvement to 9% anisotropy reduction after HT. However, it should be noted that elongation was computed based on the the estimated data.

Anisotropy change 2 and 3 are not used due to estimated data are only for demonstration.

Table 5-7: anisotropy change for yield strength and UTS

		Tensile anisotropies parameters			
Specimens		σ_y [MPa]	σ_y [MPa] Anisotropies (%)	UTS [MPa]	UTS [MPa] Anisotropies (%)
XY AS n.1		732	31.7	1027.87	42.87
ZX AS n.1(specimen 1)		500		587.175605	
XY AS n.2		730	23.15	1030	26.6
ZX AS n.2(specimen 2)		561		756	
XY AS n.3		830	17.6	1049	12.6
ZX AS n.3	(Estimated from table 5-7)	684		917	
XY HT n.1(specimen 6)		1304	23.3	1368	9.4
ZX HT n.1 (estimated from table 5-7)		1000		1240	
XY HT n.2(specimen 7)		1303	23.5	1417	11.8
ZX HT n.2 (estimated from table 5-7)		1000		1250	
XY HT n.3		1295	22.8	1342	8.3
ZX HT n.3 (estimated from table 5-7)		1000		1230	
Anisotropy change 1			8.4		33.5
Anisotropy change 2			-0.35		18.3
Anisotropy change 3			-5.9		4.7

It can be observed in table 5-7, that σ_y , of HT sample was improved by (304 MPa) 23.3% anisotropy reduction compared to AS specimen. Also UTS , has improved by (128 MPa) 9.4% anisotropy reduction compared to AS specimen.

In conclusion, the anisotropy change 1 is 14%, 5%, 8.4%, 33.5% for E , E_t , σ_y and UTS respectively.

5.5 Analyse chemical composition for cube specimens: EDS/EDX map

5.5.1 Sample A2.1: AS

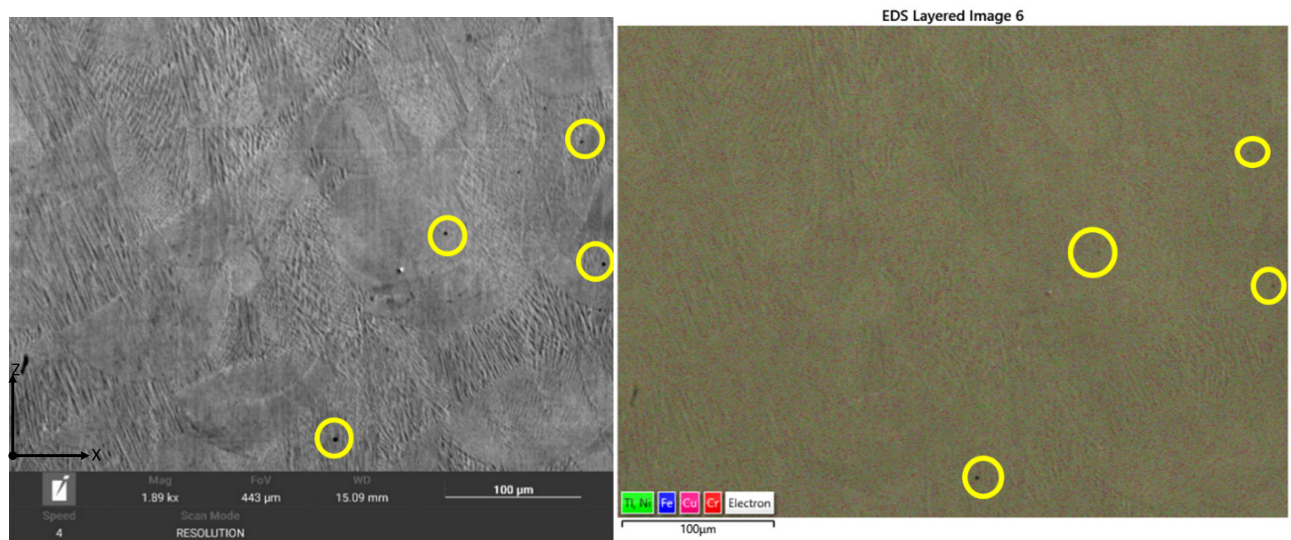


Figure 5-30: Sample A2.1 AS shows (a) SEM micrograph (b) EDS map

Figure 5-30 illustrates the SEM-EDS was utilized to observe the chemical composition in the In718 microstructure of a perpendicular deposition plane. Porosities (yellow circles) are seen on the microstructure. Then, by EDS map were obtained by EDX method as shown in Figure 5-31 to Figure 5-32 were obtained.

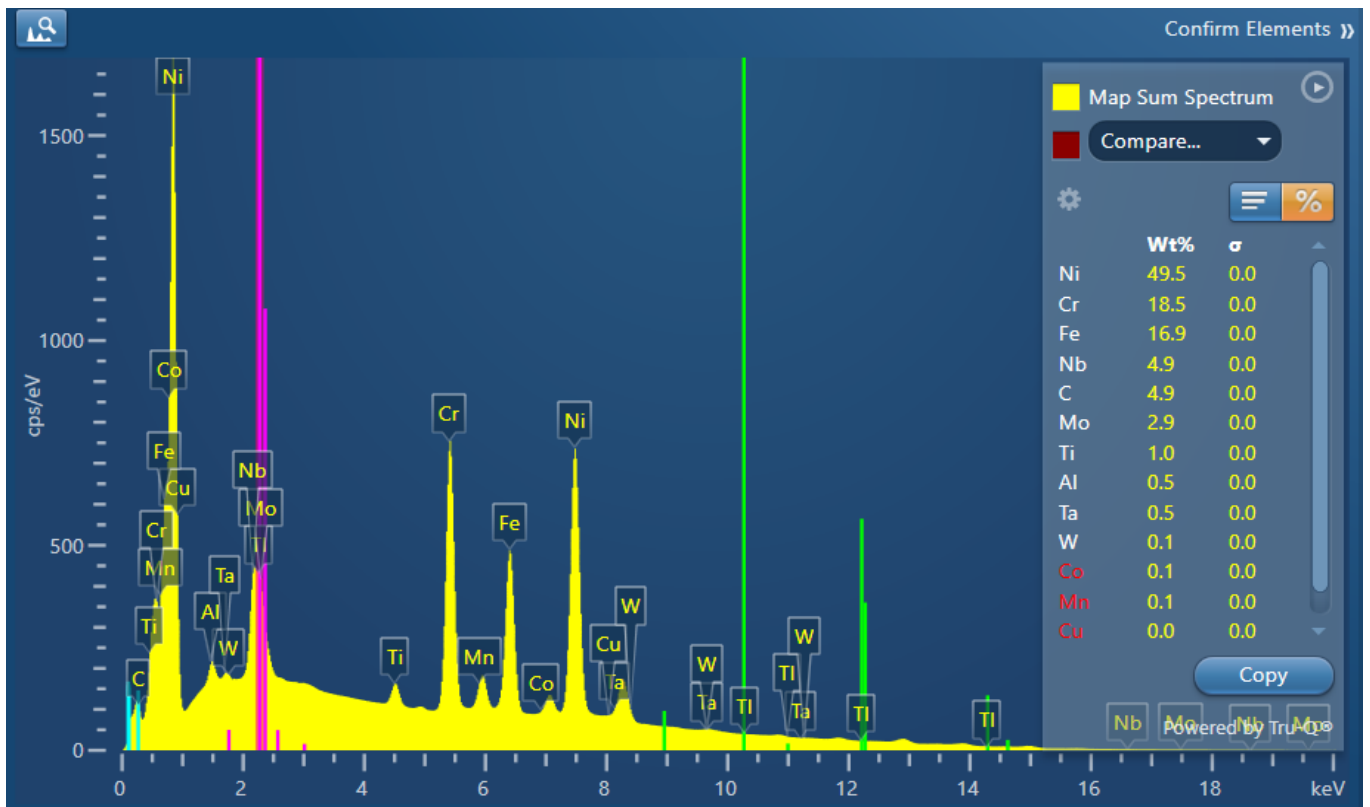


Figure 5-31: EDS map showing chemical compositions

Figure 5-31 shows the chemical composition by weight and is comparable from the manufacturer as shown in Table 4-1.

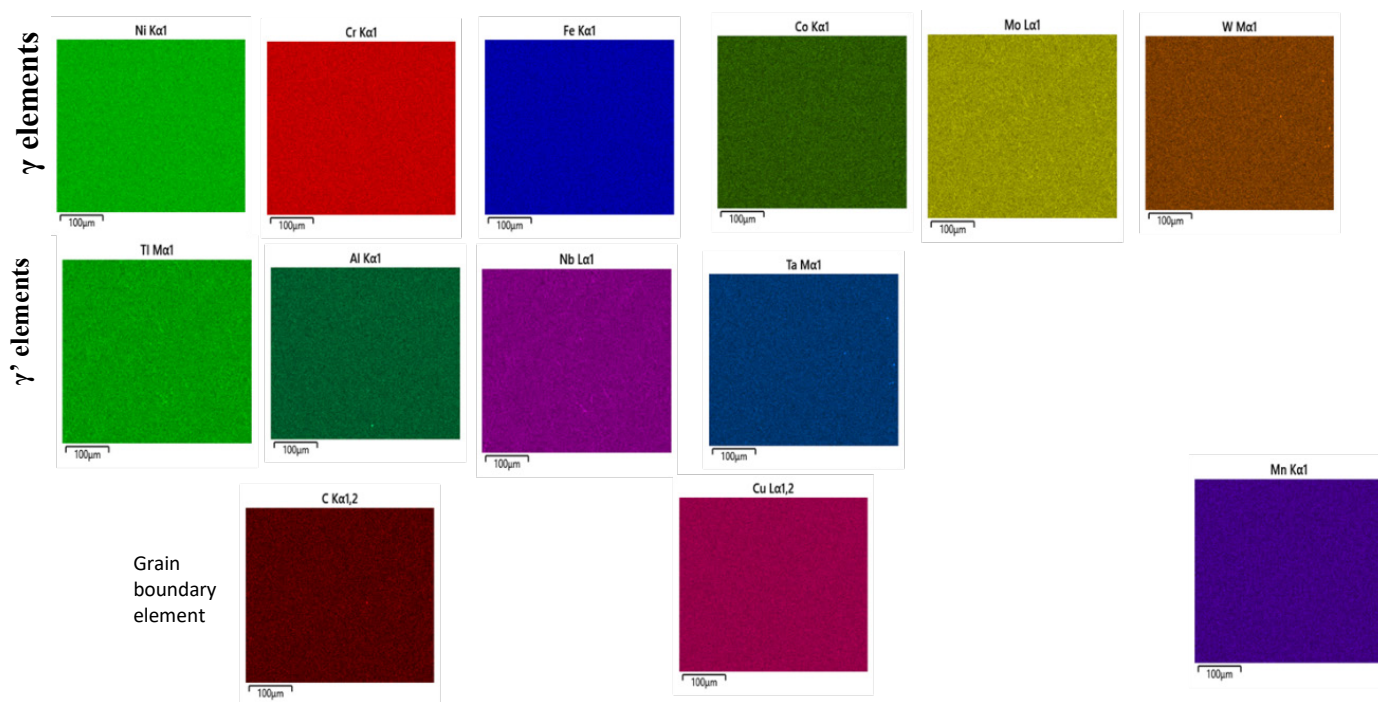


Figure 5-32: EDS map showing In718 precipitates

Key

Boundary strengtheners	B	C	Mg	Zr					
Partition to γ matrix	V	Cr	Mo	W	Re	Fe	Co	Ni	Y
Partition to γ'	Al	Ti	Nb	Hf	Ta				

Figure 5-32 illustrates In718 precipitates and its chemical composition. It is verified that by ageing the γ' precipitates were formed on the γ matrix.

5.6 Porosity analysis by using MATLAB code

By using the Matlab code known as SEM porosity app [67] [68], has enabled to obtain the porosity in fractions as shown in figure 5-33 to figure 5-38.

But, it should be noted that this method needs verification by using OM for measuring porosities.

In this thesis only MATLAB code was used.

5.6.1 Cube Sample A2.1: (ZX) AS

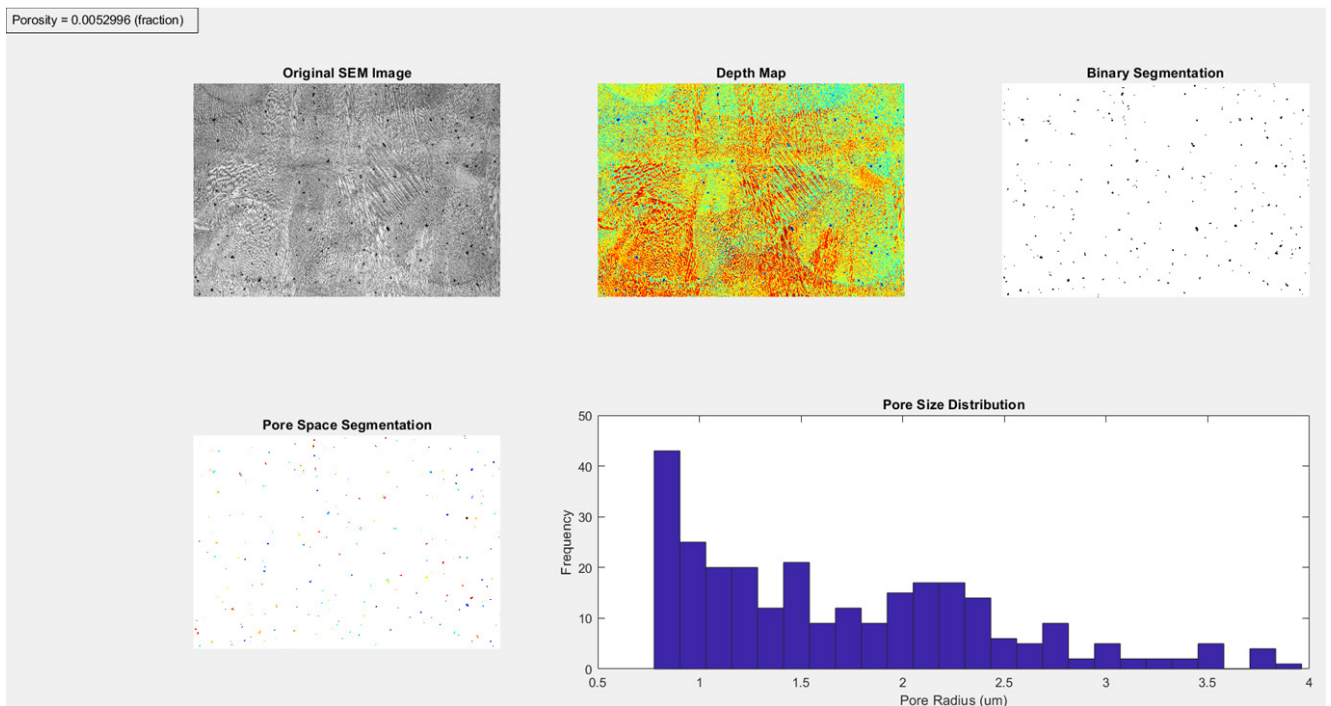
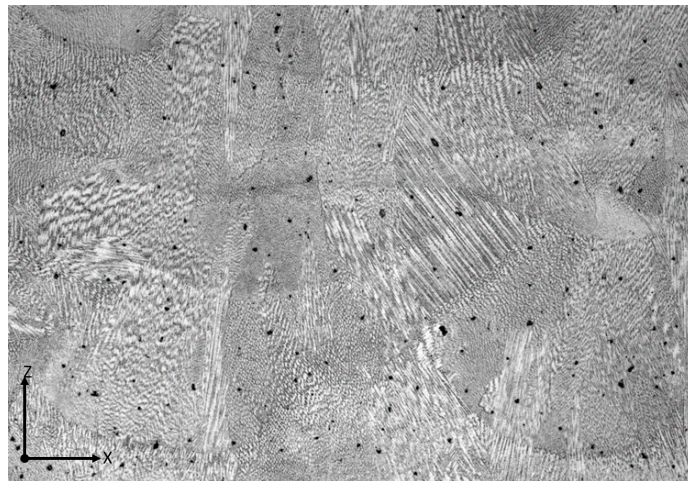


Figure 5-33: Cube Sample A2.1 porosities

Figure 5-33 illustrates, pores range from 0.5 to 3.5 μm as shown in the pore size distribution plot.

5.6.2 Cube Sample A2.2:(ZX) HT

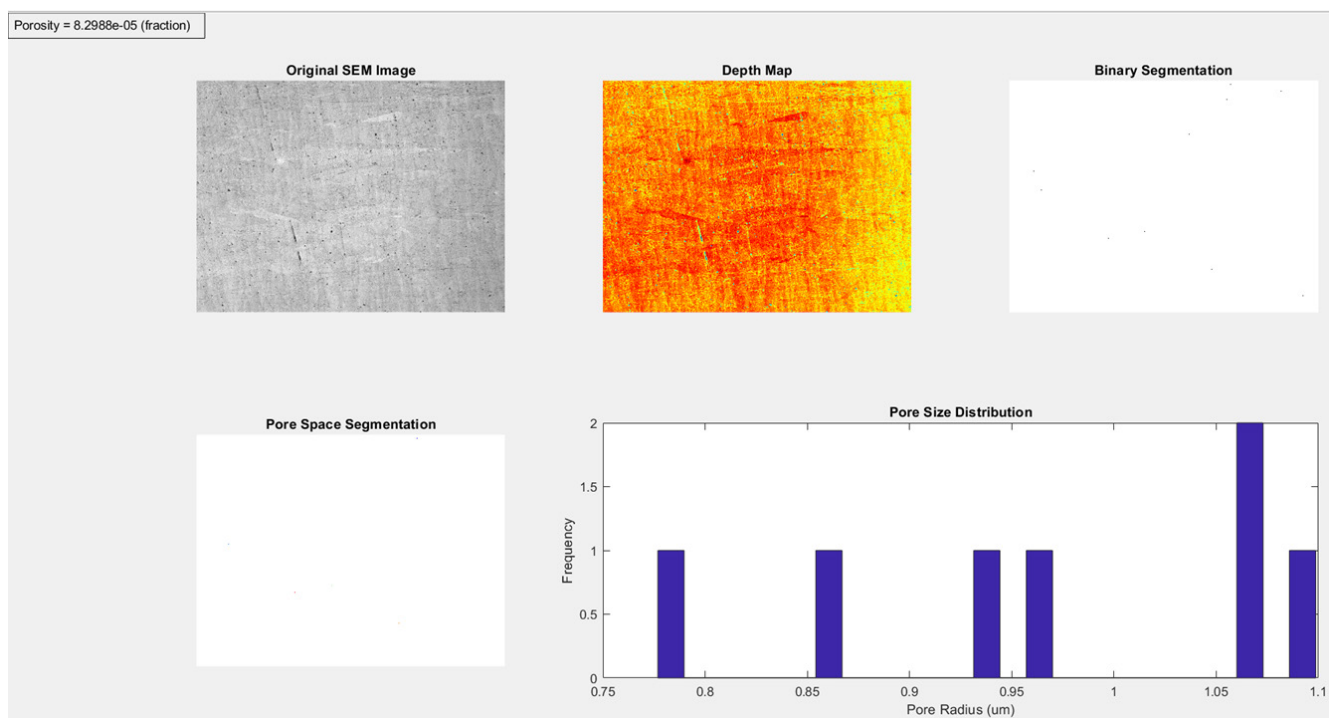
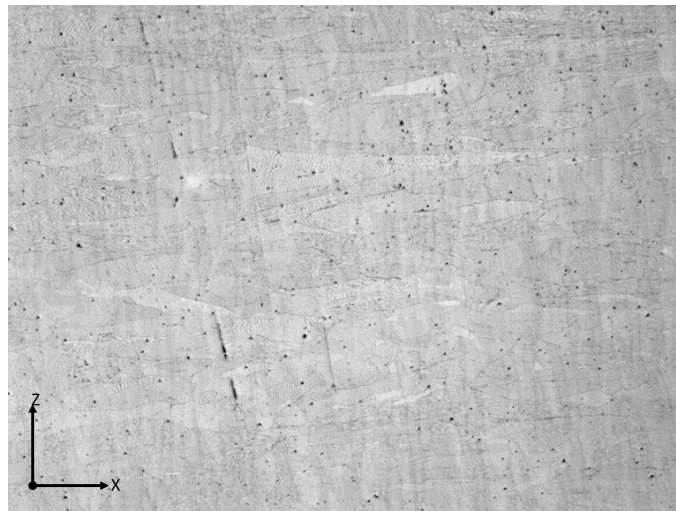


Figure 5-34: Cube Sample A2.2 porosities

Cube sample HT in ZX pores has been reduced compared to AS sample A2.1. It can be proved that HT close the pores. In Figure 5-34 reports, pore radius scattered from 0.5 to 1.1 μm as shown in the pore size distribution plot.

5.6.3 Cube Sample B2.1: (XY) AS

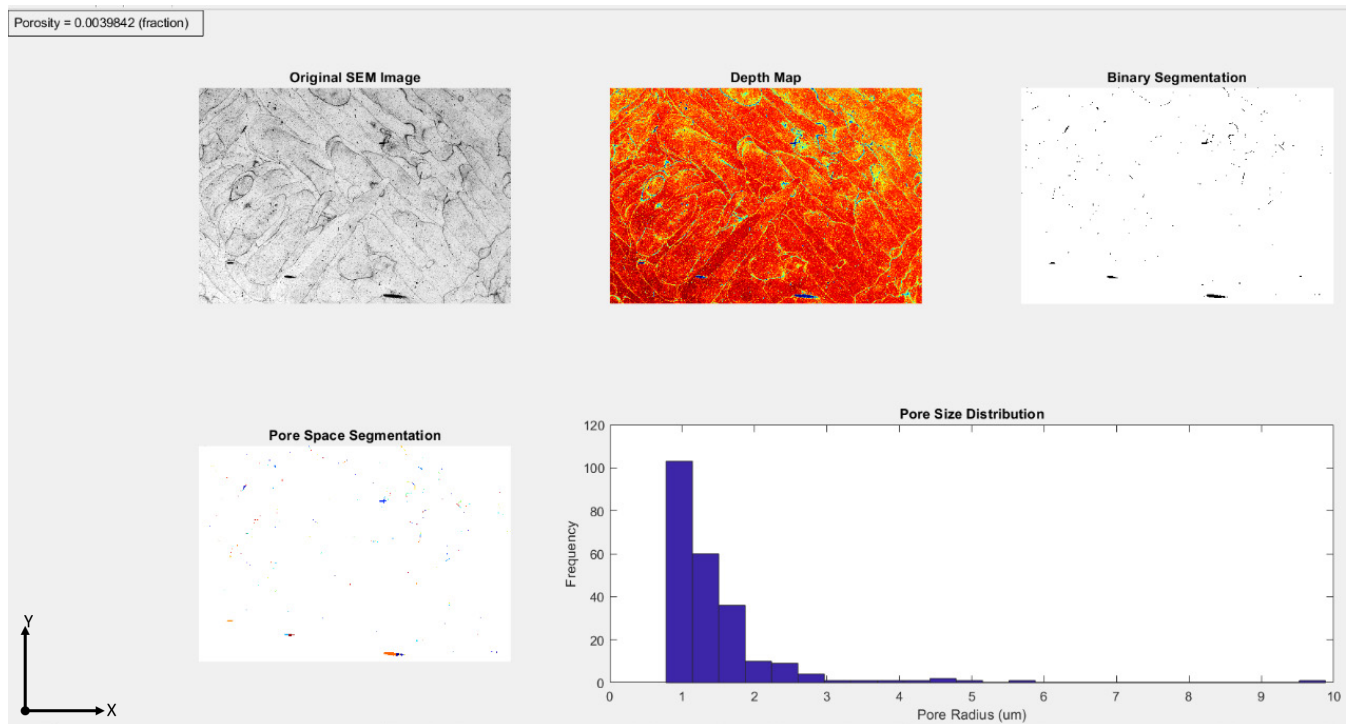


Figure 5-35: Cube Sample B2.1 porosities

Cube Sample B2.1 AS in XY has pores range from 0.8 to 5.8 μm . But most of the pores are concentrated between 0.8 to 3 μm as shown in Figure 5-35.

5.6.4 Cube Sample B2.2 (XY) HT

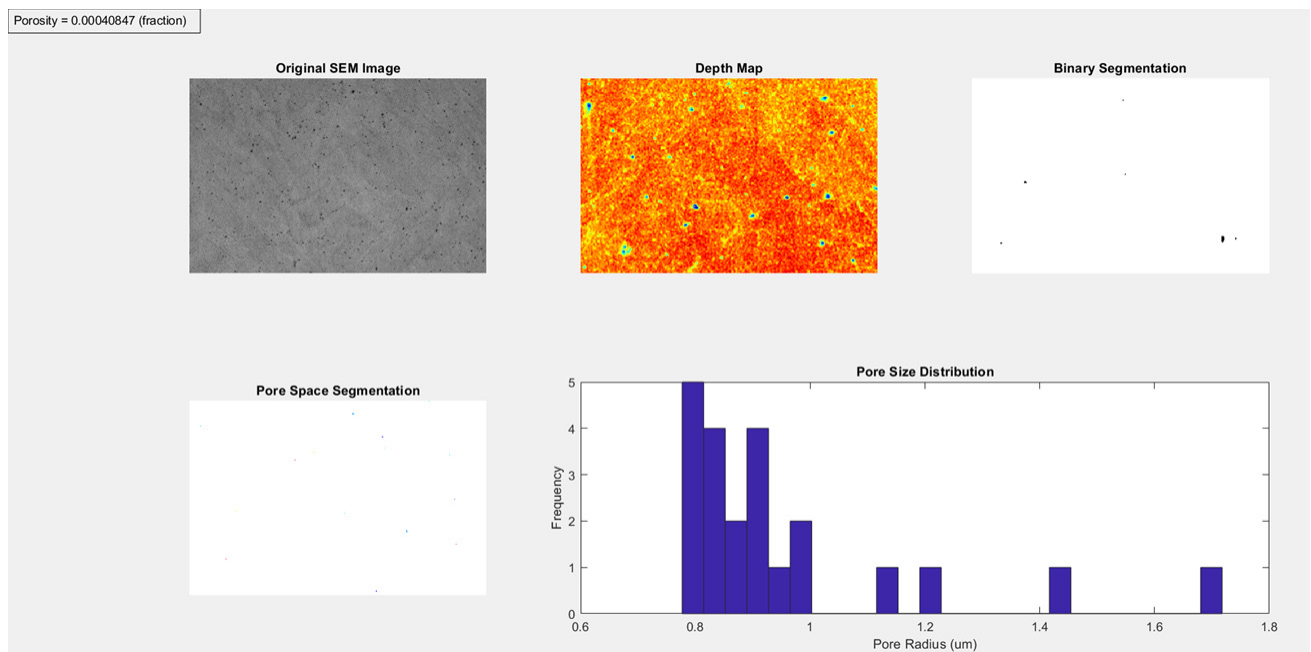
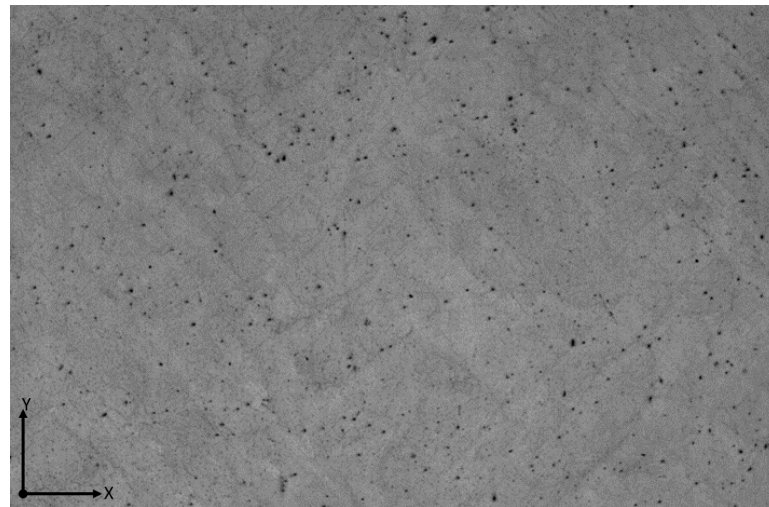


Figure 5-36: Cube Sample B2.2 porosities

Cube Sample B2.2 HT in XY has pores range from 0.7 to 1.7 μm . Again, most of the pores are concentrated between 0.7 to 1 μm . Hence, by HT has improved the microstructure by closing the pores as reported in Figure 5-36.

5.6.5 Cylindrical Specimen 1: (ZX) AS

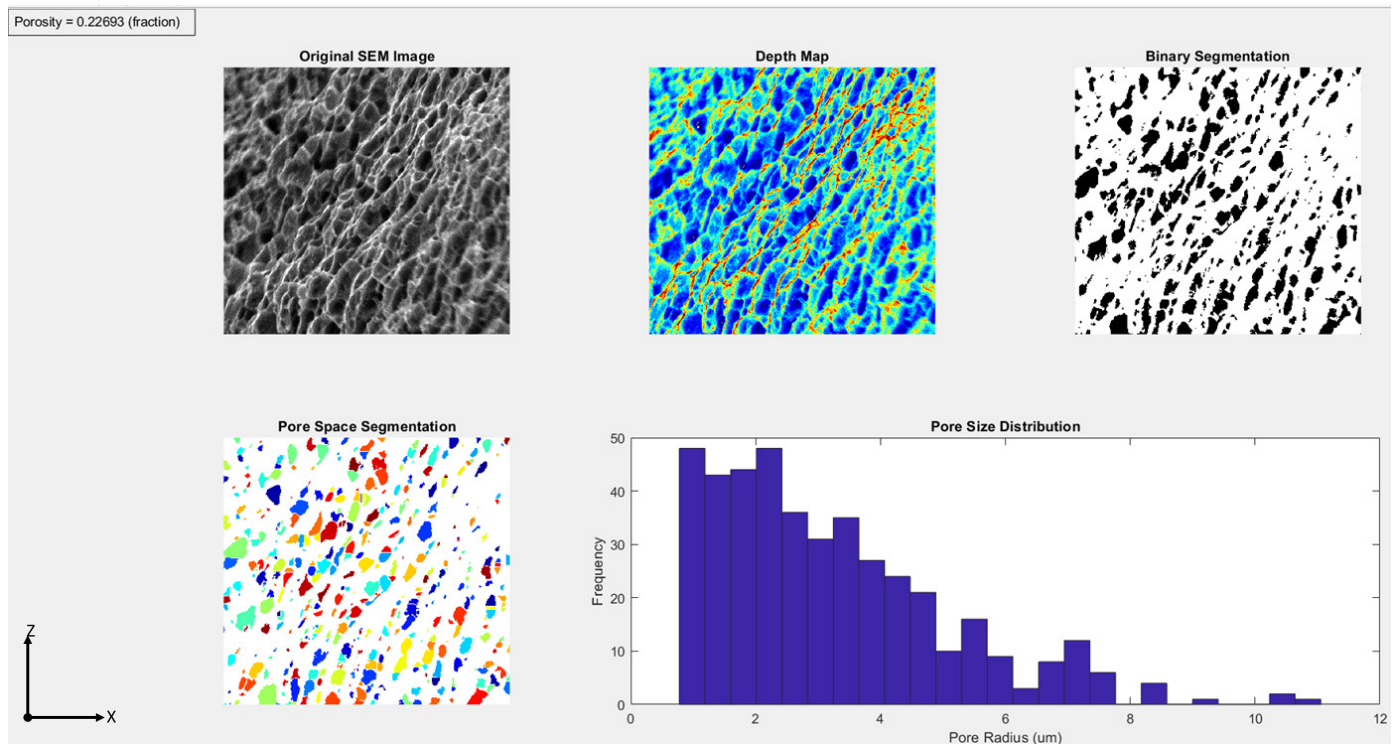


Figure 5-37: Cylindrical specimen 1 showing porosities

Cylindrical specimen 1 AS in ZX has pore radius that ranges from 1 to 11 μm . This is a fracture surface which is a ductile fracture with micro voids coalescence in Figure 5-37. These micro voids are mapped, and pore radius are big. And pore radius is concentrated between 1 to 7 μm . It can be related to Figure 5-17 and Figure 5-18, where pore diameters are 110-250 μm and 130-136 μm respectively.

5.6.6 Cylindrical Specimen 6 (XY): HT

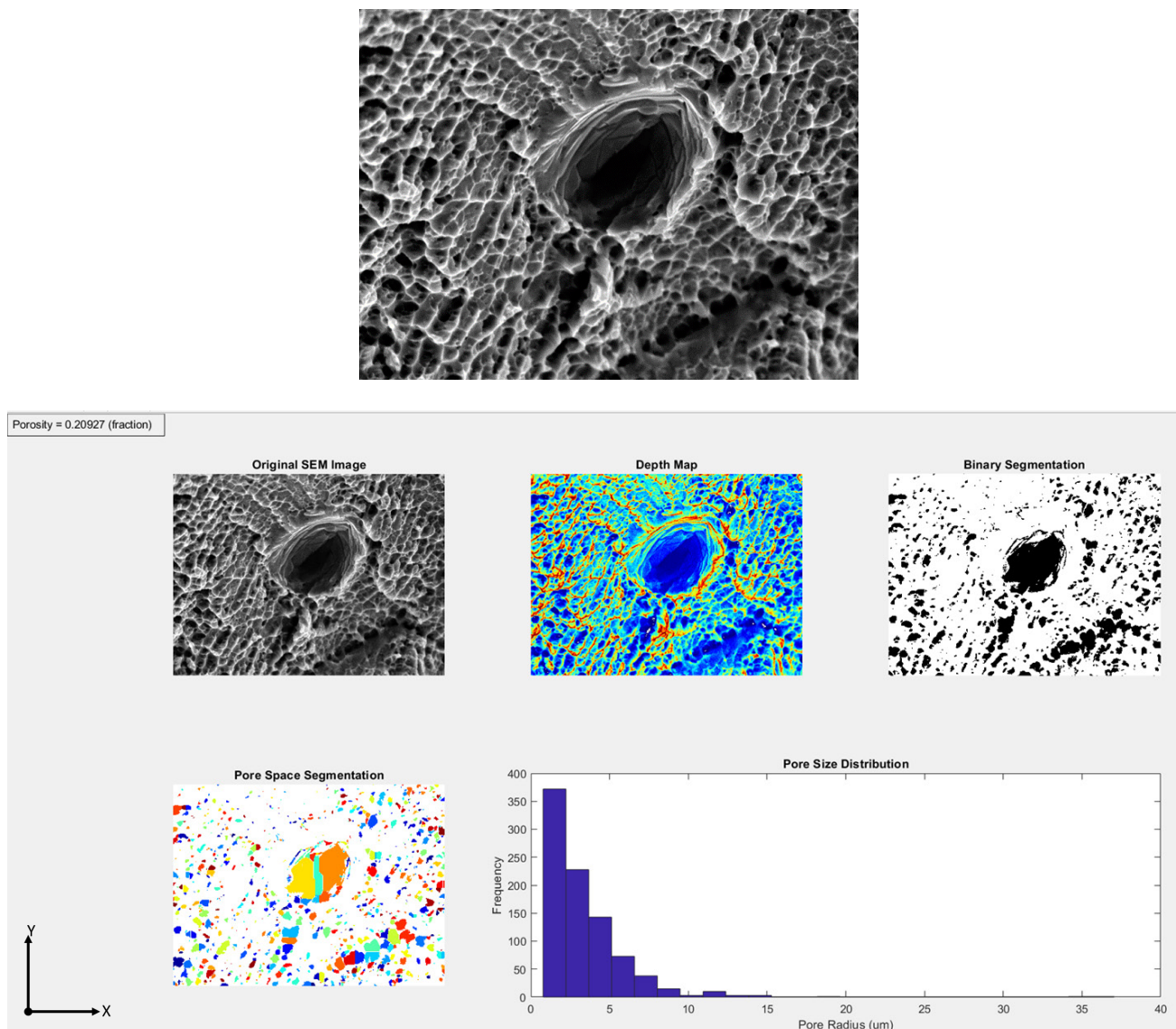


Figure 5-38: Cylindrical specimen 6 showing porosities

Cylindrical specimen 6 HT in XY has pore radius that ranges from 0.1 to 15 μm as shown in Figure 5-38. This is a fracture surface which is a ductile fracture with micro voids coalescence. These micro voids are mapped, and pore radius are small due to HT. And pore radius is concentrated between 0.1 to 8 μm .

It can be compared to Figure 5-23 and Figure 5-24 where pore diameters are 10 μm and 6 μm respectively.

5.6.7 Summary of porosity values of In718 superalloys specimens

It can be deduced that porosities are prevailing within the specimens as can be observed in table 5-8 porosities in fraction and table 5-9 porosities in percentages. Meaning the value are between 0 and 1. If we change the porosities from fraction into percentage, meaning values are between 0 to 100%.

Table 5-8: Summary of porosity values in fractions

Orientation	Post processing	Porosity [fractions]					
		Cube sample B2.2 (microstructure)	Cube sample B2.1 (microstructure)	Cube sample A2.2 (microstructure)	Cube sample A2.1 (microstructure)	Cylindrical specimen 1: AS (Fracture surface)	Cylindrical specimen 6: HT (Fracture surface)
XY	AS		0.0039842				
	HT	0.0040847					0.20927
ZX/ZY	AS				0.0052996	0.22693	
	HT			8.2988e-05			

Table 5-9: Summary of porosity values in percentages

Orientation	Post processing	Porosity [%]					
		Cube sample B2.2 HT (microstructure)	Cube sample B2.1 AS (microstructure)	Cube sample A2.2: HT (microstructure)	Cube sample A2.1 AS (microstructure)	Cylindrical specimen 1: AS (Fracture surface)	Cylindrical specimen 6: HT (Fracture surface)
XY	AS		0.39842				
	HT	0.40847					20.927
ZX/ZY	AS				0.52996	22.693	
	HT			0.0082988			

For the XY Cube specimen: HT sample B2.2 has a porosity of 0.41% higher than AS sample B2.1 with 0.40%. Here, OM is needed to re check the porosity in this samples. HT sample must have lower values of porosities because pores are closed during the heat treatment.

For the ZX cube specimen: AS sample A2.1 has a porosity of 0.53% lower than HT sample A2.2 with 0.0083%. This is consistent with the literature that pores are closed during the heat treatment.

For the cylindrical specimens: AS specimen 1, fracture surface has a porosity of 23% slightly lower than the HT specimen 6 with a value of 21%. Not so much different but due to micro voids

coalescence in both fractures that is why the values are higher when compared to the cube specimen.

From this results, it can hypothesized that porosity is the the cause of anistropies in tensile sumples of In718 superalloys.

It should be noted that, OM is needed to investigate the porosities in these specimens in order to obtain the correct values and better understand.

6 FEM analysis

ANSYS software by explicit dynamics is used to simulate the tensile test of specimen 8 (XY_AS) and specimen 6 (XY_HT) as shown in Figure 6-1 and Figure 6-2 respectively. The results are provided below. The same procedure can be used for specimen 1 (ZX_AS), specimen 2 (ZY_HT).

Equations 6.1 to 6.4 were used to obtain the ANSYS setting parameters:

$$c = \sqrt{\frac{\text{young's modulus}}{\text{density of solid}}} = \sqrt{\frac{E(1 - \nu)}{\rho(1 + \nu)(1 - 2\nu)}} \dots \dots \dots 6.1$$

$$\Delta t = f \times \frac{L}{c} \dots \dots \dots 6.2$$

$$\varepsilon = \frac{\Delta L}{L} \dots \dots \dots 6.3$$

$$\text{Factor of safety} = \frac{\text{tensile yield strength}}{\text{von mises stress}} \dots \dots \dots 6.4$$

Specimen 8 (XY_AS). XY AS

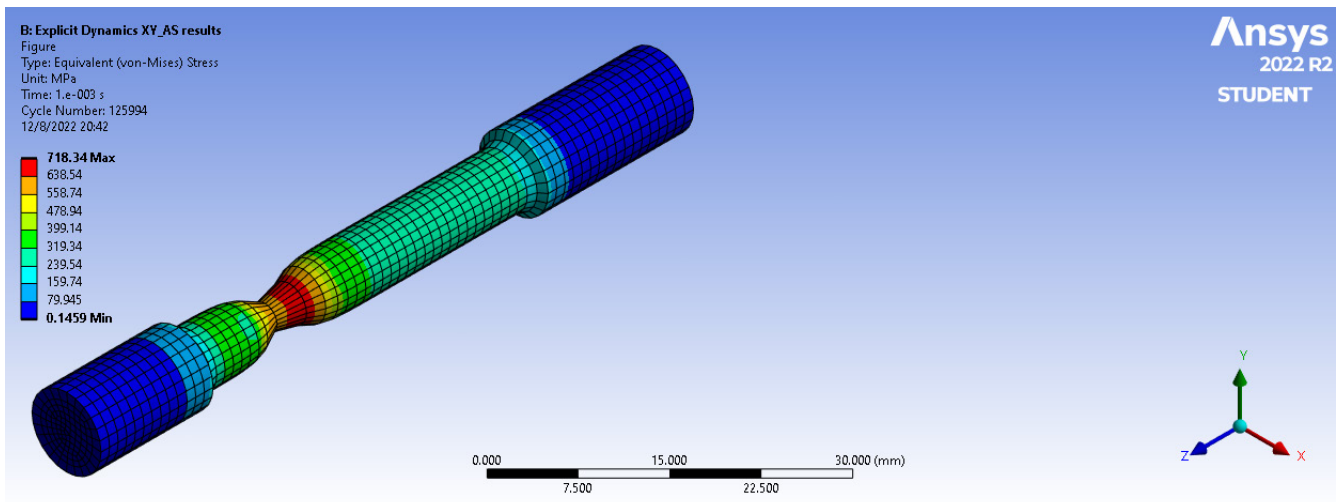


Figure 6-1: Specimen 8 (XY_AS). XY AS

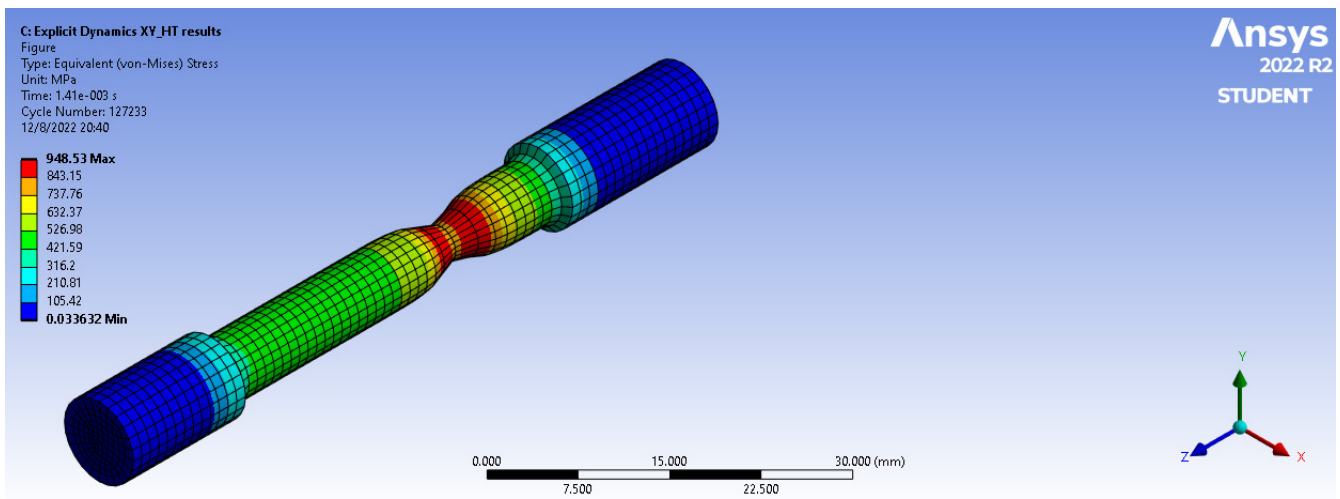


Figure 6-2: Specimen 6 (XY_HT)

7 Conclusion and future work

The aim of this thesis is to investigate the fracture behaviour of In718 specimens by means of fracture surface analysis.

The investigation was run by means of in situ scanning electron microscopy (SEM) and optical microscopy (OM) of specimen fracture surfaces from tensile tests and surfaces of cubic samples obtained by LPBF in AM.

The tensile test operated at room temperature is performed on cylindrical specimens obtained with axis parallel and perpendicular to deposition plane. EDX analysis was used to characterize the chemical composition of In718 superalloy cube samples and its powder particles.

The analysis was extended to specimens obtained with axis parallel to deposition direction and to perpendicular direction, and before and after heat treatment

Fracture samples were characterized by SEM, SEM-EDS/EDX and OM. Elongated columnar dendrites, lack of fusion, melt pools and porosities were observed.

The tensile anisotropies range of variation between specimens obtained with axis parallel to deposition direction and to perpendicular direction are 14%, 5%, 8.4%, 33.5% for E , E_l , σ_y and UTS respectively.

For specimens which underwent heat treatment, microstructure anisotropies resulted to be reduced. During HT, recrystallization enabled pores to be closed and hence reduced porosities, residual stresses and lack of fusion problems. For the perpendicular and parallel deposited AS specimens the porosities were 0.53% and 0.40% respectively. The perpendicular and parallel orientation HT specimens with porosities density resulted of 0.0083% and 0.41% respectively. For the perpendicular specimens the porosity values are consistent with the literature that pores are closed during the heat treatment. However, the parallel deposited build specimens were not consistent with the literature because it means pores were not closed after HT or there is another problem of elongated grain which can be answered by SEM-EBSD and porosities can be measured by OM to recheck these results.

AS perpendicular and HT parallel deposited cylindrical fracture surfaces have a porosity of 23% and 21% respectively. Not so much difference but due to micro voids coalescence. Also, we can not compare because heat treated perpendicular and as build parallel deposited cylindrical samples were not available for examination.

In the future work, heat treatment is needed to be redesigned in order to obtain isotropy of In718 superalloys.

8 Reference

- [1] M. J. Donachie and S. J. Donachie, *Superalloys A Technical Guide*, 2002.
- [2] S. Mankandani and D. Sivakumar, *Welding the Inconel 718 superalloys*.
- [3] M. G. Burke and T. R. Mager, ““The effect of thermal treatment on SCC of alloy 718: A structure-properties study”,” 1994.
- [4] T. Alam, “Precipitation and clustering in the early stages of ageing in Inconel 718,” 2010.
- [5] R. Kelkar, A. Andreaco, E. Ott and J. Groh, “Alloy 718: laser powder bed additive manufacturing for turbine applications,” 2018.
- [6] R. Schafrik, D. Ward and J. Groh, “Application of Alloy 718 in GE Aircraft Engines: Past, Present and Next Five Years. Superalloys 718, 625, 706 and Various Derivatives,” pp. 1-11, 2001.
- [7] N. Quy Bau, L. Mui, N. Sharon, Z. Zhiguang, S. Chen-Nan, W. Jun and Z. Wei, “Characteristics of Inconel Powders for Powder-Bed Additive Manufacturing,” 2017.
- [8] FAA, “Accident Overview of National Airlines Flight 27,” 1975.
- [9] V. Popovich, “Functionally graded Inconel 718 processed by additivemanufacturing: Crystallographic texture, anisotropy of microstructure and mechanical properties,” 2016.
- [10] C.-T. S. Maldonado, “Hydrogen Embrittlement of Pre-Cathodically Hydrogen Charged Inconel 718 Fabricated via Selective Laser Melting: Fracture and Crack Propagation via 3D EBSD,” 2022.
- [11] R. M’Saoubi and et al., “Surface integrity analysis of machined Inconel 718 over multiple length scales,” 2012.
- [12] J. Schröder, “On the influence of heat treatment on microstructure and mechanical 1 behavior of Laser Powder Bed Fused Inconel 718,” 2020.
- [13] International, SAE, “AMS5662: UNS N07718 1775 _F (968 _C) Solution Heat Treated, Precipitation Hardenable,” 2016.

- [14] K. Gruber, I. Smolina, M. Kasprowicz and T. Kurzynowski, "Evaluation of Inconel 718 Metallic Powder to Optimize the Reuse of Powder and to Improve the Performance and Sustainability of the Laser Powder Bed Fusion (LPBF) Process," 2021.
- [15] A. Spierings, M. Voegtlin, T. Bauer and K. Wegener, "Powder flowability characterisation methodology for powder-bed-based metal additive manufacturing," 2016.
- [16] J. Fox, S. Moylan and B. Lane, "Effect of process parameters on the surface roughness of overhanging structures in laser powder bed fusion additive manufacturing".
- [17] M. Brandt, Laser Additive Manufacturing. Materials, design, technologies and applications, 2016.
- [18] J. Strößner, M. Terock and U. Glatzel, "Mechanical and microstructural investigation of nickel-based superalloy IN718 manufactured by selective laser melting (SLM)," 2015.
- [19] VDI, "Status report. Additive Fertigungsverfahren," 2014.
- [20] T. Lore, V. Bey, J. Kruth and J. V. Humbeeck, "The influence of process parameters and scanning strategy on the texture in ti6al4v part produced by selective laser melting".
- [21] T. Wischeropp, "Advancement of Selective Laser Melting," 2021, p. 10.
- [22] T. Tanja, "Microstructure and mechanical properties of selective laser melted Inconel 718 compared to forging and casting," 2016.
- [23] Y. Wang and J. Shi, "Developing very strong texture in a nickel-based superalloy by selective laser melting with an ultra-high power and flat-top laser beam," 2020.
- [24] M. S. John J. Lewandowski, "Metal Additive Manufacturing A Review of Mechanical Properties," 2016.
- [25] X. Wu, "On direct laser deposited Hastelloy X: dimension, surface finish, microstructure and mechanical properties'," 2011.
- [26] W. Sames, S. Pannala and R. R. Deho, "The metallurgy and processing science of metal additive manufacturing," 2016.
- [27] T. Srivatsan and T. Sudarshan, Additive manufacturing innovations, advances, and applications, 2016.

- [28] L. N. Carter, M. M. Attallah and R. C. Reed, "Laser Powder Bed Fabrication of Nickel-Base Superalloys: Influence of Parameters; Characterisation, Quantification and Mitigation of Cracking," 2012.
- [29] H. Wan, "Effect of scanning strategy on mechanical properties of selective laser melted Inconel 718," 2019.
- [30] H. Gong, D. Christiansen, J. Beuth and J. J. Lewandowski, "Melt Pool Characterization for Selective Laser Melting of Ti-6Al-4V Pre-alloyed Powder. Solid Freeform Fabrication Symposium, pages 256–267.," 2014.
- [31] C. T. Sims, N. S. Stoloff and W. C. Hagel, *Superalloys II: High-Temperature Materials for Aerospace and Industrial Power*.
- [32] L. N. Carter, M. Christopher, P. J. Withers and M. M. Attallah, "The influence of the laser scan strategy on grain structure and cracking behaviour in SLM powder-bed fabricated nickel superalloy," 2014.
- [33] Y. Lu, S. Wu, Y. Gan, T. Huang, C. Yang, L. Junjie and J. Lin, "Study on the microstructure, mechanical property and residual stress of SLM Inconel-718 alloy manufactured by di_ering island scanning strategy," 2015.
- [34] M. Crachi, "Thermo-structural analysis and associated experimental characterization of an innovative metal-matrix-composite copper-steel material for a new Liquid Rocket Engine (LRE) thrust chamber geometry processed by SLM Additive Manufacturing," 2022.
- [35] ISO/ASTM, "Standard terminology for additive manufacturing-coordinate systems and test methodologies.," 2013.
- [36] H. Helmer, A. Bauereiß, R. Singer and C. Körner, "Grain structure evolution in Inconel 718 during selective electron beam melting".
- [37] B. Shassere, D. Greeley, A. Okello, M. M. Kirka, P. Nandwana and R. Deho, "Correlation of Microstructure to Creep Response of Hot Isostatically Pressed and Aged Electron Beam Melted Inconel 718.," 2018.
- [38] S. Plimpton, A. Thompson and A. Slepoy, "SPPARKS pin command.," 2017.
- [39] F. R. Caliari, "Study of the mechanical behavior of an Inconel 718 aged superalloy submitted to hot tensile tests," 2011.

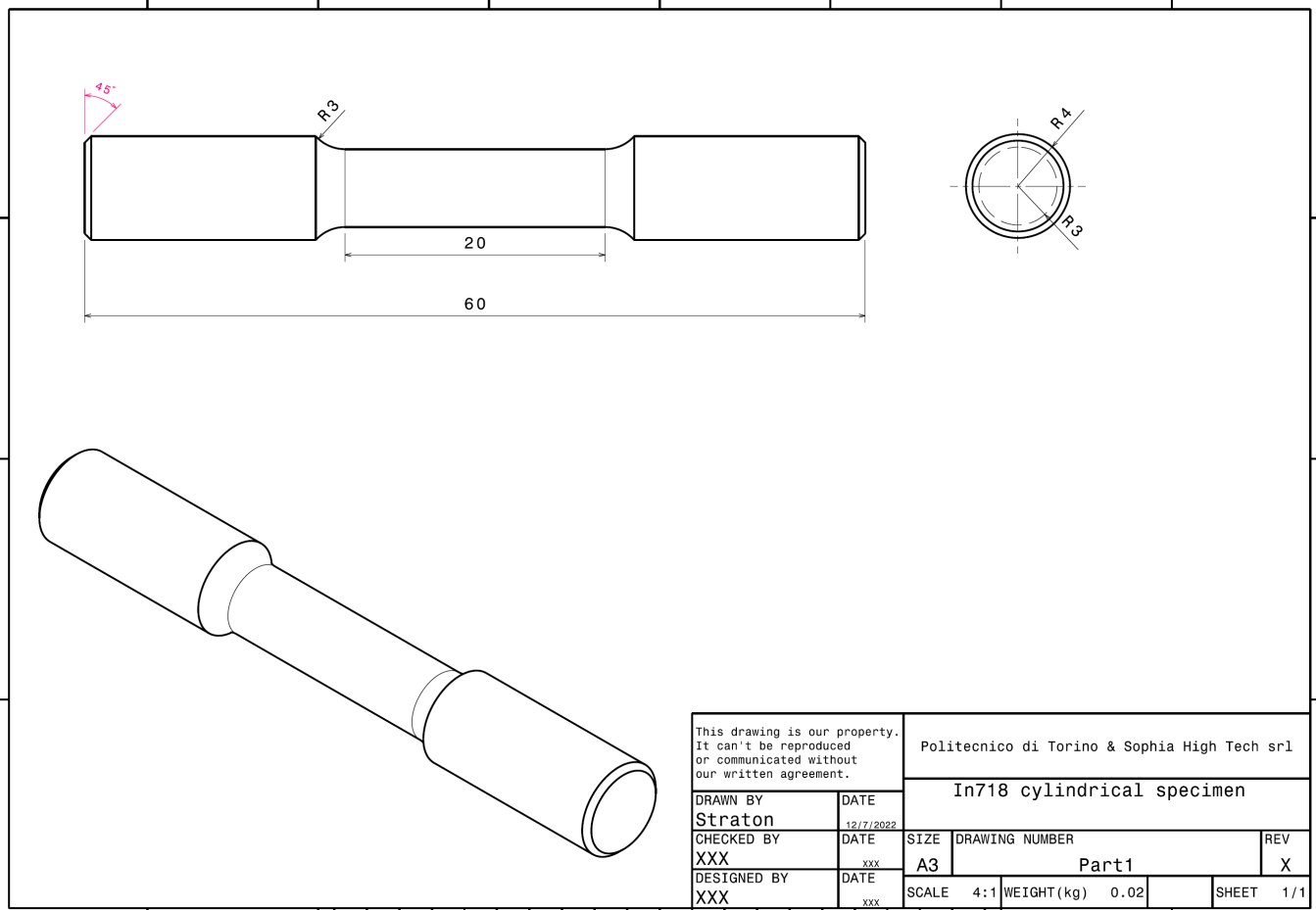
- [40] J. C. Williams and J. Edgar A. Starke, "Progress in structural materials for aerospace systems," 2003.
- [41] C. Tan, K. Zhou, W. Ma, Zhang, M. Liu and T. Kuang, "Microstructural evolution, nanoprecipitation behavior and mechanical properties of selective laser melted high-performance grade 300 maraging steel," 2017.
- [42] S. Kou, "Welding metallurgy. 2nd ed.," 2003.
- [43] A. Hozoorbakhsh, "A computational analysis of heat transfer and fluid flow in high-speed scanning of laser micro-welding, International Communications in Heat and Mass Transfer," 2015.
- [44] J. Chen and R. Cao, *Micromechanism of Cleavage Fracture of Metals*, 2014.
- [45] W. D. Callister and D. G. Rethwisch, *Materials science and engineering*, 8th edition, callister.
- [46] D. FIRRAO, "The role of fractography in failure analysis," in *ESIS Summer School* , 2016.
- [47] L. Carter, "Process optimisation of selective laser melting using energy density model for nickel based superalloys," 2016.
- [48] K. Kunze, "Texture, anisotropy in microstructure and mechanical properties of IN738LC alloy processed by selective laser melting (SLM). *Materials Science and Engineering A*, 620:213–222.," 2014.
- [49] A. Mostafa, I. Picazo Rubio, V. Brailovski, M. Jahazi and M. Medraj, "Structure, Texture and Phases in 3D Printed IN718 Alloy Subjected to Homogenization and HIP Treatments," 2017.
- [50] J. Alcisto, A. Enriquez and H. Garcia, "Tensile Properties and Microstructures of Laser-Formed Ti-6Al-4V," 2011.
- [51] O. Scott-Emuakpor and J. Schwartz, "Bending fatigue life characterisation of direct metal laser sintering nickel alloy 718," 2015.
- [52] Argenio, F. Caiazzo, V. Alfieri and G. Corrado, "Laser powder-bed fusion of Inconel 718 to manufacture turbine blades," 2017.

- [53] V. A. Popovich, "Microstructure and mechanical properties of Inconel 718 produced by SLM and subsequent heat treatment," 2015.
- [54] X. Cao, B. Rivaux, M. Jahazi, J. Cuddy and A. Birur, "Effect of pre- and post-weld heat treatment on metallurgical and tensile properties of Inconel 718 alloy butt joints welded using 4kW Nd:YAG laser," 2009.
- [55] H. Qi, M. Azer and A. Ritter, "Studies of standard heat treatment effects on microstructure and mechanical properties of laser net shape manufactured INCONEL 718," 2009.
- [56] Y. N. Zhang, X. Cao, P. Wanjara and M. Medraj, "Tensile properties of laser additive manufactured Inconel 718 using filler wire," 2014.
- [57] W. A. Tayon, R. N. Shenoy, M. R. Redding, R. K. Bird and R. A. Hafley, "Correlation between microstructure and mechanical properties in an Inconel 718 deposit produced via electron beam freeform fabrication," 2014.
- [58] R. Bird and J. Hibberd, "Tensile properties and microstructure of Inconel 718 fabricated with electron beam freeform fabrication (EBF3).," 2009.
- [59] X. Zhao, J. Chen, X. Lin and W. Huang, "Study on microstructure and mechanical properties of laser rapid forming Inconel 718," 2008.
- [60] P. L. Blackwell, "The mechanical and microstructural characteristics of laser-deposited IN718," 2005.
- [61] B. Baufeld, "Mechanical properties of INCONEL 718 parts manufactured by shaped metal deposition," 2012.
- [62] Y. Wang and J. Shi, "Developing very strong texture in a nickel-based superalloy by selective laser melting with an ultra-high power and flat-top laser beam," 2020.
- [63] M. Godec, S. Malej and D. Feizpour, "Hybrid additive manufacturing of Inconel 718 for future space applications," 2021.
- [64] Y. Kaynak and E. Tascioglu, "Post-processing effects on the surface characteristics of Inconel 718 alloy fabricated by selective laser melting additive manufacturing".
- [65] Y. Kaynak and O. Kitay, "The effect of post-processing operations on surface characteristics of 316L stainless steel produced by selective laser melting.," 2019.

- [66] Sophia High Tech Srl.
- [67] A. Rabbani and S. Salehi, "Dynamic modeling of the formation damage and mud cake deposition using filtration theories coupled with SEM image processing," 2017.
- [68] C. P. Ezeakacha, A. Rabbani, S. Salehi and A. Ghalambor, "Integrated Image Processing and Computational Techniques to Characterize Formation Damage," 2018.
- [69] Normung DIN Deutsches Institut für, Additive Fertigung. Grundlagen, 2018.
- [70] Y. Kaynak and E. Tascioglu, "Post-processing effects on the surface characteristics of Inconel 718 alloy fabricated by selective laser melting additive manufacturing".
- [71] J. C. Williams and E. A. Starke, "Progress in structural materials for aerospace systems," 2003.
- [72] L. N. Carter and X. Wang, "Process optimisation of selective laser melting using energy density model for nickel based superalloys," 2016.

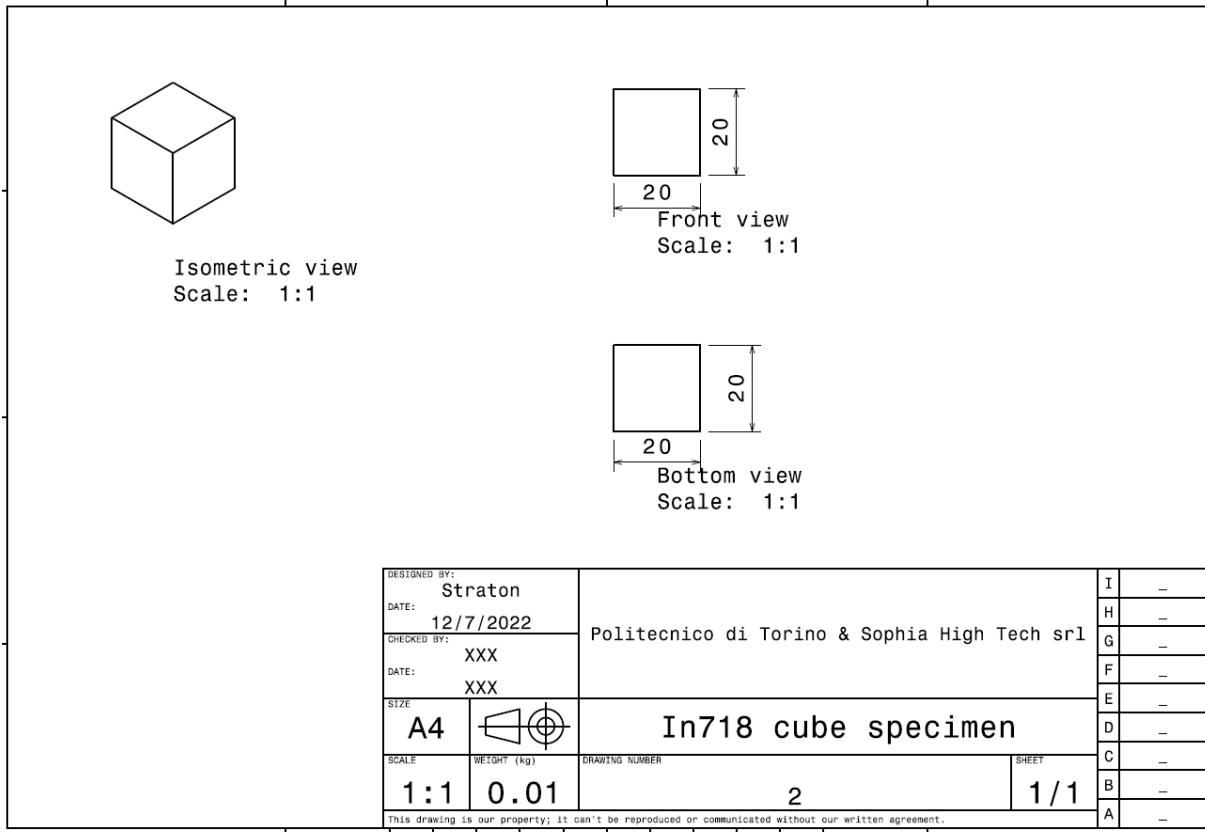
9 Appendix

9.1 Appendix A: In718 cylindrical specimen drawing



This drawing is our property. It can't be reproduced or communicated without our written agreement.		Politecnico di Torino & Sophia High Tech srl	
DRAWN BY Straton		In718 cylindrical specimen	
CHECKED BY XXX	DATE 12/17/2022	SIZE A3	DRAWING NUMBER Part1
DESIGNED BY XXX	DATE xxx	SCALE 4:1	WEIGHT (kg) 0.02
			SHEET 1/1

9.2 Appendix B: In718 cube specimen drawing



9.3 Appendix C: SEM Micrograph in Image J and PSD results by Origin Pro:

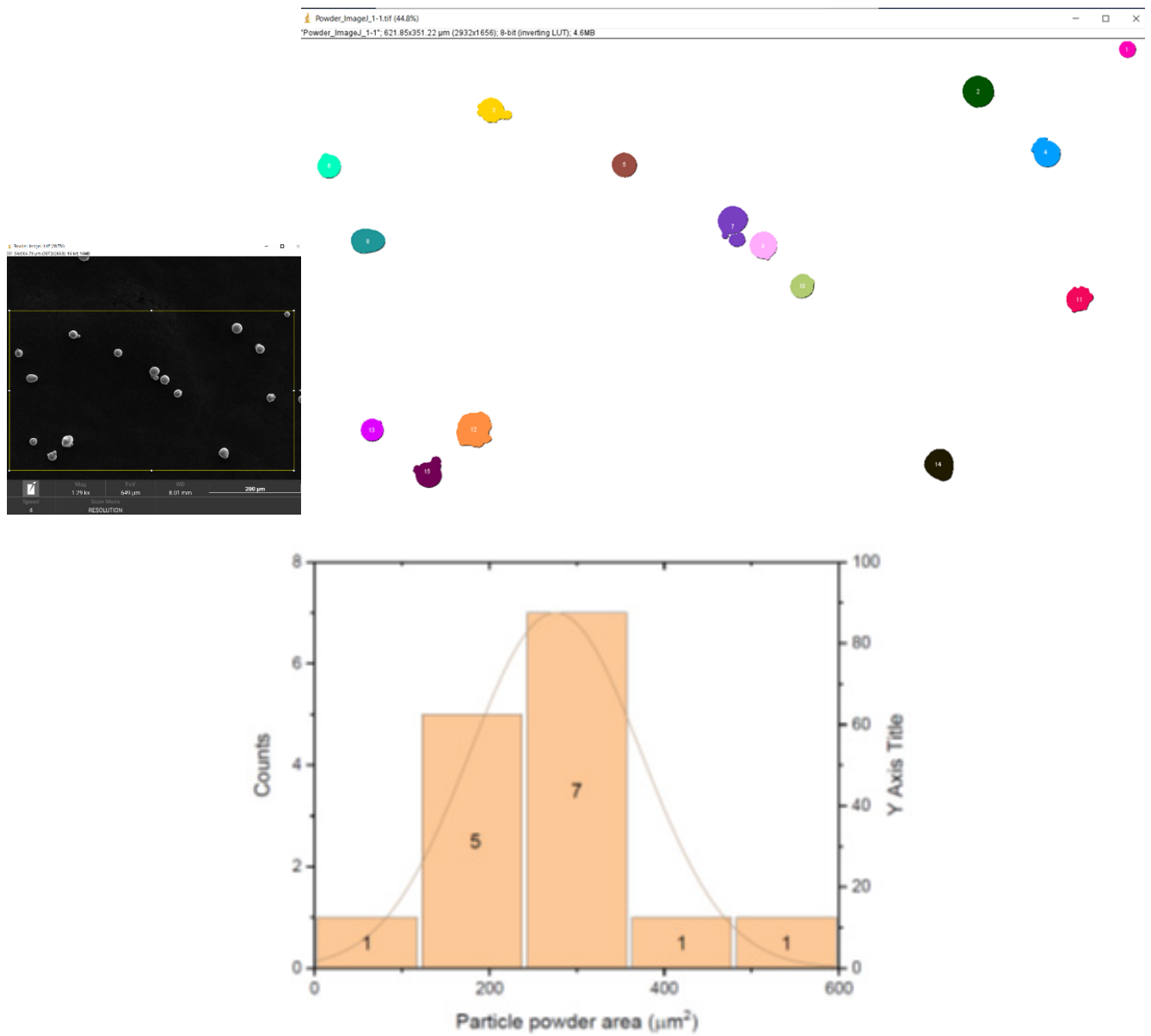


Figure 9-1: (a & c) Image J sample analysis (c) Powder size distribution (PSD)

9.4 Appendix D: SEM Micrograph:

Specimen 1

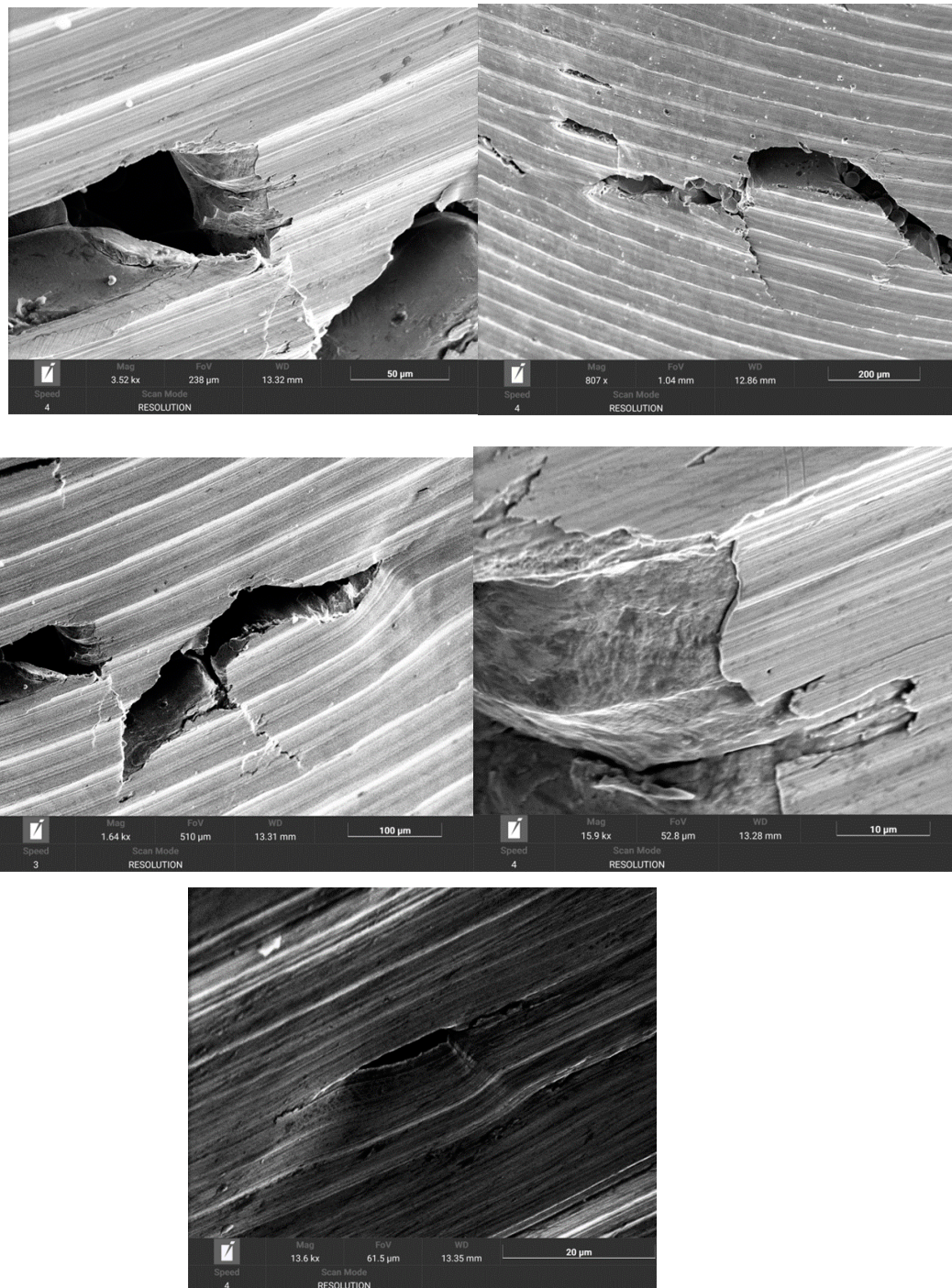


Figure 9-2: Lateral surface showing the primary cracks as resulted due to the effect of machining, lack of fusion and porosity

Specimen 7 (Parallel deposition plane)

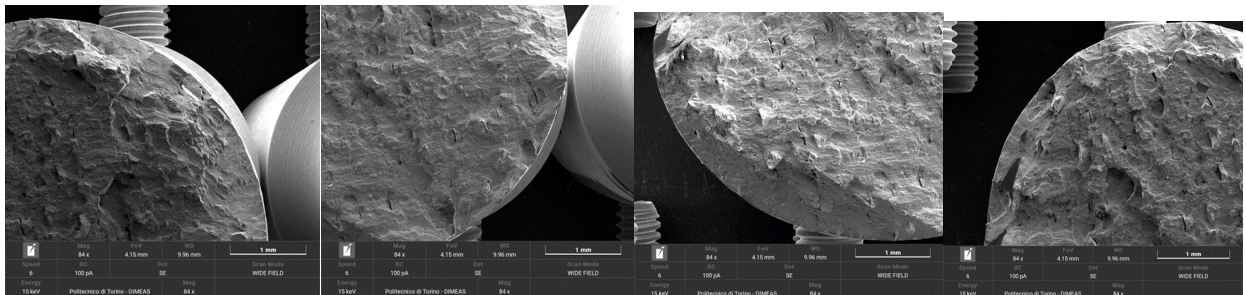
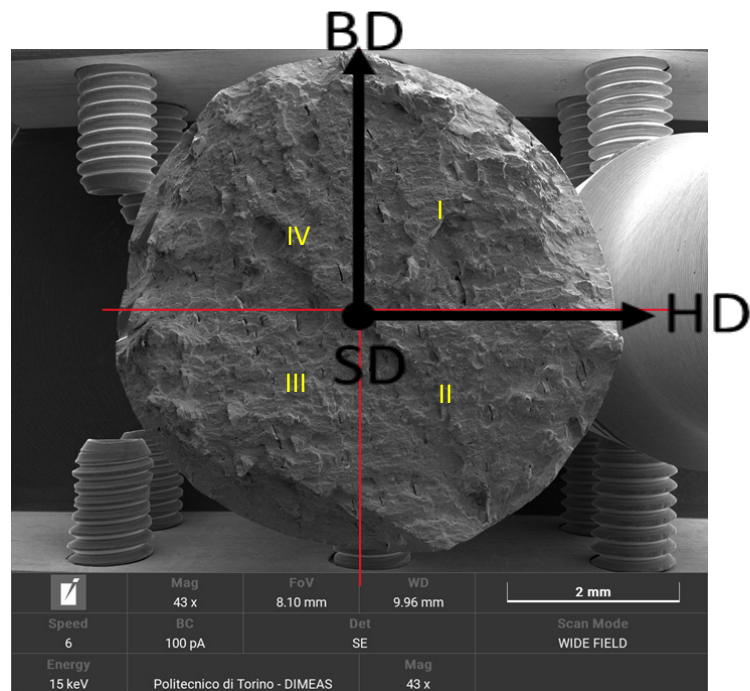


Figure 9-4: Tensile fracture surface of horizontally (XY) built Inconel 718 sample tested Heat treated, (a) overall view showing a smooth flat surface,

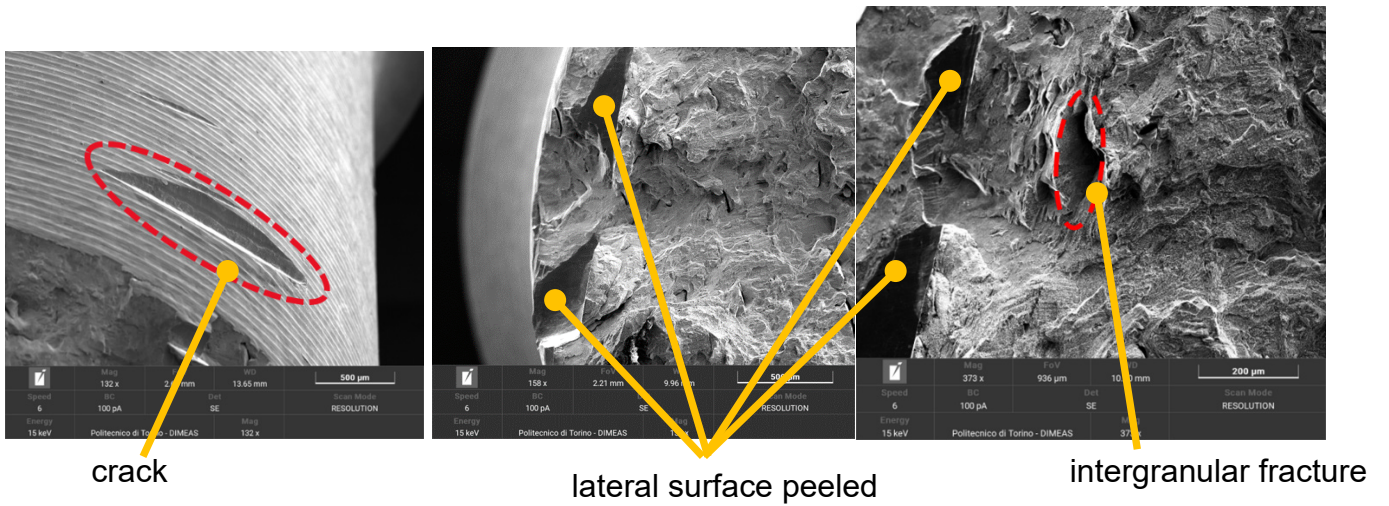


Figure 9-5: cracks, lateral surface peeled/split, intergranular fracture along the boundary

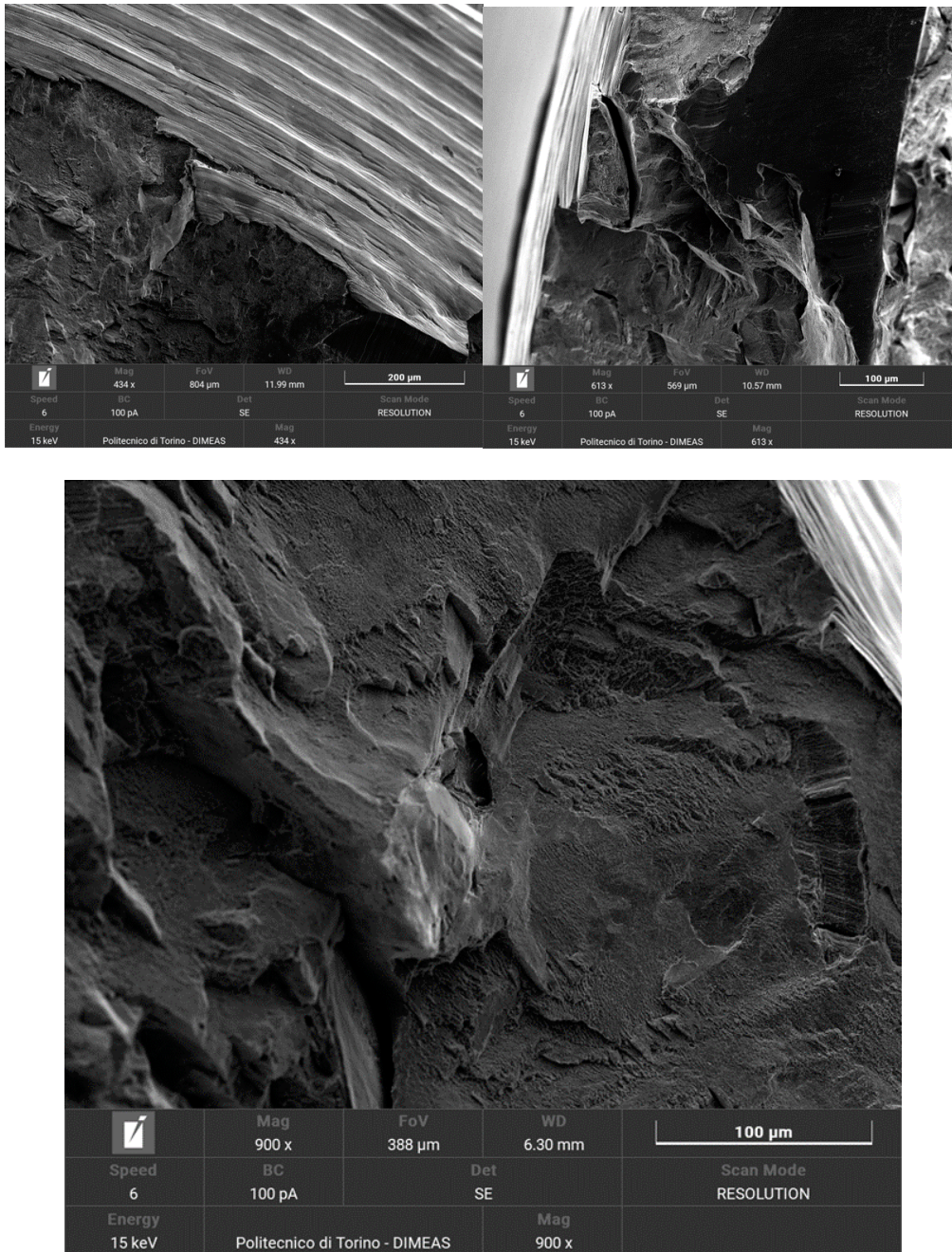


Figure 9-6: Ductile fracture, brittle fracture, intergranular fracture, transgranular fracture, quasi cleavage

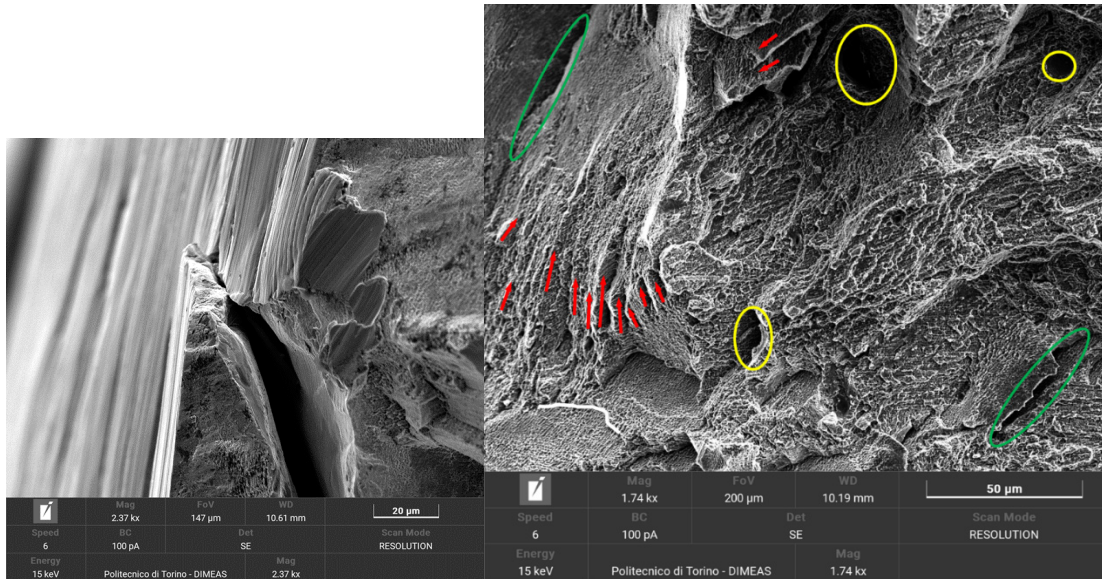


Figure 9-7: intergranular fracture near the lateral surface, Cleavage rivers and stairs, micro voids coalescence, dimples, ductile and brittle fracture

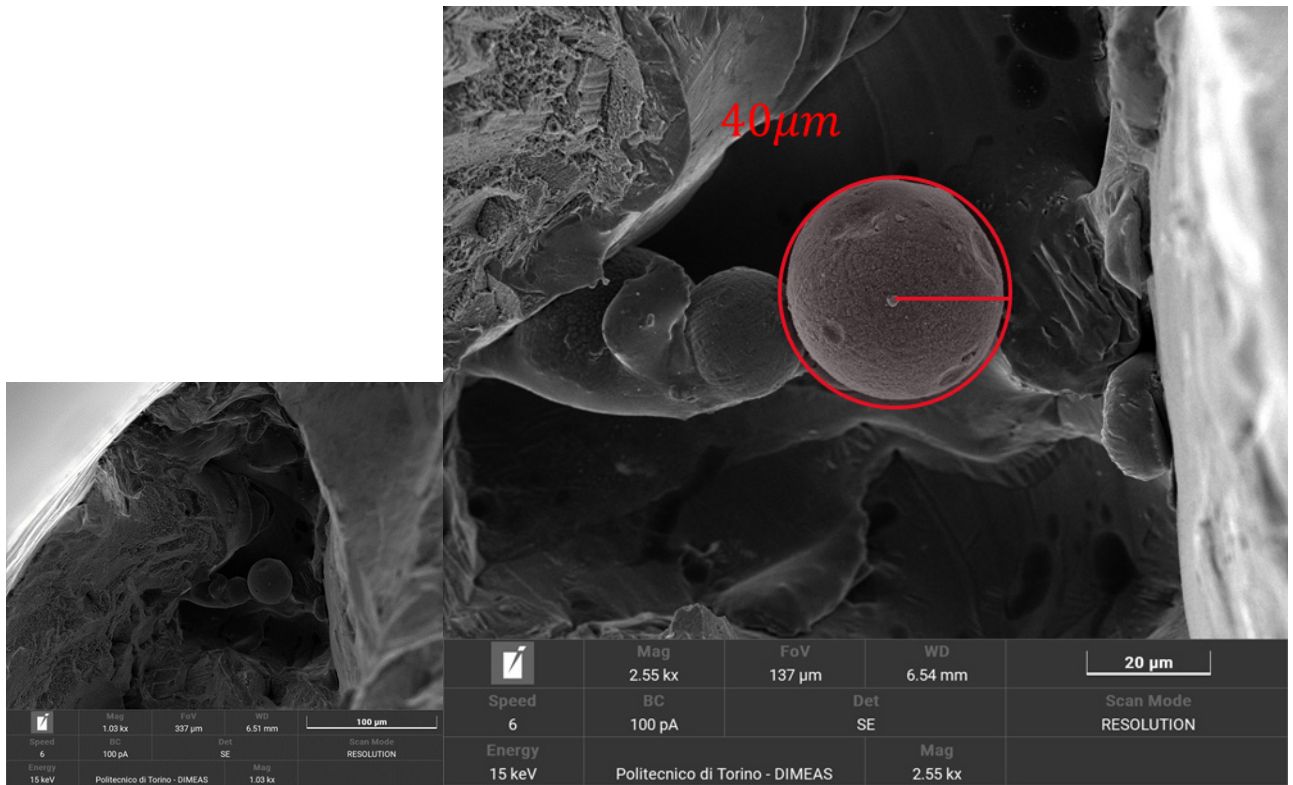


Figure 9-8: Lack of fusion, unmelted particles

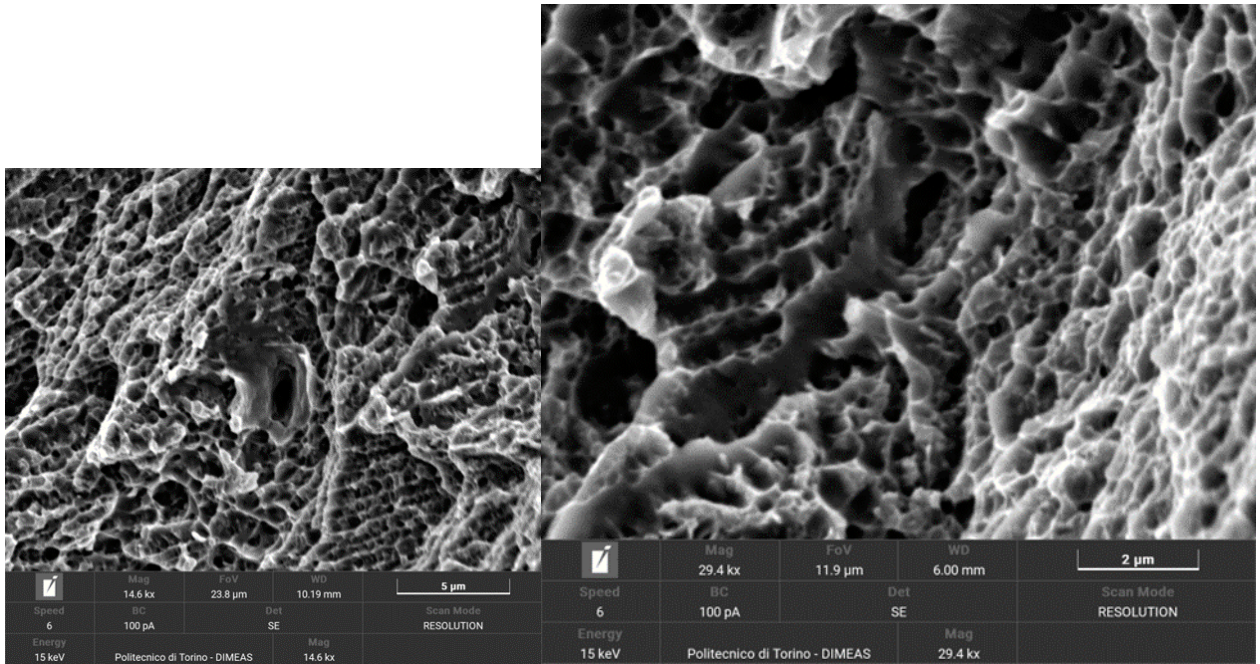


Figure 9-9: Ductile fracture, Micro voids coalescence

9.5 Appendix E: SEM: EDS/EDX for Spectrum results:

Sample A2.1: AS spectrums

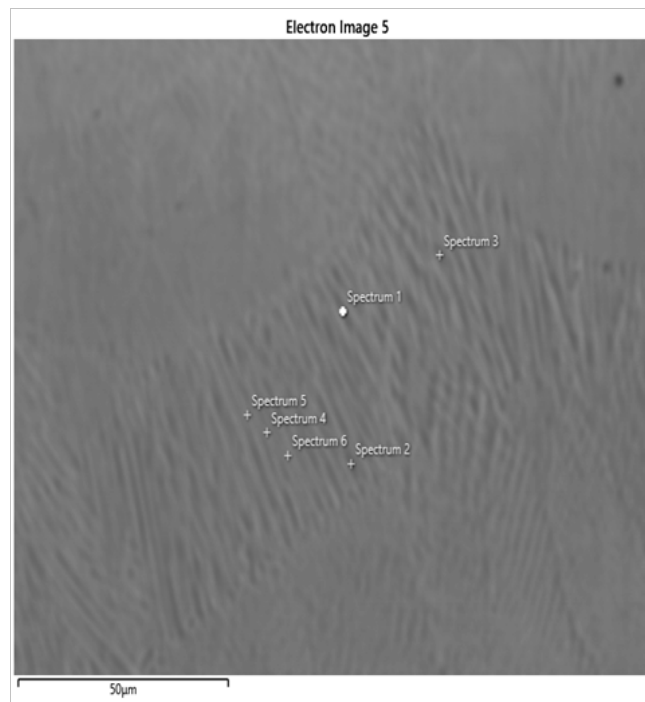


Figure 9-10: SEM micrograph spectrums points

Figure 9-1, describe the spectrum 1 to 6. Below is shown the composition of each spectrum point from **page 111-113**.

